NOVEL PLATINUM-BASED NANOCRYSTALS AND THEIR USE AS ELECTROCATALYSTS FOR THE OXYGEN REDUCTION REACTION

A Dissertation
Presented to
The Academic Faculty

by

Jinho Park

In Partial Fulfillment
of the Requirements for the Degree
of Doctor of Philosophy in the
School of Chemistry and Biochemistry

Georgia Institute of Technology
August, 2016

NOVEL PLATINUM-BASED NANOCRYSTALS AND THEIR USE AS ELECTROCATALYSTS FOR THE OXYGEN REDUCTION REACTION

Approved by:

Dr. Younan Xia, Advisor
Department of Biomedical Engineering
Georgia Institute of Technology

Dr. Angus P. Wilkinson
School of Chemistry and Biochemistry
Georgia Institute of Technology

Dr. Z. John Zhang
School of Chemistry and Biochemistry
Georgia Institute of Technology

Dr. Ronghu Wu
School of Chemistry and Biochemistry
Georgia Institute of Technology

Dr. Seung Woo Lee
School of Mechanical Engineering
Georgia Institute of Technology

Date Approved: June 3, 2016

Dedicated to my parents and wife for their love, endless support, and encouragement.

ACKNOWLEDGEMENTS

In order to reach the finish line of my PhD study, I owe thanks to many people. First and foremost, I would like express my deepest gratitude to my advisor, Professor Younan Xia who trained me with his extreme patience and careful guidance. He provided insightful discussion and stimulated my critical thinking, as well as greatly improved my scientific writing skills. I would also like to thank Professors Seung Woo Lee, Angus Wilkinson, John Zhang, and Ronghu Wu, for serving on my dissertation committee. In particular, I would extend my gratitude to Professor Lee for his valuable discussion regarding electrochemical characterizations.

My special thanks go to Dr. Hsin-Chieh Peng, who generously shared his academic and research experiences over the past four years. I also gratefully give thanks to Professor Sang-Il Choi for sharing many hands-on experiences for syntheses and electrochemical measurements. I sincerely appreciate the collaboration of Professors Manos Mavrikakis, Moon Kim, and Jingyue Liu, who performed DFT calculations and HRTEM for some of my projects. I am grateful to the support provided by many people at Georgia Tech: Professor Dong Qin, Ms. Madeline Vara, Dr. Yi Wang, Ms. Helan Wang, Mr. Shixion Bao, Ms. Sujin Lee, Mr. Ming Lou, Dr. Xue Wang, Mr. Michael Tanes, Mr. Zachary Hood, and many other current and former members of the Xia group, who have helped me tremendously during my dissertation study.

Although this dissertation is dedicated to them, they deserve to be recognized again. I sincerely express my deepest gratitude to my parents, Heonkyu Park and Youngok Ihn for their endless love, support, and prayer for me. And last, I must not miss my deepest and special thanks to my loving wife, Jiyang Oh and my precious daughter, Ella S. Park for keeping me sane with their unwavering love and support.

TABLE OF CONTENTS

LIST OF TABLES

Page

LIST OF FIGURES

LIST OF SYMBOLS AND ABBREVIATIONS

A	the relative specific activity of the ORR catalyst
AA	ascorbic acid
AFC	alkaline fuel cell
BE	benzyl ether
CA	citric acid
CI-NEB	climbing image nudged elastic band
CV	cyclic voltammogram
DEG	diethylene glycol
DFT	density functional theory
DOE	Department of Energy
$\|e\|$	the absolute value of charge of an electron
E(d-band center)	the average energy of d-band
$E_{\text{clean slab}}$	total energy of the slab without the adsorbate
E_{total}	total energy of the adsorbate on the slab
$E_{\text{gas phase}}$	total energy of the isolated adsorbate in the gas phase

E^0	reduction potential
E_A	activation energy
E_O	binding energy of Pt−O bond
E_{OH}	binding energy of Pt−OH
ECSA	electrochemical surface area
EDX	energy dispersive X-ray
EG	ethylene glycol
G	the free energy of the reaction
G_0	the free energy of the overall oxygen reduction reaction
G_1	the free energy of the Step 1 reaction of oxygen reduction
G_4	the free energy of the Step 4 reaction of oxygen reduction
j	the observed current density
j_d	the diffusion-limiting current density
j_k	the kinetic current density
$j_{k,mass}$	the kinetic current density per mass of Pt, mass acitivity
$j_{k,specific}$	the kinetic current density per electrochemical surface area, specific activity

k	rate constant
k_B	Boltzmann constant
HAADF	high-angle annular dark-field
HAc	acetic acid
HOR	hydrogen oxidation reaction
HRTEM	high-resolution transmission electron microscopy
ICP-MS	inductively-coupled plasma mass spectroscopy
MCFC	molten carbonate fuel cell
MEA	membrane-electrode assembly
ML	monolayer
$Ni(acac)_2$	nickel(II) acetylacetonate
OAc	oleic acid
OAm	oleylamine
ORR	oxygen reduction reaction
PAFC	phosphoric acid fuel cell
PEMFC	polymer electrolyte membrane fuel cell
$Pt(acac)_2$	platinum(II) acetylacetonate

PVP	poly(vinyl pyrrolidone)
RDE	rotating disk electrode
RHE	reversible hydrogen electrode
S	entropy
SOFC	solid oxide fuel cell
STEM	scanning transmission electron microscopy
T	absolute temperature
TEM	transmission electron microscopy
U	the electrode operating potential
UPD	underpotential deposition
UPS	ultraviolet photoelectron spectroscopy
V_{RHE}	electric potentials *vs* reversible hydrogen electrode
XPS	X-ray photoelectron spectroscopy
ZPE	zero-point energy

SUMMARY

Owing to the low operating temperature and high power density, polymer electrolyte membrane fuel cells (PEMFCs) are promising candidates to replace the conventional combustion engines in the automotive industry. The poor performance of Pt-based catalysts toward oxygen reduction still needs to be addressed to make PEMFCs viable for commercialization. To this end, it is essential to tailor the physicochemical properties of the catalytic nanocrystals involved, including the crystal facets, elemental composition, and structure. This dissertation includes a number of projects for the development of Pt-based electrocatalysts with markedly enhanced performance toward oxygen reduction. In the first project, I synthesize Pd@Pt_{nL} core−shell octahedra by depositing ultrathin Pt shells on octahedral nanocrystals made of a less expensive metal, such as Pd. This strategy presents a great opportunity to enhance both the activity and durability of the catalyst toward oxygen reduction while significantly reducing the Pt loading in a PEMFC. Theoretical calculations are also employed to understand the improvement in catalytic activity. In the second project, I further apply the Pt deposition method to passivate Pt−Ni alloy octahedral nanocrystals and improve their poor catalytic durability toward oxygen reduction. In this strategy, an ultrathin Pt shell effectively protects the Ni in the Pt−Ni alloy core from dissolution in a highly corrosive environment, greatly improving the catalytic durability. In the third project, I developed an advanced catalyst based upon Pt nanoframes with open faces and a hollow interior. The catalyst exhibits not only significantly increased catalytic surface area but also remarkably improved durability toward oxygen reduction. The strategies presented in this dissertation and the understanding of catalytically relevant physicochemical properties offer insights for the design of advanced fuel cell catalysts in the future, allowing for large-scale commercialization of PEMFCs.

CHAPTER 1

INTRODUCTION

1.1 The Fuel Cell Technology and Oxygen Reduction Reaction

A fuel cell is a device designed to convert chemical energy directly into electrical energy. Owing to its high efficiency and low emission of pollutants, the fuel cell technology has been considered as a promising platform of energy for the future [1]. In general, a fuel cell is composed of three components: anode, electrolyte, and cathode. Both the anode and cathode contain catalysts to accelerate the corresponding reactions, respectively. At the anode, oxidation of a fuel (usually hydrogen, H_2) occurs, producing positively charged ions and electrons. The electrolyte is specifically designed to allow those ionic species to pass between the two electrodes. The electrons are transferred from the anode to the cathode through an external circuit. At the cathode, another compound (usually oxygen, O_2) is electrocatalytically reduced to produce negatively charged ions and/or water. The different types of fuel cells are summarized in Figure 1.1. In an SOFC or MCFC, both CO and H_2 are supplied to the anode as fuels. On the other hand, an AFC, PEMFC, or PAFC essentially employs relatively pure hydrogen as a fuel to be fed to the anode [1].

Among these fuel cells, PEMFC is particularly promising for the automotive industry due to its lower operating temperature and higher power densities relative to other types of fuel cells [1−3]. As shown in Figure 1.2, H_2 is supplied to the cell and then oxidized at the anode, producing protons (H^+) and electrons (e^-). The protons and electrons are transferred to the cathode through an electrolyte (a polymer membrane) and an external circuit, respectively. At the cathode, the electrocatalytic ORR takes place with the transferred protons and electrons, producing water. In a PEMFC, the ORR at the cathode is six or more orders of magnitude slower than the HOR at the anode, limiting the overall

performance of a fuel cell [3]. Thus, most of the research has focused on how to enhance the performance of a PEMFC by developing an advanced cathode catalyst for ORR. Currently, the most effective catalysts for ORR are based on Pt nanoparticles of 2−3 nm in size [4−6]. However, the price of Pt has rapidly increased over the past few decades owing to its extremely low abundance in the Earth's crust and the ever-growing demand for this precious metal in the automotive industry [4 ,7, 8].

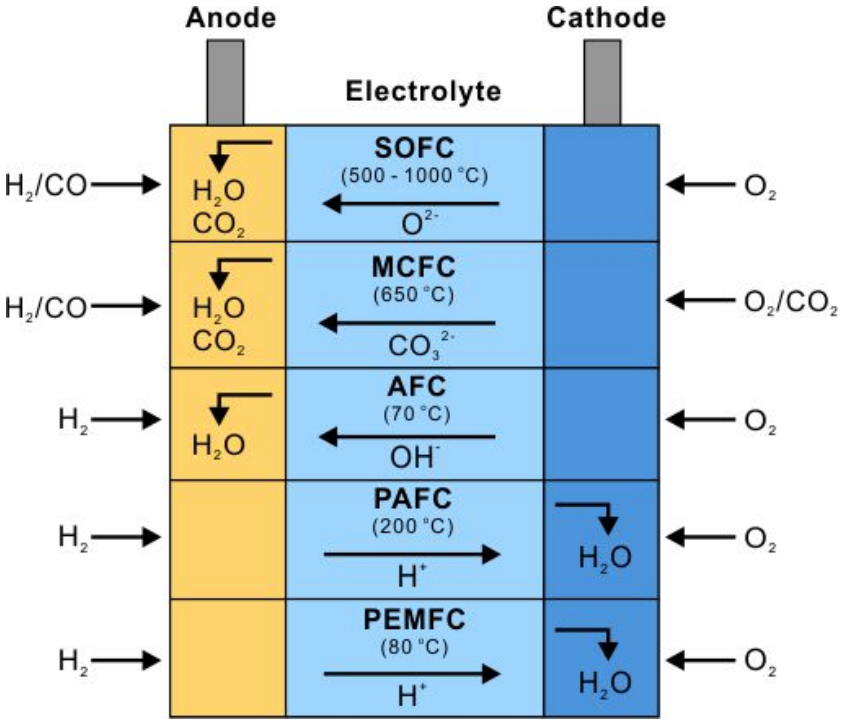

Figure 1.1. Summary of fuel cell types. In addition to electrical energy, H_2O and/or CO_2 are produced at the anode of an SOFC, MCFC, or AFC, and at the cathode of a PAFC or PEMFC types. The operating temperature and relevant catalysts also vary on the type of a fuel cell. (Adapted with permission from [1]. Copyright 2001 Nature Publishing Groups.)

Even though the commercial Pt/C catalyst gives an extremely high specific ECSA, unfortunately, the mass activity (per unit mass of Pt, A mg_{Pt}^{-1}) of this catalyst is limited by its low specific activity (per unit surface area, mA cm_{Pt}^{-2}) [7]. As recommended by

the United States DOE, the loading of Pt in an ORR catalyst needs to be reduced by at least four-fold relative to the current state-of-the-art commercial Pt/C catalyst in order to make PEMFCs a viable technology for large-scale use [8]. To reduce the Pt loading in a PEMFC, it is therefore necessary to design new ORR catalysts with drastically improved mass activity.

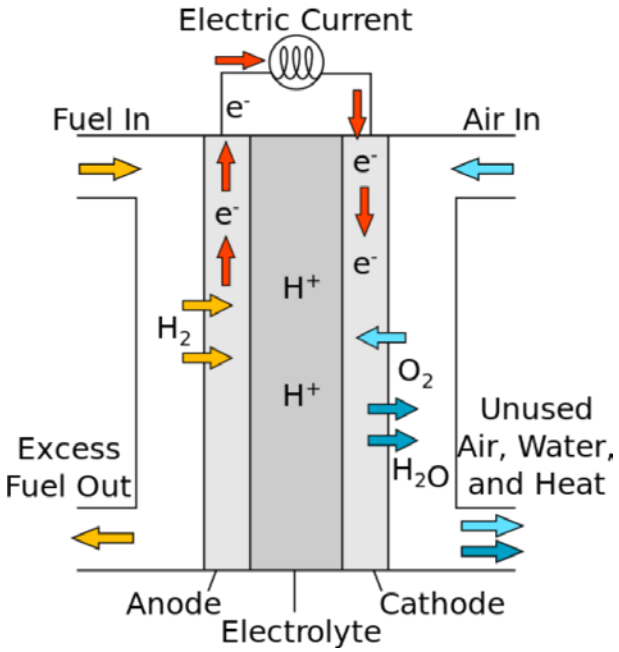

Figure 1.2. Schematic diagram of a PEMFC. H_2 is fed into the cell and oxidized at an anode, producing protons (H^+) and electrons (e^-). The protons and electrons are transferred to the cathode through a polymer membrane (electrolyte) and an external circuit, respectively. An ORR occurs at a cathode with the protons and electrons transferred from the anode, producing water. (Adapted with permission from [8]. Copyright 2012 United States Department of Energy.)

As shown in Figure 1.3, two different approaches can be utilized to enhance the mass activity of an ORR catalyst: *i*) increasing its specific ECSA and *ii*) enhancing its specific activity. These two approaches should be combined to maximize the mass activity of an ORR catalyst. In general, increasing the specific ECSA of an ORR catalyst can be achieved by simply decreasing the size of the nanoparticles involved [9]. However, it is well documented that the specific activity of an ORR catalyst is usually reduced when decreasing the size of the nanoparticles involved. [10, 11] Therefore, to maximize the mass activity, it is essential to explore new strategies for enhancing the specific activity while maintaining the high specific ECSA of the catalyst.

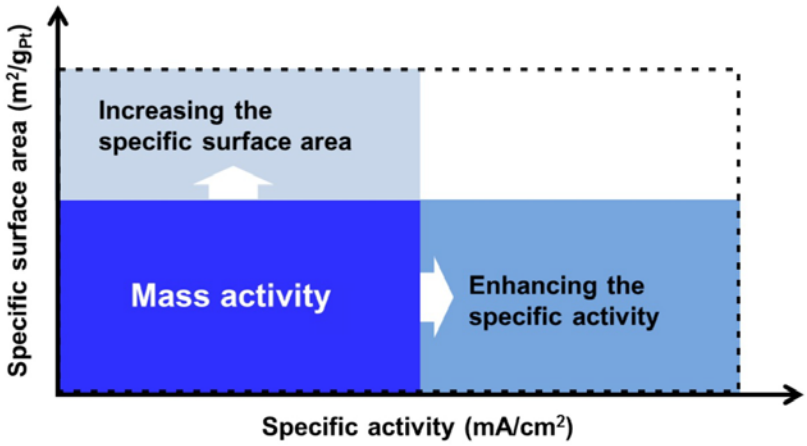

Figure 1.3. Two approaches to the enhancement of mass activity (per unit mass of Pt) of an ORR catalyst. The mass activity can be enhanced by increasing the specific ECSA and/or specific activity (per unit area of Pt). When combined together, the mass activity can be maximized as marked area enclosed by the dashed lines.

In order to design an ORR catalyst with enhanced specific activity, it is necessary to understand the mechanisms of electrocatalytic oxygen reduction. The overall equation of ORR can be written as [12]:

$$O_2 + 4H^+ + 4e^- \rightarrow 2H_2O \qquad (1.1)$$

This overall reaction is composed of four major steps (Equation 1.2−1.5) [12]:

$$\text{Step 1:} \quad O_2 + 4H^+ + 4e^- \rightarrow OOH^* + 3H^+ + 3e^- \tag{1.2}$$

$$\text{Step 2:} \quad OOH^* + 3H^+ + 3e^- \rightarrow O^* + H_2O + 2H^+ + 2e^- \tag{1.3}$$

$$\text{Step 3:} \quad O^* + H_2O + 2H^+ + 2e^- \rightarrow OH^* + H_2O + H^+ + e^- \tag{1.4}$$

$$\text{Step 4:} \quad OH^* + H_2O + H^+ + e^- \rightarrow 2H_2O \tag{1.5}$$

where * represents the active site of catalyst. Figure 1.4 shows the free energy diagram regarding the various steps of ORR on Pt(111). The diagram indicates that ORR is thermodynamically spontaneous. However, among all steps, Step 1 (hydrogenation of O_2) and Step 4 (hydrogenation of OH*) are nonspontaneous and they are the rate-limiting steps of ORR [12]. It is worth pointing out that the Step 1 and Step 4 are involved with the adsorption of an oxygen molecule onto the Pt and the desorption of OH from the Pt, respectively. Thus, as the Pt−O binding energy increases, Step 1 can be accelerated with its decreased free energy of reaction (ΔG_1). In contrast, with the increased Pt−OH binding energy, Step 4 is decelerated due to the increased free energy of reaction (ΔG_4). Combined together, the overall free energy of ORR (ΔG_0) as a function of Pt−O binding energy shows as a volcano profile (Figure 1.5) [12]. Note that even though the Pt−OH binding energy (ΔE_{OH}) is not the same as the value of Pt−O binding energy (ΔE_O), they have a linear correlation. [10] The volcano plot in Figure 1.5 indicates that the overall kinetics of ORR are determined by Step 1 when oxygen is too weakly bound to Pt (right-half region of the volcano). Conversely, Step 4 becomes the rate-limiting step of ORR if the oxygen is too strongly bound to Pt. In addition, this plot also provides critical information on how to design a Pt-based ORR catalyst to enhance the specific activity by engineering the catalyst to have either stronger or weaker binding energy with oxygen. For example, the ORR kinetics on the pure Pt(111) are limited by Step 4, and can be enhanced by modifying the catalyst to weaken Pt−O binding.

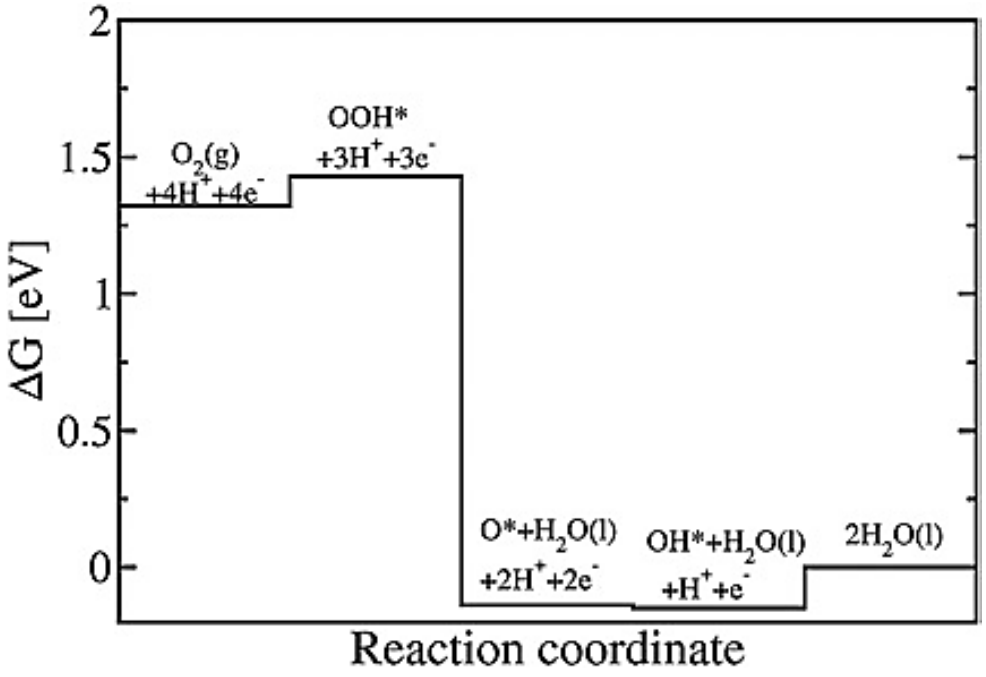

Figure 1.4. The free energy diagram for the four step reactions of ORR at 0.9 V_{RHE} on Pt (111). Even though the overall ORR is a spontaneous reaction, there are two nonspontaneous step reactions involved: the hydrogenation of O_2 (Step 1) and the hydrogenation of OH* (Step 4). It implies that such step reactions could be considered as candidates of the rate-limiting step for the ORR. (Adapted with permission from [12]. Copyright 2008 Royal Society of Chemistry.)

The catalytic activity is not the only important consideration in developing advanced ORR catalysts. The durability of ORR catalyst is another crucial property to address for large scale commercialization of PEMFCs [13]. It is particularly difficult to achieve good durability for an ORR catalyst owing to the highly corrosive environment during the operation of a PEMFC, including the high content of oxygen and highly positive electric potentials [13−15]. Furthermore, especially in automotive applications, the PEMFC is operated in a wide range of conditions such as start−stop cycles, low humidity, and fuel starvation, all of which affect the catalytic durability. [13]

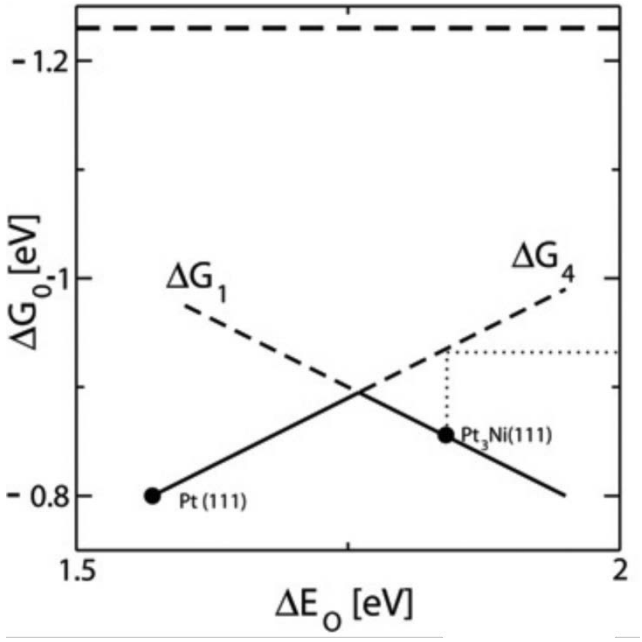

Figure 1.5. The overall free energy of ORR (ΔG_0) as a function of Pt−O binding energy (ΔE_O). Either Step 1 or Step 4 is the rate-limiting step of the ORR. (Adapted with permission from [12]. Copyright 2008 Royal Society of Chemistry.)

In addition to the low activity, the commercial Pt/C catalyst is plagued by poor durability. During the long-term operation of the cell, the ECSA of a Pt/C catalyst rapidly decreases through several routes: *i*) dissolution of Pt atoms from the Pt nanoparticles; *ii*) detachment of Pt nanoparticles from the carbon support; and *iii*) growth of the Pt nanoparticles [13, 14]. Based on the thermodynamics, bulk Pt can be oxidized and dissolved with positive potential over 1.2 V_{RHE}:

$$Pt \leftrightarrow Pt^{2+} + 2e^{-} \qquad E^0 = 1.1\ V_{RHE} \qquad (1.6)$$

The equilibrium electrochemical potential (E^0) for Pt dissolution drops in case of Pt nanoparticles and further decreases with the size. Accordingly, higher Pt^{2+} concentrations

were measured for Pt/C at 80 °C than predicted for bulk Pt [13, 14]. Moreover, the dissolution of Pt from the Pt nanoparticles can be accelerated under conditions involving high oxygen content through the formation of PtO on the surface. The detachment of Pt nanoparticles during ORR can be attributed to the oxidation of carbon (carbon corrosion) [13]. Thermodynamically, carbon can be oxidized to CO_2 under the loading of low electric potential:

$$C + 2H_2O \leftrightarrow CO_2 + 4H^+ + 4e^- \qquad E^0 = 0.21\ V_{RHE} \qquad (1.7)$$

Despite its slow kinetics, the oxidation of carbon can result in the detachment of Pt nanoparticles from the catalyst due to extremely small contact area between the carbon and Pt nanoparticles. The growth of Pt nanoparticles can proceed *via* two different mechanisms, Ostwald ripening through migration of atoms and aggregation through migration of the particles. The growth can be accelerated with the highly positive potential loaded on the cathode of a PEMFC [13].

1.2 Enhancing the Performance of Pt-based Catalysts toward Oxygen Reduction

In an attempt to address the issues related to the low activity and poor durability of the commercial Pt/C, many strategies have been intensively explored over the past two decades. In general, the performance of an ORR catalyst can be improved by controlling characteristics of the nanoparticles involved, for example, shape (or facet), elemental composition, and structure. In this section, I introduce a series of novel studies accomplished for enhancing the activity and/or durability of Pt-based ORR catalysts.

1.2.1 Control of Shape or Facet

It has been established that the catalytic activity of a single crystal is sensitive to the exposed facet for a certain reaction. In particular, the kinetics of electrocatalysis for oxygen reduction has a strong correlation with the facets on Pt-based nanocrystals. The facet-sensitivity of ORR toward the low-index facets of pure Pt has been established by Markovic, Gasteiger, and Ross [16−19]. The specific activities of single-crystal Pt(*hkl*) surfaces are found to increase in the order of Pt(100) << Pt(111) ≈ Pt(110) when in a non-adsorbing electrolyte such as perchloric acid (Figure 1.6) [16, 20]. The different ORR activities are attributed to the facet-sensitive adsorption of the oxygen species (O and OH) on Pt(*hkl*) single-crystal surfaces, which arises from different geometries of the surface atoms. When a transition metal (M = Ni, Co, and Fe) is introduced to form Pt−M alloy, the facet-sensitivity of the ORR activity will be altered. For example, the specific activity of low-index Pt_3Ni(*hkl*) alloy surfaces follows the order of $Pt_3Ni(100)$ < $Pt_3Ni(110)$ << $Pt_3Ni(111)$ as shown in Figure 1.6 [20]. Despite the altered order, the facet-sensitivity of the ORR activity on the Pt_3Ni(*hkl*) alloy surfaces also originates from the geometric difference in surface structure.

Based upon the facet-sensitivity of the Pt-based single crystals toward the ORR, many researchers have developed new catalysts using nanocrystals that are enclosed by the favored facets [21−28]. With regard to pure Pt, rhombic dodecahedra (enclosed by {110}) and octahedra (enclosed by {111}) are anticipated to be more active toward ORR than cubes (enclosed by {100}). In 2013, Hong and co-workers successfully synthesized Pt icosahedra, which are also enclosed by Pt{111} facets, and evaluated their ORR activity by benchmarking against Pt nanocubes and a commercial Pt/C [25]. As shown in Figure 1.7, the Pt icosahedra exhibited 2.3 and 4 times enhancement in the specific ORR activity relative to the Pt cubes and a commercial Pt/C.

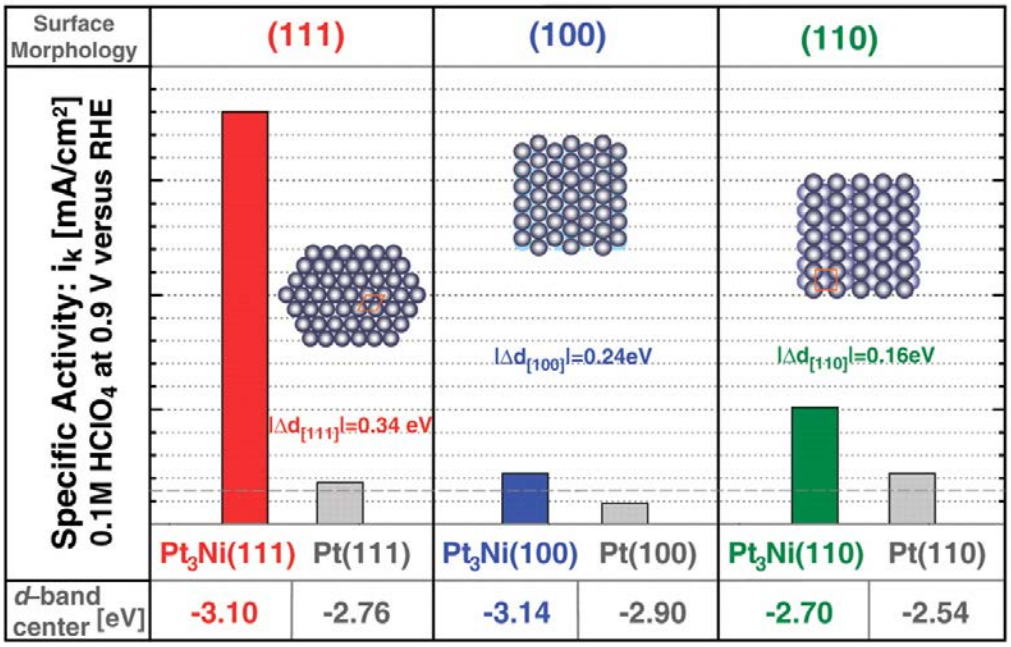

Figure 1.6. Influence of the surface morphology and electronic surface properties on the kinetics of ORR. Both the d-band centers and specific ORR activities were measured for the pure Pt(*hkl*) and Pt_3Ni(*hkl*) single-crystal surfaces. Specific activity is given as a kinetic current density, i_k, measured at 0.9 V_{RHE}. The energies of d-band center were obtained from UPS spectra. (Adapted with permission from [20]. Copyright 2007 American Association for the Advancement of Science.)

Owing to the much improved activity of the Pt−M alloy for ORR relative to the pure Pt, shape control of Pt−M nanocrystals has been actively studied in recent years [21, 24, 27]. To this end, the Fang group demonstrated the syntheses of Pt_3Ni nanocubes and octahedra to compare their activities toward ORR [21]. In terms of specific activity, the Pt_3Ni octahedra showed significant enhancement (by more than 5 times) as compared to the Pt_3Ni nanocubes (Figure 1.8). The mass activity also increased with the octahedral nanocrystals rather than the cubic ones.

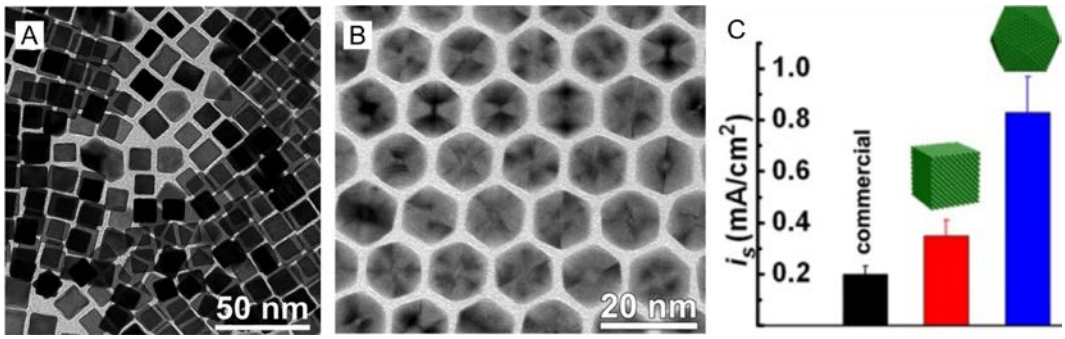

Figure 1.7. TEM images of (A) Pt cubes and (B) Pt icosahedra. (C) Specific activities (0.9 V_{RHE}) for the commercial Pt/C catalyst (the black bar), Pt cubes catalyst (the red bar), and Pt icosahedra (the blue bar) toward the ORR. (Adapted with permission from [25]. Copyright 2013 American Chemical Society.)

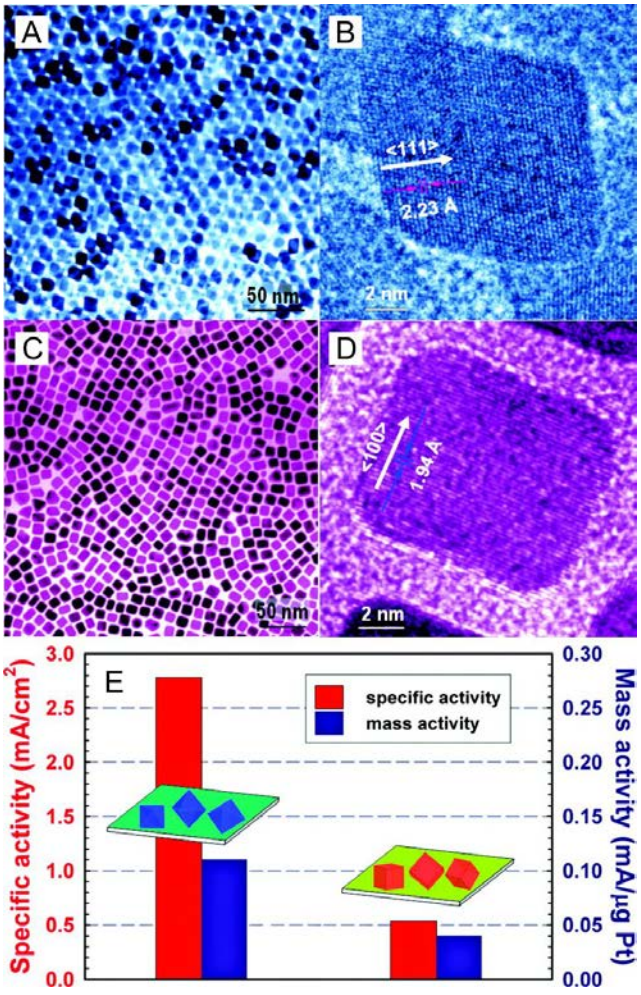

Figure 1.8. TEM and HRTEM images of (A and B) Pt_3Ni octahedra and (C and D) Pt_3Ni cubes. (E) Specific and mass activities (0.9 V_{RHE}) for the Pt_3Ni octahedra (left) and Pt_3Ni cubes (right) toward ORR. (Adapted with permission from [21]. Copyright 2010 American Chemical Society.)

1.2.2 Control of Elemental Composition

As oxygen binds too strongly to the the pure Pt surface, the overall kinetics of ORR on a Pt surface becomes limited by the hydrogenation of OH* (Step 4, Equation 1.5). In this regard, the Pt surface of Pt needs to be engineered to decrease the binding energy with the oxygen species. To this end, alloying Pt with another transition metal could modify the electronic structure of surface Pt atoms and thus decrease the binding energies with O (and/or OH) [29]. It is well-established that surface binding energies with the adsorbates correlate with the average energy of the d states (d-band center) of the surface atoms.[30–32] As shown in Figure 1.9A, the d-band center energy (*E*(d-band center)) of the Pt(111) or $Pt_3M(111)$ alloy surface has a linear correlation with Pt−O binding energy (ΔE_O). Lowering the d-band center of Pt also results in a down shift for the anti-bonding energy state of the Pt−O bond, and thus more electrons can exist in the anti-bonding state, destabilizing the Pt−O bond. By alloying with most transition metals, the d-band center of Pt tends to decrease, leading to a lower Pt−O binding energy. Figure 1.9B shows the relative ORR specific activities (0.9 V_{RHE}) of pure Pt(111) and $Pt_3M(111)$ surfaces as a function of d-band center energy [29]. The plots from both the experiments (red) and calculations (black) exhibit a classical volcano-shape, like the one in Figure 1.5. In all cases, the ORR activity is enhanced by alloying Pt with the transition metal due to the decreased Pt−O binding energy. However, in cases where the binding with oxygen becomes too weak (Pt_3Fe and Pt_3Ti), the overall kinetics becomes limited by the adsorption of oxygen (Step 1), resulting in a decrease in ORR activity. Based on the plots, the Pt_3Ni and Pt_3Co are expected to exhibit the highest activity toward ORR among the Pt_3M alloys, since their Pt−O binding energy is around the optimal value for the oxygen reduction.

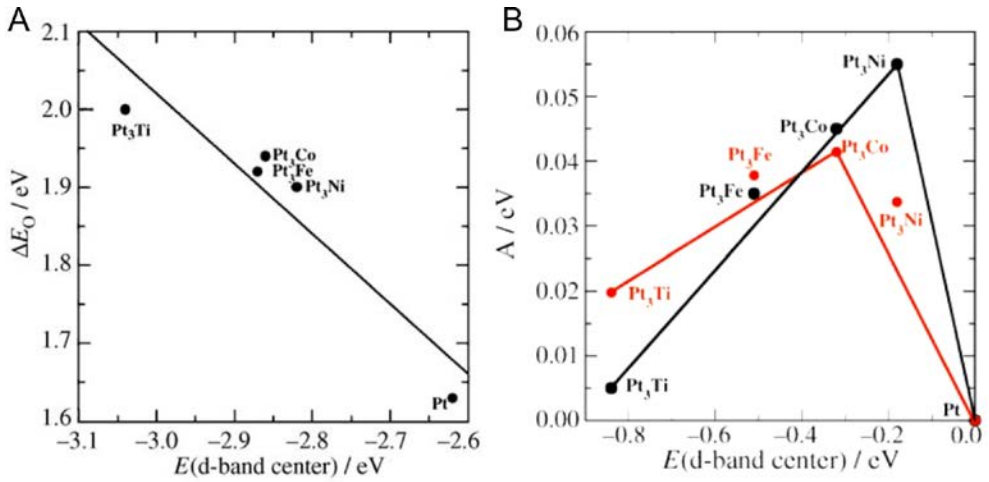

Figure 1.9. (A) Pt−O binding energies (ΔE_O) of the Pt(111) and Pt_3M(111) alloy surfaces as a function of d-band center energy (E(d-band center)). (B) Relative ORR specific activities (at 0.9 V_{RHE}) of pure Pt(111) and Pt_3M(111) surfaces as a function of d-band center energy. The activity predicted from DFT simulations is shown in black, and the measured activity is shown in red. (Adapted with permission from [29]. Copyright 2006 Wiley-VCH.)

In an extended study, Stamenkovic and Markovic group have experimentally compared the specific ORR activities of pure Pt and Pt_3Ni alloy single-crystal surfaces with three different low-index facets: (111), (100), and (110) [19]. For all those facets, the Pt_3Ni alloy surfaces showed a lower d-band center energy and thus a great enhancement in specific activity relative to the pure Pt surfaces. In particular, the (111) single-crystal surface exhibited the most significant enhancement of over 10-fold through the introduction of Ni. It is also 90-fold more active than a state-of-the-art Pt/C toward ORR in terms of specific activity at 0.9 V_{RHE} (Figure 1.6).

Due to the remarkably improved specific activity with the Pt_3Ni(111) surfaces, Pt−Ni alloy nanocrystals enclosed by {111} facets have been intensively explored as an advanced ORR catalyst [21, 33−43]. To this end, in 2012 our group reported a remarkably high mass activity of 3.3 A mg_{Pt}^{-1} for Pt−Ni alloy octahedra (Pt/Ni (mol) =

2.5), which is 17-fold higher than that of a commercial Pt/C [38]. It was further confirmed the elemental composition of Pt−Ni octahedra would affect the ORR activity by varying the Pt/Ni ratios from 1.4 to 3.7 [39]. In 2015, Huang and co-workers reported the record-setting mass activity toward ORR with molybdenum (Mo)-doped Pt_3Ni octahedra [43]. By doping the surfaces with Mo atoms, they could slightly increase Pt−O binding energy of the $Pt_3Ni(111)$ surface, resulting in further enhancement in specific activity relative to pristine $Pt_3Ni(111)$.

1.2.3 Control of Structure

In addition to the shape and elemental composition, the structure of nanoparticles can be controlled to improve the performance of Pt-based ORR catalysts. In general, the Pt-based ORR catalysts are composed of nanoparticles enclosed by low-index facets with a uniform elemental composition. However, uncommon structures such as core−shell nanoparticles [44−59], dendrites [60], nanocages [61−63], and nanoframes [64−66] provide more opportunity to enhance the activity and/or durability of the catalyst. Among them, Pt-based core−shell nanocrystals have been most actively explored for several reasons. First, the materials cost can be reduced by replacing Pt in the core with a less expensive metal. The introduction of a different metal can alter the electronic structure of Pt through the ligand and strain effects, resulting in enhancement in ORR activity. In addition to activity, catalytic durability also can be improved by switching to the core−shell nanocrystals with relatively large size. In principle, these advantages become dominant when the thickness of Pt shell decreases down to less than 1 nm. The synthesis of Pt-based core−shell nanocrystals has been demonstrated through both electrochemical [26, 44, 45, 47−49, 51, 58] and chemical methods [46, 50, 52, 53−57, 59]. In 2004, the Adzic group demonstrated electrochemical deposition of a Pt monolayer on various types of cores to develop a new class of ORR catalyst based on the core−shell nanocrystals [44]. To deposit a monolayer of Pt on the nanocystals, they employed the galvanic

replacement reaction between the underpotentially deposited Cu monolayer and a Pt precursor. This method could be extended to generate more complex structures such as core−interlayer−shell nanocrystals.

Shao and co-workers reported the synthesis of the $Pd@Au_{1L}@Pt_{1L}$ core−interlayer−shell nanocrystals by electrochemically depositing monolayer of Au and then Pt on the surfaces of shape-controlled Pd nanocrytals [26]. Through the inclusion of Au interlayer between Pd core and Pt shell, both the catalytic activity and durability could be improved toward ORR (Figure 1.10A). The Au interlayer increased the reduction potential of neighboring atoms on the nanocrystals, suppressing the dissolution of Pt and/or Pd during electrochemical operation at low pH and highly positive potential. Furthermore, the Au interlayer can alter the electronic structure of Pt, lowering the d-band center and thus enhancing the ORR activity of the Pt-based catalyst. Although the electrochemical method is attractive to generate Pt-based core−shell nanocrystals with precisely controlled Pt shell thicknesses, the involvenment of electrode for the deposition process severly limites the scale at which such syntheses can be conducted.

Alternatively, our group has developed a solution-phase protocol for the chemical deposition of conformal Pt shells of 1−6 atomic layers in thickness on facet-controlled Pd nanocrystals [53−55]. The key to the success of this deposition is a combination of slow Pt deposition kinetics and a relatively high reaction temperature, allowing time for newly deposited Pt adatoms to diffuse across the entire surface of a Pd nanocrystal. When benchmarked against a commercial Pt/C catalyst, the $Pd@Pt_{nL}$ (n = 1−6) core−shell nanocrystals showed great enhancement in terms of activity as well as durability toward ORR (Figure 1.10B) [53].

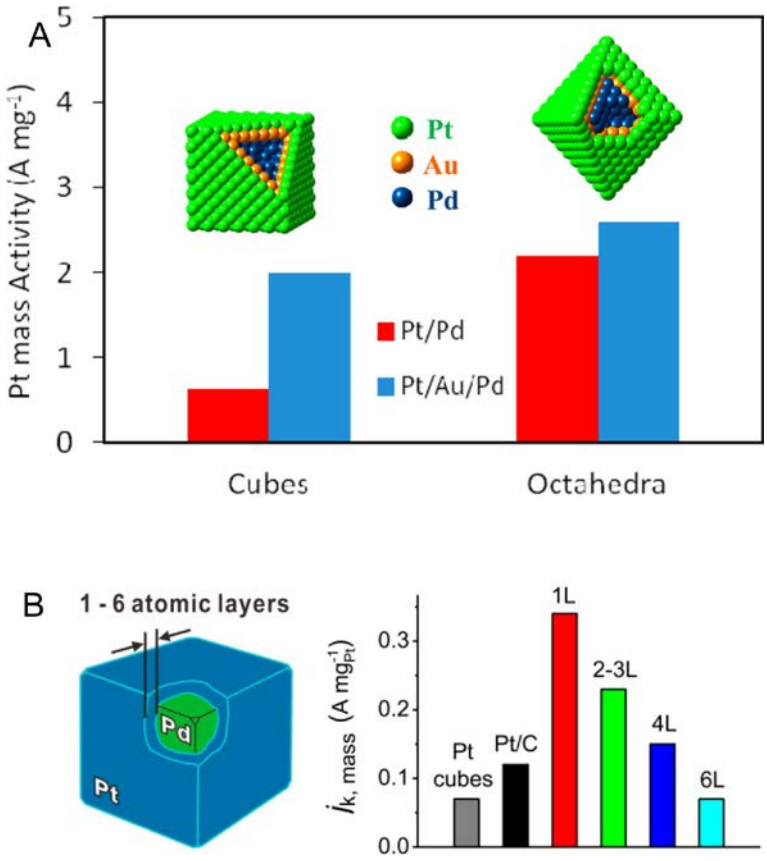

Figure 1.10. (A) Mass activities (0.9 V_{RHE}) of the Pd@Pt core−shell cubes and octahedra (red), and Pd@Au@Pt core−interlayer−shell nanocubes and octahedra (blue). (B) A model of Pd@Pt_{nL} core−shell nanocube and its mass ORR activity (0.9 V_{RHE}) toward ORR with different number of Pt atomic layers. Adapted with permission from [26, 53]. Copyright 2010 American Chemical Society.)

Despite the remarkable improvement in both the activity and durability toward ORR with the Pd@Pt core−shell nanocrystals, the use of Pd cores still largely contributes to the high cost of material. Our group successfully fabricated Pt-based hollow nanocages comprised of well-defined facets by selectively etching away Pd cores from the Pd@Pt_{nL} nanocrystals (Figure 1.11) [61, 62]. Different from the core−shell structure, these hollow nanocages allow both the outer and inner surfaces of a Pt shell to participate in the catalytic reaction, further increasing the mass activity [61−63]. Even after the removal of Pd cores from the Pd@Pt_{nL} nanocrystals, the Pt nanocages largely retained their side

faces which are active for the ORR. Owing to these structural advantages, the icosahedral Pt nanocages have recorded the highest mass activity up to date (1.28 A mg_{Pt}^{-1}) among the catalysts based on pure Pt [62].

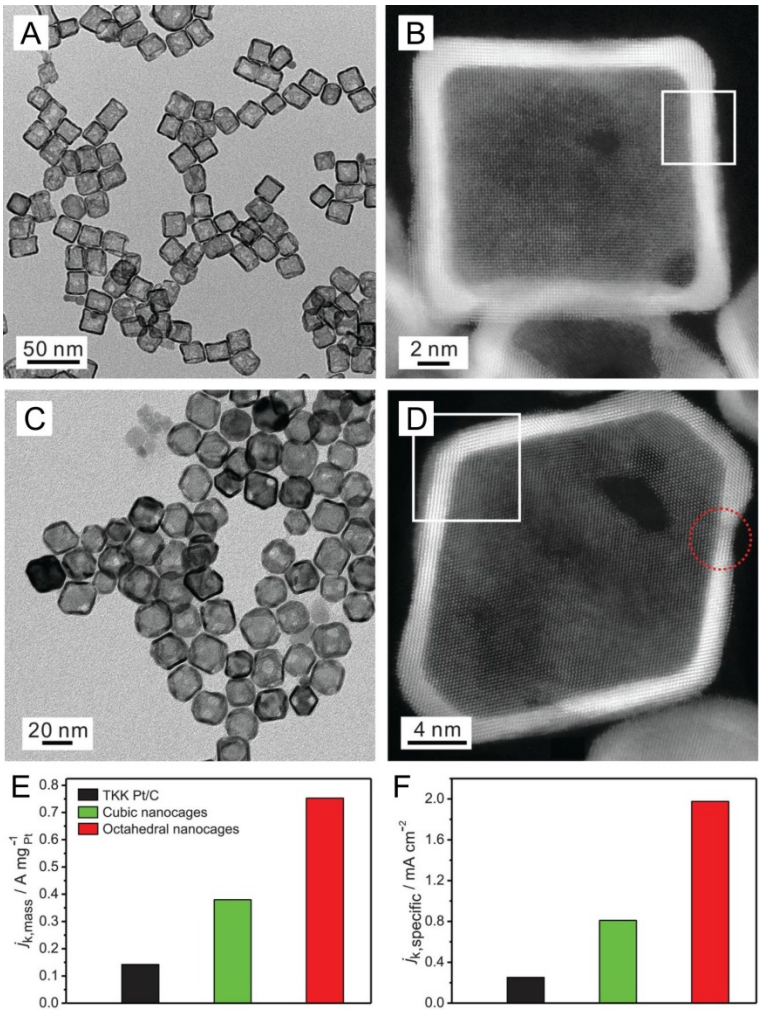

Figure 1.11. TEM and HAADF-STEM images of (A and B) Pt cubic nanocages and (C and D) Pt octahedral nanocages. (E) Mass and (F) specific activities (at 0.9 V_{RHE}) toward ORR measured for the cubic (green) and octahedral (red) nanocages and the commercial Pt/C (black). (Adapted with permission from [61]. Copyright 2015 American Association for the Advancement of Science.)

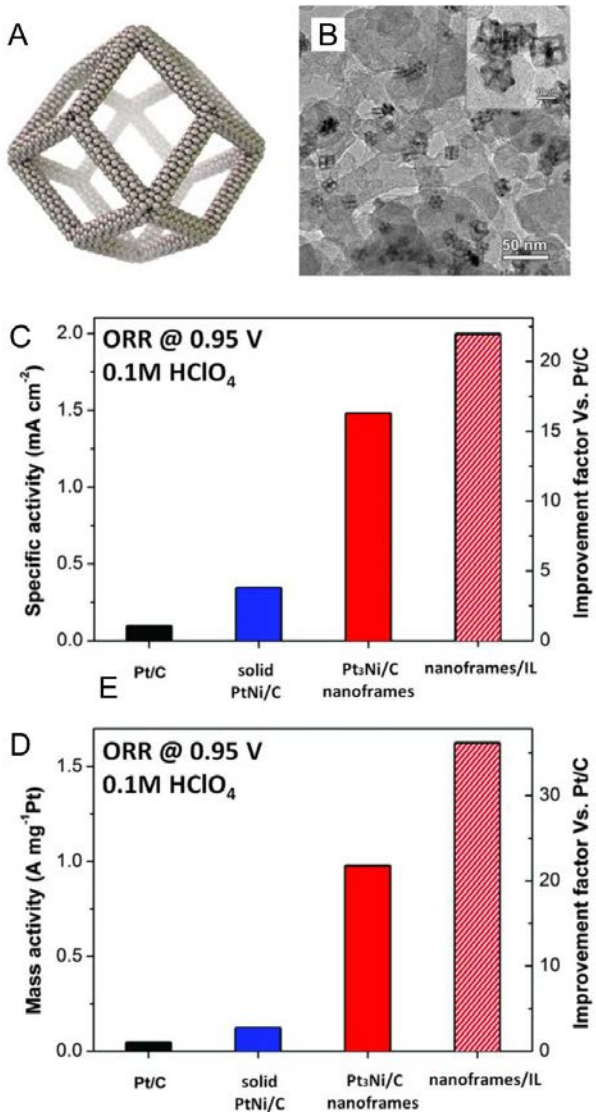

Figure 1.12. (A) Atomic model and (B) TEM image of Pt_3Ni nanoframes. (C) Specific and (D) mass activities (at 0.95 V_{RHE}) of the commercial Pt/C, solid PtNi/C (6-nm PtNi alloy nanoparticles on carbon), and Pt_3Ni/C nanoframes (Pt_3Ni nanoframes on carbon), respectively. ORR activity of the Pt_3Ni/C nanoframes were also measured in an ionic liquid (IL). (Adapted with permission from [64]. Copyright 2014 American Association for the Advancement of Science.)

Another promising structure for the advanced ORR catalyst is nanoframes, composed only of ultrathin ridges (a few nanometers in thickness) with open faces and a hollow interior [64−66]. As a highly open structure, the nanoframes provide not only extremely high specific ECSA, but also allow for accelerated diffusion of the chemicals involved, leading to enhanced ORR kinetics. Yang, Stamenkovic, and co-workers have synthesized

Pt_3Ni alloy nanoframes through the interior erosion of $PtNi_3$ polyhedra [64]. In this protocol, the $PtNi_3$ polyhedron slowly transformed into the Pt_3Ni nanoframe in hexadecane, for 12 h (Figure 1.12). With a catalyst based on the Pt_3Ni nanoframes, they have achieved dintingtively high mass activity of 5.7 A mg_{Pt}^{-1} at 0.9 V_{RHE}.

1.3 Scope of this Work

The aim of this work is to develop Pt-based advanced electrocatalysts with enhanced performance toward ORR. Despite the significant progress over the past few decades in improving the catalytic activity and/or durability, none of the Pt-based ORR catalyst is able to fully satisfy the 2017 target recommended by United States DOE. In order to enhance the activity and durability of an ORR catalyst, it is critical to tailor the physicochemical properties of the Pt-based nanoparticles involved including the shape (or facet), elemental composition, and structure. In this dissertation, I describe several strategies for developing advanced ORR catalysts with enhancement in both activity and durability. In addition, I also have investigated the correlation between the physicochemical properties and performance of an ORR catalyst, which is essential to the design of future catalysts.

In Chapter 2, I describe two different protocols for the syntheses of nano-sized Pd@Pt_{nL} (n=2−5) core−shell octahedra based on polyol and aqueous solutions, respectively. The conformal, epitaxial deposition of Pt shells on Pd octahedra could be achieved by carefully controlling the kinetics for both the deposition of Pt atoms and subsequent diffusion of the Pt adatoms. When benchmarked against a commercial Pt/C, the catalyst based on nano-sized Pd@Pt_{nL} octahedra showed great enhancement in terms of both activity and durability toward ORR. DFT calculations were used to understand the enhanced specific activity regarding the Pd@Pt_{nL} octahedra. The improved durability was also systemically investigated by measurements of morphological and compositional changes to the Pd@Pt_{nL} octahedra during an accelerated durability test.

In Chapter 3, I validated a strategy for enhancing the catalytic durability of nano-sized Pt−Ni alloy octahedra toward ORR. Ultrathin, conformal shells of Pt were deposited on the surface of Pt−Ni alloy octahedral nanocrystals in a solution phase. Through passivation of the surface of Pt−Ni octahedral nanocrystals with ultrathin Pt shells, both the chemical stability and electrocatalytic durability were greatly enhanced. Despite the deposition of Pt shells, the remarkably high specific activity of the Pt−Ni octahedra was largely retained.

In Chapter 4, I developed a new ORR catalyst based upon Pt cubic nanoframes composed of thin ridges less than 2 nm in thickness. The Pt cubic nanoframes could be synthesized *via* site-selected deposition of Pt on Pd nanocubes, followed by selective removal of the Pd cores. Owing to open faces and a hollow interior of the Pt cubic nanoframes, the electrocatalyst not only exhibited a greatly increased specific ECSA but also substantially improved durability toward ORR relative to the commercial Pt/C catalyst.

1.4 References

[1] Steele, B. C. H.; Heinzel, A. *Nature* **2001,** *414*, 345−352.

[2] Vielstich, W.; Lamm, A.; Gasteiger, H. A. *Handbook of Fuel Cells−Fundamentals, Technology and Applications*; John Wiley & Sons: Chichester, 2003.

[3] Debe, M. K. *Nature* **2012**, *486*, 43−51.

[4] Gasteiger, H. A.; Kocha, S. S.; Sompalli, B.; Wagner, F. T. *Appl. Catal., B* **2005**, *56*, 9−35.

[5] Shao, M. *Electrocatalysis in Fuel Cells: A Non- and Low-Platinum Approach*; Springer: London, 2013.

[6] Perry, M. L.; Fuller, T. F. J. *Electrochem. Soc.* **2002**, *149*, S59−S67.

[7] Chen, J.; Lim, B.; Lee, E. P., Xia, Y. *Nano Today* **2009**, *4*, 81−95.

[8] Department of Energy. *Multi-Year Research, Development and Demonstration Plan*, http://www.eere.energy.gov, 2012.

[9] Xia, Y.; Xiong, Y.; Lim, B.; Skrabalak, S. E. *Angew. Chem. Int. Ed.* **2009**, *48*, 60−103.

[10] Greeley, J.; Rossmeisl, J.; Hellmann, A.; Nørskov, J. K. *Z. Phys. Chem.* **2007**, *221*, 1209−1220.

[11] Mayrhofer, K. J. J.; Strmcnik, D.; Blizanac, B. B.; Stamenkovic, V.; Arenz, M.; Markovic, N. M. *Electrochim. Acta* **2008**, *53*, 3181−3188.

[12] Rossmeisl, J.; Karlberg, G. S.; Jaramillo, T.; Norskov, J. K. *Faraday Discuss*. **2009**, *140*, 337−346.

[13] de Bruijn, F. A.; Dam, V. A. T.; Janssen, G. J. M. *Fuel Cells* **2008**, *8*, 3−22.

[14] Ferreira, P. J.; la O', G. J.; Shao-Horn, Y.; Morgan, D.; Makharia, R.; Kocha, S.; Gasteiger, H. A. *J. Electrochem. Soc.* **2005**, *152*, A2256−A2271.

[15] Sasaki, K.; Naohara, H.; Cai, Y.; Choi, Y. M.; Liu, P.; Vukmirovic, M. B.; Wang, J. X.; Adzic, R. R. *Angew. Chem. Int. Ed.* **2010**, *49*, 8602−8607.

[16] Marković, N. M.; Ross Jr, P. N. Surf. Sci. Rep. **2002**, *45*, 117−229.

[17] Markovic, N. M.; Gasteiger, H. A.; Ross, P. N. *J. Phys. Chem.* **1995**, *99*, 3411−3415.

[18] Marković, N. M.; Gasteiger, H. A.; Grgur, B. N.; Ross, P. N. *J. Electroanal. Chem.* **1999**, *467*, 157−163.

[19] Stamenkovic, V.; M. Markovic, N.; Ross, P. N. *J. Electroanal. Chem.* **2001**, *500*, 44−51.

[20] Stamenkovic, V. R.; Fowler, B.; Mun, B. S.; Wang, G. F.; Ross, P. N.; Lucas, C. A.; Markovic, N. M. *Science* **2007**, *315*, 493−497.

[21] Zhang, J.; Yang, H.; Fang, J.; Zou, S. *Nano Lett.* **2010**, *10*, 638−644.

[22] Sánchez-Sánchez, C. M.; Solla-Gullón, J.; Vidal-Iglesias, F. J.; Aldaz, A.; Montiel, V.; Herrero, E. *J. Am. Chem. Soc.* **2010**, *132*, 5622−5624.

[23] Rabis, A.; Rodriguez, P.; Schmidt, T. J. *ACS Catal.* **2012**, *2*, 864−890.

[24] Wu, J.; Qi, L.; You, H.; Gross, A.; Li, J.; Yang, H. *J. Am. Chem. Soc.* **2012,** *134*, 11880−11883.

[25] Zhou, W.; Wu, J.; Yang, H. *Nano Lett.* **2013**, *13*, 2870−2874.

[26] Shao, M.; Peles, A.; Odell, J. *J. Phys. Chem. C* **2014,** *118*, 18505−18509.

[27] Sun, X.; Jiang, K.; Zhang, N.; Guo, S.; Huang, X. *ACS Nano* **2015**, *9*, 7634−7640.

[28] Lopes, P. P.; Strmcnik, D.; Tripkovic, D.; Connell, J. G.; Stamenkovic, V.; Markovic, N. M. *ACS Catal.* **2016**, *6*, 2536−2544.

[29] Stamenkovic, V.; Mun, B. S.; Mayrhofer, K. J. J.; Ross, P. N.; Markovic, N. M.; Rossmeisl, J.; Greeley, J.; Nørskov, J. K. *Angew. Chem. Int. Ed.* **2006,** *45*, 2897−2901.

[30] Hammer, B.; Norskov, J. K. *Nature* **1995,** *376*, 238−240.

[31] Greeley, J.; Nørskov, J. K.; Mavrikakis, M. *Annu. Rev. Phys. Chem.* **2002,** *53*, 319−348.

[32] Hammer, B.; Morikawa, Y.; Nørskov, J. K. *Phys. Rev. Lett.* **1996,** *76*, 2141−2144.

[33] Stamenkovic, V. R.; Mun, B. S.; Arenz, M.; Mayrhofer, K. J. J.; Lucas, C. A.; Wang, G.; Ross, P. N.; Markovic, N. M. *Nat. Mater.* **2007,** *6*, 241−247.

[34] Wang, C.; Chi, M.; Wang, G.; van der Vliet, D.; Li, D.; More, K.; Wang, H.-H.; Schlueter, J. A.; Markovic, N. M.; Stamenkovic, V. R. *Adv. Funct. Mater.* **2011**, *21*, 147−152.

[35] Carpenter, M. K.; Moylan, T. E.; Kukreja, R. S.; Atwan, M. H.; Tessema, M. M. *J. Am. Chem. Soc.* **2012,** *134*, 8535−8542.

[36] Cui, C.; Gan, L.; Li, H.-H.; Yu, S.-H.; Heggen, M.; Strasser, P. *Nano Lett.* **2012,** *12*, 5885−5889.

[37] Cui, C.; Gan, L.; Heggen, M.; Rudi, S.; Strasser, P. *Nat. Mater.* **2013,** *12*, 765−771.

[38] Choi, S.-I.; Xie, S.; Shao, M.; Odell, J. H.; Lu, N.; Peng, H.-C.; Protsailo, L.; Guerrero, S.; Park, J.; Xia, X.; Wang, J.; Kim, M. J.; Xia, Y. *Nano Lett.* **2013,** *13*, 3420−3425.

[39] Choi, S.-I.; Xie, S.; Shao, M.; Lu, N.; Guerrero, S.; Odell, J. H.; Park, J.; Wang, J.; Kim, M. J.; Xia, Y. *ChemSuschem* **2014,** *7*, 1476−1483.

[40] Hernandez-Fernandez, P.; Masini, F.; McCarthy, D. N.; Strebel, C. E.; Friebel, D.; Deiana, D.; Malacrida, P.; Nierhoff, A.; Bodin, A.; Wise, A. M.; Nielsen, J. H.; Hansen, T. W.; Nilsson, A.; StephensIfan, E. L.; Chorkendorff, I. *Nat. Chem.* **2014,** *6*, 732−738.

[41] Sun, X.; Jiang, K.; Zhang, N.; Guo, S.; Huang, X. *ACS Nano* **2015**, *9*, 7634−7640.

[42] Arán-Ais, R. M.; Dionigi, F.; Merzdorf, T.; Gocyla, M.; Heggen, M.; Dunin-Borkowski, R. E.; Gliech, M.; Solla-Gullón, J.; Herrero, E.; Feliu, J. M.; Strasser, P. *Nano Lett.* **2015,** *15*, 7473−7480.

[43] Huang, X.; Zhao, Z.; Cao, L.; Chen, Y.; Zhu, E.; Lin, Z.; Li, M.; Yan, A.; Zettl, A.; Wang, Y. M.; Duan, X.; Mueller, T.; Huang, Y. *Science* **2015,** *348*, 1230−1234.

[44] Zhang, J.; Mo, Y.; Vukmirovic, M. B.; Klie, R.; Sasaki, K.; Adzic, R. R. *J. Phys. Chem. B* **2004,** *108*, 10955−10964.

[45] Zhang, J.; Lima, F. H. B.; Shao, M. H.; Sasaki, K.; Wang, J. X.; Hanson, J.; Adzic, R. R. *J. Phys. Chem. B* **2005,** *109*, 22701−22704.

[46] Wang, C.; Chi, M.; Li, D.; Strmcnik, D.; van der Vliet, D.; Wang, G.; Komanicky, V.; Chang, K.-C.; Paulikas, A. P.; Tripkovic, D.; Pearson, J.; More, K. L.; Markovic, N. M.; Stamenkovic, V. R. *J. Am. Chem. Soc.* **2011,** *133*, 14396−14403.

[47] Shao, M.; Peles, A.; Shoemaker, K.; Gummalla, M.; Njoki, P. N.; Luo, J.; Zhong, C.-J. *J. Phys. Chem. Lett.* **2011,** *2*, 67−72.

[48] Sasaki, K.; Naohara, H.; Choi, Y.; Cai, Y.; Chen, W.-F.; Liu, P.; Adzic, R. R. *Nat. Commun.* **2012,** *3*, 1115.

[49] Shao, M.; He, G.; Peles, A.; Odell, J. H.; Zeng, J.; Su, D.; Tao, J.; Yu, T.; Zhu, Y.; Xia, Y. *Chem. Commun.* **2013,** *49*, 9030−9032.

[50] Hsieh, Y.-C.; Zhang, Y.; Su, D.; Volkov, V.; Si, R.; Wu, L.; Zhu, Y.; An, W.; Liu, P.; He, P.; Ye, S.; Adzic, R. R.; Wang, J. X. *Nat. Commun.* **2013,** *4*, 2466.

[51] Wang, G.; Huang, B.; Xiao, L.; Ren, Z.; Chen, H.; Wang, D.; Abruña, H. D.; Lu, J.; Zhuang, L. *J. Am. Chem. Soc.* **2014,** *136*, 9643−9649.

[52] Choi, S.-I.; Shao, M.; Lu, N.; Ruditskiy, A.; Peng, H.-C.; Park, J.; Guerrero, S.; Wang, J.; Kim, M. J.; Xia, Y. *ACS Nano* **2014,** *8*, 10363−10371.

[53] Xie, S.; Choi, S.-I.; Lu, N.; Roling, L. T.; Herron, J. A.; Zhang, L.; Park, J.; Wang, J.; Kim, M. J.; Xie, Z.; Mavrikakis, M.; Xia, Y. *Nano Lett.* **2014,** *14*, 3570−3576.

[54] Park, J.; Zhang, L.; Choi, S.-I.; Roling, L. T.; Lu, N.; Herron, J. A.; Xie, S.; Wang, J.; Kim, M. J.; Mavrikakis, M.; Xia, Y. *ACS Nano* **2015,** *9*, 2635−2647.

[55] Wang, X.; Choi, S.-I.; Roling, L. T.; Luo, M.; Ma, C.; Zhang, L.; Chi, M.; Liu, J.; Xie, Z.; Herron, J. A.; Mavrikakis, M.; Xia, Y. *Nat. Commun.* **2015,** *6*, 7594.

[56] Wang, X.; Vara, M.; Luo, M.; Huang, H.; Ruditskiy, A.; Park, J.; Bao, S.; Liu, J.; Howe, J.; Chi, M.; Xie, Z.; Xia, Y. *J. Am. Chem. Soc.* **2015,** *137*, 15036−15042.

[57] Tian, X.; Luo, J.; Nan, H.; Zou, H.; Chen, R.; Shu, T.; Li, X.; Li, Y.; Song, H.; Liao, S.; Adzic, R. R. *J. Am. Chem. Soc.* **2016,** *138*, 1575−1583.

[58] Shen, L.-L.; Zhang, G.-R.; Miao, S.; Liu, J.; Xu, B.-Q. *ACS Catal.* **2016,** *6*, 1680−1690.

[59] Zhang, L.; Zhu, S.; Chang, Q.; Su, D.; Yue, J.; Du, Z.; Shao, M. *ACS Catal.* **2016**, *6*, 3428−3432.

[60] Lim, B.; Jiang, M.; Camargo, P. H. C.; Cho, E. C.; Tao, J.; Lu, X.; Zhu, Y.; Xia, Y. *Science* **2009,** *324*, 1302−1305.

[61] Zhang, L.; Roling, L. T.; Wang, X.; Vara, M.; Chi, M.; Liu, J.; Choi, S.-I.; Park, J.; Herron, J. A.; Xie, Z.; Mavrikakis, M.; Xia, Y. *Science* **2015,** *349*, 412−416.

[62] Wang, X.; Figueroa-Cosme, L.; Yang, X.; Luo, M.; Liu, J.; Xie, Z.; Xia, Y. *Nano Lett.* **2016,** *16*, 1467−1471.

[63] He, D. S.; He, D.; Wang, J.; Lin, Y.; Yin, P.; Hong, X.; Wu, Y.; Li, Y. *J. Am. Chem. Soc.* **2016,** *138*, 1494−1497.

[64] Chen, C.; Kang, Y.; Huo, Z.; Zhu, Z.; Huang, W.; Xin, H. L.; Snyder, J. D.; Li, D.; Herron, J. A.; Mavrikakis, M.; Chi, M.; More, K. L.; Li, Y.; Markovic, N. M.; Somorjai, G. A.; Yang, P.; Stamenkovic, V. R. *Science* **2014,** *343*, 1339−1343.

[65] Becknell, N.; Kang, Y.; Chen, C.; Resasco, J.; Kornienko, N.; Guo, J.; Markovic, N. M.; Somorjai, G. A.; Stamenkovic, V. R.; Yang, P. *J. Am. Chem. Soc.* **2015,** *137*, 15817−15824.

[66] Fang, Z.; Wang, Y.; Liu, C.; Chen, S.; Sang, W.; Wang, C.; Zeng, J. *Small* **2015,** *11*, 2593−2605.

CHAPTER 2

ATOMIC LAYER-BY-LAYER DEPOSITION OF PLATINUM ON PALLADIUM OCTAHEDRA FOR ENHANCED CATALYSTS TOWARD OXYGEN REDUCTION

2.1 Introduction

As described in Chapter 1, the activity and durability of a catalyst for the ORR can be improved by engineering the size, shape, structure, and composition of the nanoparticles involved [1−12]. To this end, Pt-based bimetallic nanoparticles have been demonstrated with remarkable performance in catalyzing ORR [5−12]. The bimetallic nanoparticles have been synthesized with a number of different structures, including alloy [6−8], dendrite [9], and core−shell [10−12]. Among them, deposition of a few atomic layers of Pt on the surface of facet-controlled nanocrystals made of another metal such as Pd offers an attractive strategy for maximizing the activity in terms of Pt mass [13]. This strategy can reduce the materials cost of a catalyst by replacing the Pt in the core with a much less expensive metal [5]. It can also retain the dispersion of Pt atoms while increasing the durability of a catalyst by switching to nanoparticles with larger sizes. In addition, the inclusion of a different metal can alter the electronic structure of Pt through ligand and strain effects, leading to potential enhancement in specific activity [17, 14−19].

In 2014, our group successfully synthesized Pd@Pt_{nL} core−shell nanocubes *via* conformal, epitaxial deposition of Pt on Pd nanocubes, where the number (n) of Pt atomic layers could be precisely controlled from a monolayer to multiple layers [20]. When compared to a commercial Pt/C catalyst, the Pd@Pt_{nL} nanocubes showed enhancement in both mass activity (by 3-fold) and durability toward ORR. Because the Pt atoms were well-dispersed on the surfaces of the Pd cores as ultrathin shells, the Pd@Pt_{nL} nanocubes exhibited higher specific ECSAs than the Pt/C reference despite their marked difference in particle size (21 nm *vs* 3.2 nm). The high dispersion of Pt atoms made a critical

contribution to the enhancement in mass activity. While this prior work demonstrated the feasibility to improve the catalytic performance, the cubic shape is not an optimal choice for the development of effective ORR catalysts. For ORR catalysts based upon Pt, previous studies have established that the (111) surface has a specific activity at least 2-fold higher than that of the (100) surface [21−23]. As a result, there exists a strong incentive to epitaxially deposit Pt atoms as atomic overlayers on Pd octahedra to achieve a higher electrocatalytic activity than what was previously reported for the cubic system.

The synthesis of Pd@Pt core−shell nanocrystals *via* seeded growth typically suffers from an island growth mode or self-nucleation for the Pt atoms because the bond energy of Pt−Pt (307 kJ mol^{-1}) is much greater than that of Pd−Pt (191 kJ mol^{-1}) [9]. It has been reported that monolayers or submonolayers of Pt could be deposited on Pd nanocrystals using an electrochemical approach by taking advantage of the galvanic replacement reaction between the underpotentially deposited monolayers of Cu and a Pt(II) precursor [24, 25]. The capability of this method will be limited in terms of scale-up production due to the involvement of electrodes in the deposition process. Using a different approach, the Xia group demonstrated that Pt atoms could be deposited as uniform, conformal, ultrathin overlayers on Pd nanocubes *via* a solution-phase process that involves the use of a polyol such as EG [20, 26]. At a relatively high reaction temperature of 200 ^{o}C, the deposited Pt atoms could be promoted to diffuse across the Pd surface to generate Pt shells in a layer-by-layer fashion. In principle, this protocol could be extended to generate conformal shells of Pt on Pd octahedra. However, because Pd(111) has a much lower surface free energy than Pd(100), it is anticipated that the original deposition protocol would be complicated by the self-nucleation of Pt atoms [27].

In this chaper, I compare two different protocols based upon polyol and aqueous solutions for the epitaxial, conformal deposition of Pt on Pd octahedra to generate Pd@Pt_{nL} octahedra (n = 2−5). For the polyol-based system, I simply used the protocol developed for the Pd@Pt_{nL} nanocubes [20] with a minor modification to address the self-

nucleation issue by decreasing the concentration of the Pt(IV) precursor. When switched to an aqueous system, I could achieve similar conformal deposition of Pt on Pd octahedra at a much lower temperature (95 *vs* 200 ^{o}C), which should be more attractive as a cost-saving and environment-friendly process [28]. To avoid self-nucleation for the newly formed Pt atoms in an aqueous system, I employed a mild reducing agent to slow down the reduction of a Pt(II) precursor. Prior to the synthesis of Pd@Pt_{nL} octahedra, my collaborators performed periodic, self-consistent DFT calculations using extended surface models of the nanocrystal terraces. The calculation results confirmed that the Pd@Pt_{nL} (n = 2−5) octahedra indeed had higher specific activity than both the commercial Pt/C catalyst and Pd@Pt_{nL} (n = 2−5) nanocubes [20], owing to the increased destabilization of OH on the surfaces of the Pd@Pt_{nL} octahedra. Experimentally, I demonstrated that both the specific and mass activities of the Pd@Pt_{nL} octahedra were greatly enhanced relative to the commercial Pt/C. The Pd@Pt_{nL} octahedra also exhibited substantial improvement in durability toward ORR when compared to the Pt/C. The improved durability can be attributed to a greatly enlarged size for the Pd@Pt_{nL} octahedra (21 nm *vs* 3.2 nm) as well as the sacrificial role of the Pd core in a corrosive condition.

2.2 Results and Discussion

Comparison of the ORR Activities of Pd@Pt_{nL} (n = 2−5) Octahedra by DFT Calculation. Before conducting the synthesis, the ORR activities of Pd@Pt_{nL} (n = 2−5) octahedra were compared by computing the energetics of oxygen reduction on model surfaces using periodic, self-consistent DFT by Mavrikakis and co-workers (see Section 2.5 for details). Specifically, the Pd@Pt_{nL} octahedra were modeled as Pt_{nL}*/Pd(111) extended surfaces, whereas Pt solid octahedra were represented by the Pt(111) surface. Due to the compositional instability associated with the Pt_{1L}*/Pd(111) surface (Figure 2.1), I decided not to consider Pd@Pt_{1L} octahedra in the present work. Mavrikakis and

co-workers obtained the reaction thermochemistry (Table 2.1) at 0.9 V_{RHE} (with reference to the reversible hydrogen electrode, RHE) from the computed binding energies (Table 2.2) [29]. On the basis of the reaction thermochemistry [30], it can be concluded that the rate-limiting step is $OH^* + H^+ + e^- \rightarrow H_2O$ for all these systems. I also noted that the reaction energy for this step is determined by the binding energy of OH, and the reaction endothermicity rises with increasing the absolute binding energy of OH. This analysis indicates that this step becomes more facilitated on Pt_{nL}*/Pd(111) (n = 2−5) than Pt(111). In addition, prior theoretical calculations and experimental measurements indicate that the specific ORR activity of Pt(111) is higher than that of Pt(100) in the presence of a non-adsorbing electrolyte such as $HClO_4$ [21−23]. As shown in Figure 2.2, the calculation results clearly indicated that each of the Pt_{nL}*/Pd(111) (n = 2−5) surfaces had a higher specific activity than pure Pt(111). As a result, the Pd@Pt_{nL} (n = 2−5) octahedra were anticipated to exhibit enhanced specific ORR activity relative to Pt octahedra. It is worth noting note that the relative ordering of activities for the 2L, 3L, and 4L model surfaces follows the trend for the d_z^2-band center, which, in turn, determines the binding energy of OH on these surfaces (Table 2.3). It is nontrivial to deconvolute the lattice strain effect from the ligand effect on the binding energy of OH; however, results in this study suggest that both effects are important in enhancing the ORR specific activity (Table 2.2). The minor lattice compression imposed by the deposition of Pt atoms on a lattice of slightly smaller Pd atoms causes destabilization of OH, while electronic interactions between the Pd substrate and the Pt overlayers can modulate the OH binding energy depending on the number of Pt layers. Since the Pt atoms of a core−shell nanocrystal are much better dispersed than those of a Pt solid octahedron with a similar size, all the Pd@Pt_{nL} (n = 2−5) octahedra should exhibit greatly enhanced mass activity in terms of Pt. Furthermore, each Pd@Pt_{nL} nanocrystal should be less expensive than a solid Pt octahedron with a similar size because the current price of Pd is only half that of Pt. Taken together, there is a strong incentive to synthesize Pd@Pt_{nL} (n = 2−5) octahedra

and explore them as a new class of ORR catalysts.

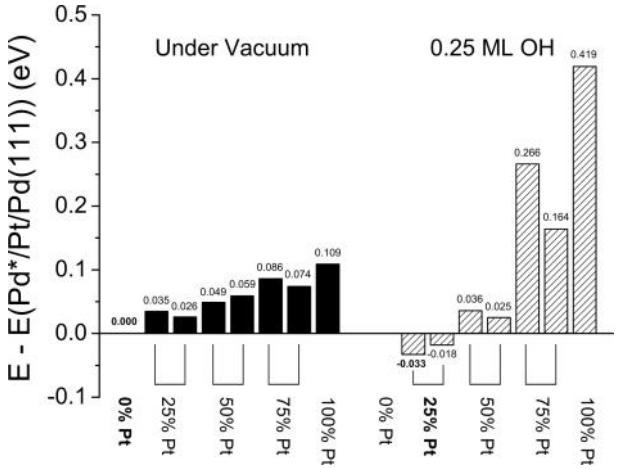

Figure 2.1. Thermodynamic stability of Pt_{1L}*/Pd(111) calculated under vacuum and in the presence of 0.25 ML OH for the top layer with different compositions. The stability were shown as difference in the total energies between the system with the listed surface composition (% Pt) and the reference state (0% Pt), which is all Pt atoms on the top layer were replaced by Pd atoms of the second layer (Pd*/Pt/Pd(111)). The energy of the Pd-terminated surface is equal to 0 (the reference state). Negative values correspond to more stable configurations while positive values correspond to less stable states. The most stable configuration in each case is indicated using bold letters. Two permutations were considered for 25, 50, and 75% Pt. (Reprinted with permission from [57]. Copyright 2015 American Chemical Society.)

Table 2.1. Free energies (ΔG) for the hydrogenation of the adsorbed oxygen (O) and hydroxyl (OH) at 0.9 V_{RHE} and 298 K calculated for the model surfaces using DFT.

n of Pt atomic layers	ΔG of the reaction (eV)			
	Pt_{nL}*/Pd (100)[a]		Pt_{nL}*/Pd (111)	
	$O^* + H^+ + e^- \rightarrow OH^*$	$OH^* + H^+ + e^- \rightarrow H_2O + *$	$O^* + H^+ + e^- \rightarrow OH^*$	$OH^* + H^+ + e^- \rightarrow H_2O + *$
2	0.015	0.459	0.125	0.349
3	0.008	0.460	0.117	0.356
4	0.011	0.468	0.114	0.347
5	0.012	0.475	0.110	0.351
Pure Pt	0.015	0.487	0.123	0.363

[a] The values were taken from the recent publication by Xia *et al*. [20], and included here for the purpose of comparison.

Table 2.2. Binding energies of O and OH on the model surfaces at 0.25 ML coverage derived from DFT calculations.

n of Pt atomic layers	Binding energy (eV)			
	Pt_{nL}*/Pd (100)[a]		Pt_{nL}*/Pd (111)	
	O	OH	O	OH
2	-3.844	-2.695	-3.867	-2.138
3	-3.838	-2.696	-3.867	-2.145
4	-3.850	-2.705	-3.855	-2.136
5	-3.858	-2.712	-3.855	-2.140
Pure Pt	-3.873	-2.724	-3.879	-2.152
Compressed Pt	-	-	-	-2.144

[a] The values were taken from the recent publication by Xia *et al*. [20], and included here for the purpose of comparison.

Table 2.3. Center of d_z^2-bands for the model surfaces at 0.25 ML coverage of OH as derived from DFT calculations.

n of Pt atomic layers	$\varepsilon_{dz2} - \varepsilon_f$ (eV)
2	-2.480
3	-2.478
4	-2.485

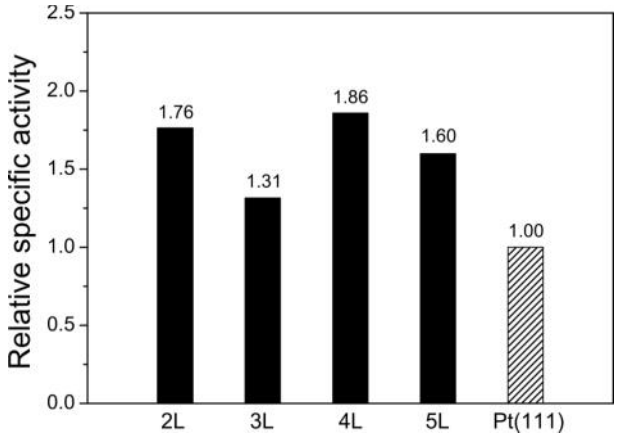

Figure 2.2. Relative specific activities of Pd@Pt_{nL} (n = 2−5) octahedra at 0.9 V_{RHE} that were calculated using Pt_{nL}*/Pd(111) model surfaces by DFT. All values are presented relative to Pt(111). All the catalysts based upon Pd@Pt_{nL} (n = 2−5) octahedra are anticipated to exhibit improved specific activity relative to Pt octahedra, which are represented by Pt(111). (Reprinted with permission from [57]. Copyright 2015 American Chemical Society.)

Comparison of Two Different Protocols for the Syntheses of Pd@Pt_{nL} Octahedra. Figure 2.3 shows a schematic illustration of the polyol- and water-based protocols for the syntheses of Pd@Pt_{nL} octahedra. Both systems involved the use of Pd octahedra with slight truncation at corner sites as the seeds (see Figure 2.4 for typical TEM images). In general, Pd is a good substrate for the epitaxial overgrowth of Pt due to their close match in lattice constant. However, due to a lower surface free energy of Pd(111) relative to Pd(100), it has been difficult to completely prevent the newly formed Pt atoms from self-nucleating in an attempt to obtain Pd@Pt_{nL} octahedra in high purity. This problem was found to be particularly serious when I was trying to directly use the polyol-based protocol developed for coating Pt on Pd cubic seeds (Figure 2.5) [20]. This issue could be addressed by reducing the concentration of the Na_2PtCl_6 precursor solution. Due to the use of a relatively high temperature of 200 ^oC, the Pd@Pt_{nL} octahedra tended to be truncated at the corner sites, just like the original Pd octahedral seeds. The presence of Pt{100} facets at the corner sites is expected to compromise the specific ORR activity of the resultant nanocrystals.

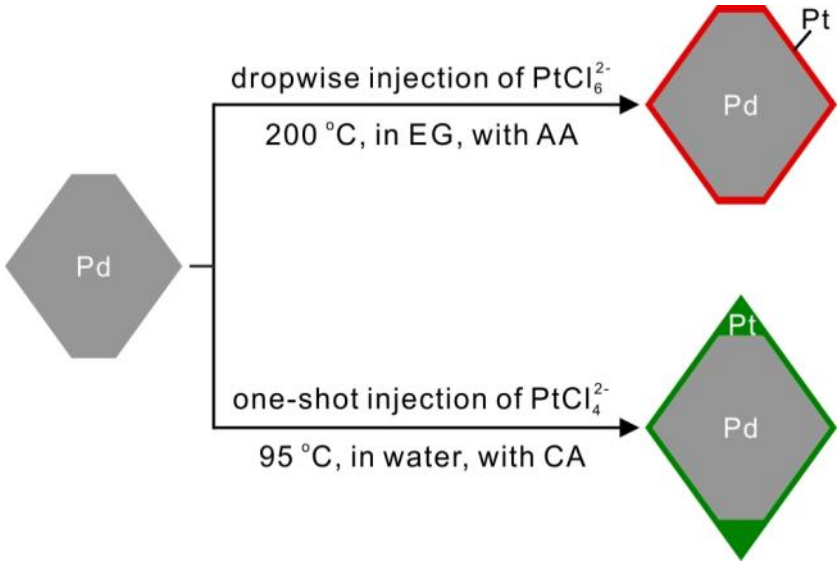

Figure 2.3. Schematic diagram showing the syntheses of Pd@Pt_{nL} octahedra *via* two different routes involving polyol and water, respectively. For the synthesis in polyol, a Na_2PtCl_6 solution in EG is titrated dropwise into the reaction solution at 200 °C. Due to the use of a relatively high temperature, the core−shell octahedra show truncation at the corners, just like the original Pd seeds. For the synthesis in water, an aqueous solution of K_2PtCl_4 is added in one shot into the reaction solution at 95 °C. The use of a much lower reaction temperature results in the formation of Pd@Pt_{nL} octahedra with sharper corners than the products of a polyol synthesis. (Reprinted with permission from [57]. Copyright 2015 American Chemical Society.)

In addition to the use of polyol and a relatively high reaction temperature, I also tried a water-based protocol conducted at a much lower temperature for the synthesis of Pd@Pt_{nL} octahedra. Unlike the synthesis of Pd@Pt_{nL} cubes, which has to be carried out in a polyol at 200 °C, I could achieve conformal deposition of Pt on Pd octahedra in water at a temperature as low as 95 °C. Related to the issue of temperature, I used DFT calculations (see Section 2.5 for details) with the assistance from Mavrikakis and co-workers to compare the activation energy barriers for a Pt adatom to diffuse across Pd(111) and Pd(100) surfaces, respectively. It was found that the barrier was only 0.16 eV on Pd(111), while it was increased by almost 7-fold to 1.06 eV on Pd(100). This result confirms the feasibility to achieve a uniform, conformal coating of Pt on a Pd octahedron *via* surface diffusion at a much lower temperature as compared to the coating of a Pd

cube. In the case of water-based synthesis, I also observed sharpening of corners for the core−shell nanocrystals due to the use of a much lower temperature relative to the polyol-based system. To address the self-nucleation issue in the water-based system, I used a weak reducing agent such as CA to slow down the reduction of a Pt(II) precursor. By doing so, I could even introduce the Pt(II) precursor in one shot and still obtain Pd@Pt_{nL} octahedra with a purity approaching 100%. The introduction of precursor in one shot represents another advantage for the possible extension of this protocol to a droplet-based system for the purpose of continuous, scalable production [31].

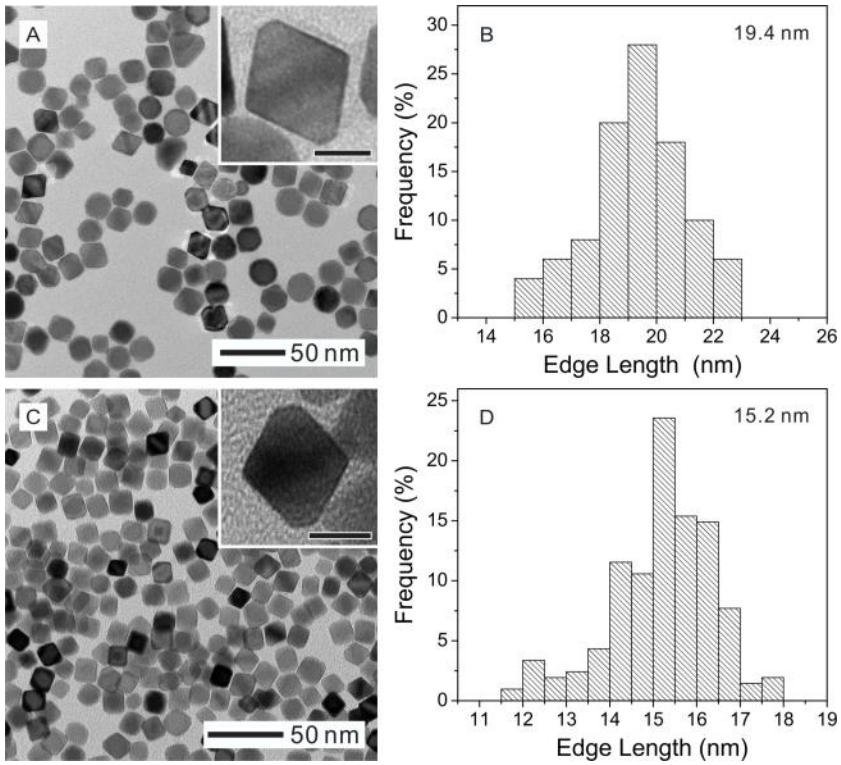

Figure 2.4. (A, C) TEM images and (B, D) size distributions of the Pd octahedra used as seeds for the synthesis of Pd@Pt_{nL} octahedra. The insets show TEM images of the Pd octahedron at a higher magnification (scale bar: 10 nm). (Reprinted with permission from [57]. Copyright 2015 American Chemical Society.)

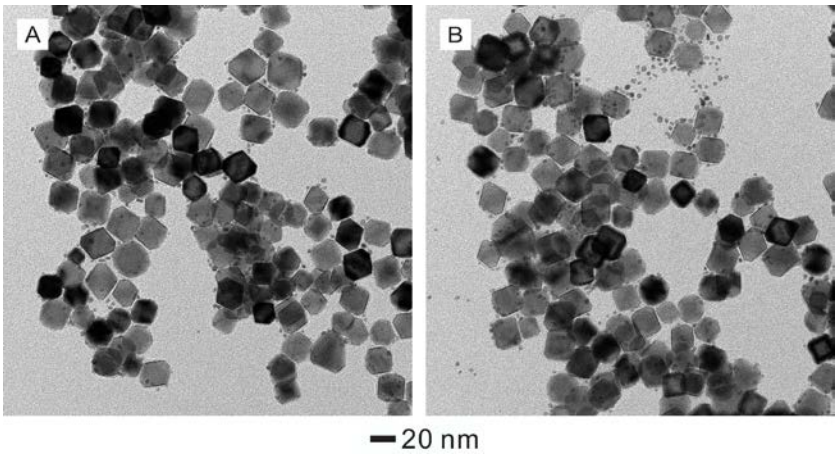

Figure 2.5. TEM images of the products obtained using the polyol procedure reported for the synthesis of Pd@$Pt_{2–3L}$ cubes [20]. In this case, I only replaced the Pd cubic seeds with Pd octahedral seeds with all other parameters kept the same as the standard protocol. (Reprinted with permission from [57]. Copyright 2015 American Chemical Society.)

Synthesis of Pd@Pt_{nL} Octahedra Using the Polyol-Based Protocol. For the polyol-based system, I used Pd octahedra with slight truncation at corner sites as the seeds (Figure 2.4A). The synthesis was conducted by slowly injecting the Na_2PtCl_6 precursor solution into EG containing PVP, KBr, AA, and the Pd seeds at 200 ^oC under magnetic stirring. Similar to the previous work reported in [20], the thickness of the Pt shells could be readily controlled with atomic precision by changing the amount of Pt(IV) precursor added into the growth solution. Figure 2.6 shows TEM images of the Pd@Pt_{nL} octahedra obtained using the polyol-based protocol. The number of Pt atomic layers increased up to five by increasing the volume of the precursor solution from 12.0 to 16.0 and 22.0 mL, respectively. Specifically, the samples shown in Figure 2.6 correspond to Pd@$Pt_{2–3L}$, Pd@$Pt_{3–4L}$, and Pd@$Pt_{4–5L}$ octahedra. I determined the average number (n) of Pt atomic layers for the Pd@Pt_{nL} octahedra using ICP-MS. As shown in Table 2.4, the average numbers of Pt atomic layers were 2.2, 3.4, and 4.3, respectively, for these three samples. The TEM images indicate that all the samples of Pd@Pt_{nL} (n = 2−5) octahedra were covered by smooth surfaces due to the uniform, conformal deposition of Pt atoms.

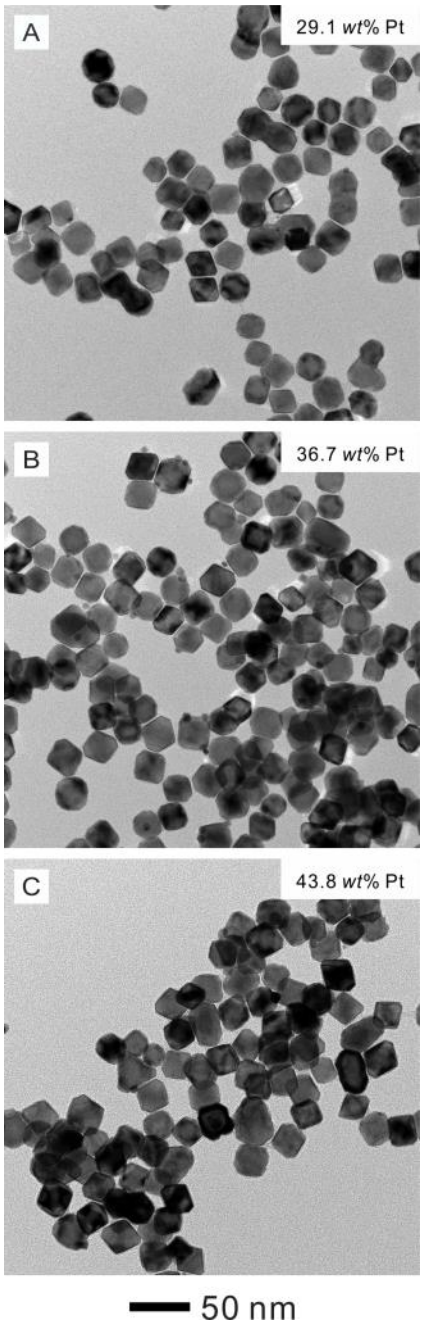

Figure 2.6. TEM images of $Pd@Pt_{nL}$ octahedra synthesized using the polyol-based protocol: (A) $Pd@Pt_{2–3L}$, (B)$Pd@Pt_{3–4L}$, and (C) $Pd@Pt_{4–5L}$ octahedra. The volumes of the Na_2PtCl_6 solution (0.10 mg mL^{-1}) added into the reaction solution were 12.0, 16.0, and 22.0 mL, respectively. The number (n) of Pt atomic layers was derived from the ICP-MS data. For each sample, the Pt content (wt%) from ICP-MS analysis is shown in the inset. (Reprinted with permission from [57]. Copyright 2015 American Chemical Society.)

Table 2.4. The average number (n) of the Pt atomic layers calculated from the Pd and Pt contents in the Pd@Pt_{nL} octahedra. The metal contents were determined using ICP-MS while the size of the Pd octahedra was derived from TEM.

Sample	m_{Pt}/m_{Pd} [a]	Thickness of Pt shell (nm)	Calculated number of Pt atomic layers	number of Pt atomic layers for notation	Synthesis method
Pd@Pt_{2-3L}	0.41	0.50	2.21	2−3	Polyol-based system
Pd@Pt_{3-4L}	0.58	0.74	3.36	3−4	
Pd@Pt_{4-5L}	0.78	0.97	4.29	4−5	
Pd@Pt_{2-3L}	0.41	0.56	2.47	2−3	Water-based system

[a] The m_{Pt} and m_{Pd} represent content of Pt and Pd in the Pd@Pt_{nL} octahedra (in wt%).

Figure 2.7, A−E, shows HAADF-STEM images of the Pd@Pt_{2-3L} octahedra, confirming that the Pt atoms were uniformly deposited on the surfaces of the Pd seeds. In particular, Figure 2.7B shows that the truncated corners of the Pd seeds were largely preserved during the deposition of Pt. Interestingly, more atomic layers of Pt were deposited at the corner sites than on the side faces. This difference indicates that the Pt atoms preferred to be deposited onto the {100} facets at the corner sites relative to the {111} facets on the side faces, which could be attributed to the difference in surface free energy or atom coordination number [27]. I could observe some surface defects such as steps and vacancy sites on the surface of the Pt shell. Such defects are typically associated with crystal growth in a solution phase *via* a layer-by-layer mechanism [32], as

well as thin film deposition in a gas phase [33]. The observation of such surface defects also supports the claim that the Pt shell was formed in a layer-by-layer fashion due to the slow injection of the Pt precursor and the involvement of a relatively high temperature. Figure 2.7F shows EDX line scan profiles along the red arrow marked in Figure 2.7E, further confirming the core−shell structure observed in the STEM images. I also characterized the Pd@$Pt_{3–4L}$ and Pd@$Pt_{4–5L}$ octahedra by STEM, and representative images can be found in Figure 2.8. In general, it is hard to measure the exact number of Pt overlayers on a Pd octahedron due to the complication of orientation (which is different from a cubic system). These STEM images still offer some useful information to support the core−shell structure claimed for these bimetallic nanocrystals.

Electrocatalytic Measurements of the Pd@Pt_{nL} Octahedra Synthesized in Polyol. Prior to electrochemical measurements, the Pd@Pt_{nL} octahedra were dispersed onto carbon to obtain Pd@Pt_{nL}/C catalysts (Figure 2.9, C−E). The catalysts were then treated with acetic acid at 60 ^{o}C for 2 h to remove residual PVP or bromide ions possibly adsorbed on the surface (Figure 2.10). Figure 2.11A shows CVs of the catalysts obtained at room temperature in a N_2-saturated aqueous $HClO_4$ solution (0.1 M). Table 2.5 shows specific ECSAs of the catalysts derived from the charges associated with the desorption peaks of the underpotentially deposited hydrogen. It is worth noting that the specific ECSAs of the Pd@Pt_{nL}/C were comparable to or even higher than that of the Pt/C, although their particles were much greater in terms of size (21 *vs* 3.2 nm). This result implies that the Pt atoms in the Pd@Pt_{nL} octahedra were better dispersed on the surface than those in the 3.2-nm particles of Pt/C when they were deposited as ultrathin shells of only a few atomic layers thick.

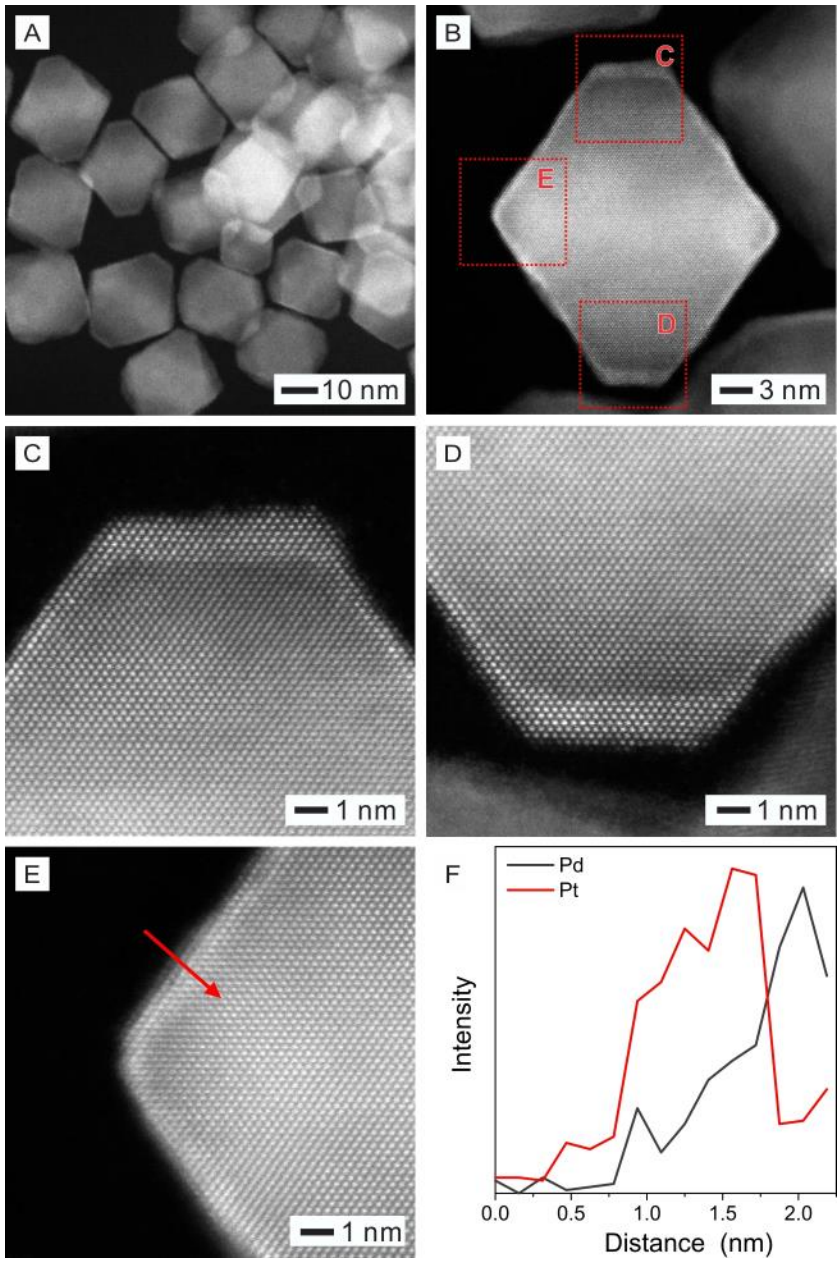

Figure 2.7. (A−E) HAADF-STEM images of the Pd@$Pt_{2–3L}$ octahedra synthesized using the polyol-based protocol. In the STEM images, the dark and bright regions correspond to Pd and Pt, respectively. (F) EDX line scan profiles of Pd and Pt for the Pd@$Pt_{2–3L}$ octahedron along the red arrow marked in (E). (Reprinted with permission from [57]. Copyright 2015 American Chemical Society.)

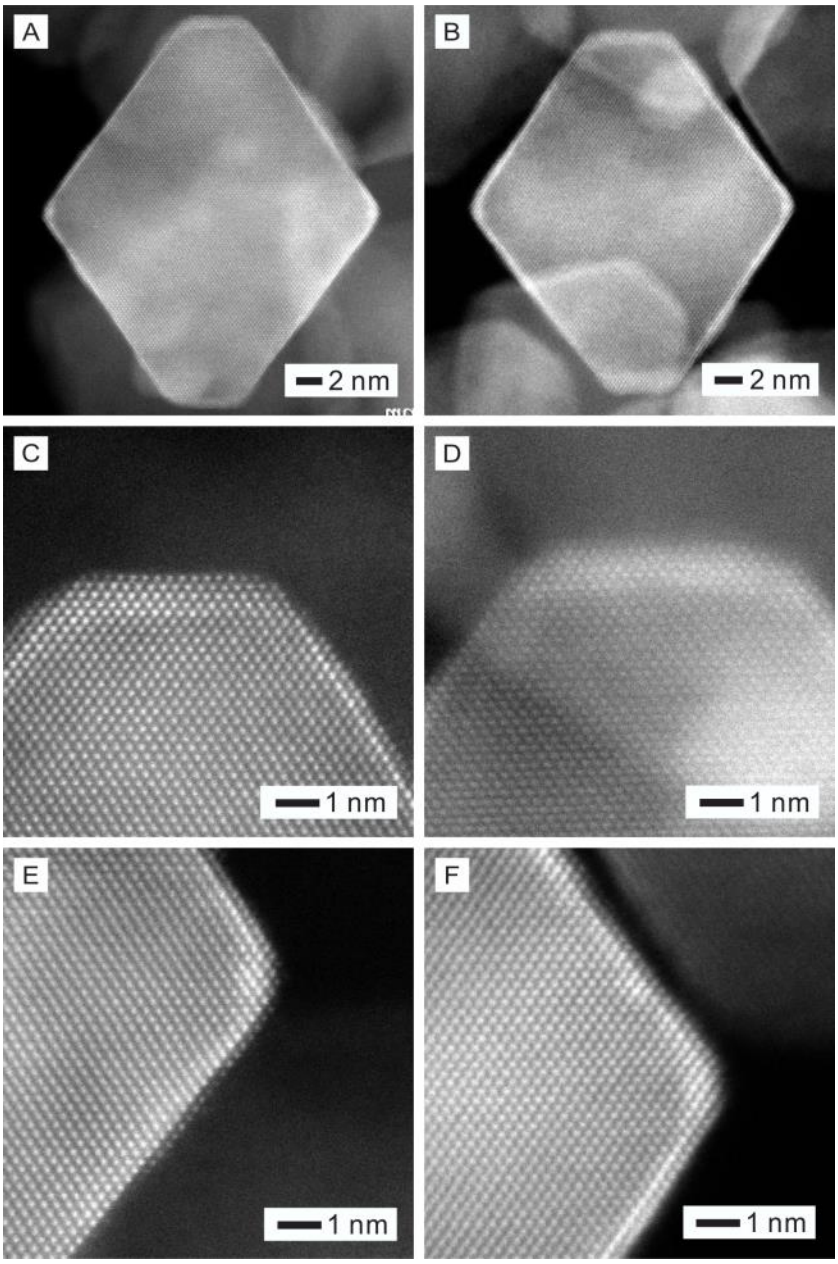

Figure 2.8. HAADF-STEM images of the $Pd@Pt_{nL}$ octahedra synthesized using the polyol-based protocol: (A, C, E) $Pd@Pt_{3–4L}$ and (B, D, F) $Pd@Pt_{4–5L}$ octahedra. (Reprinted with permission from [57]. Copyright 2015 American Chemical Society.)

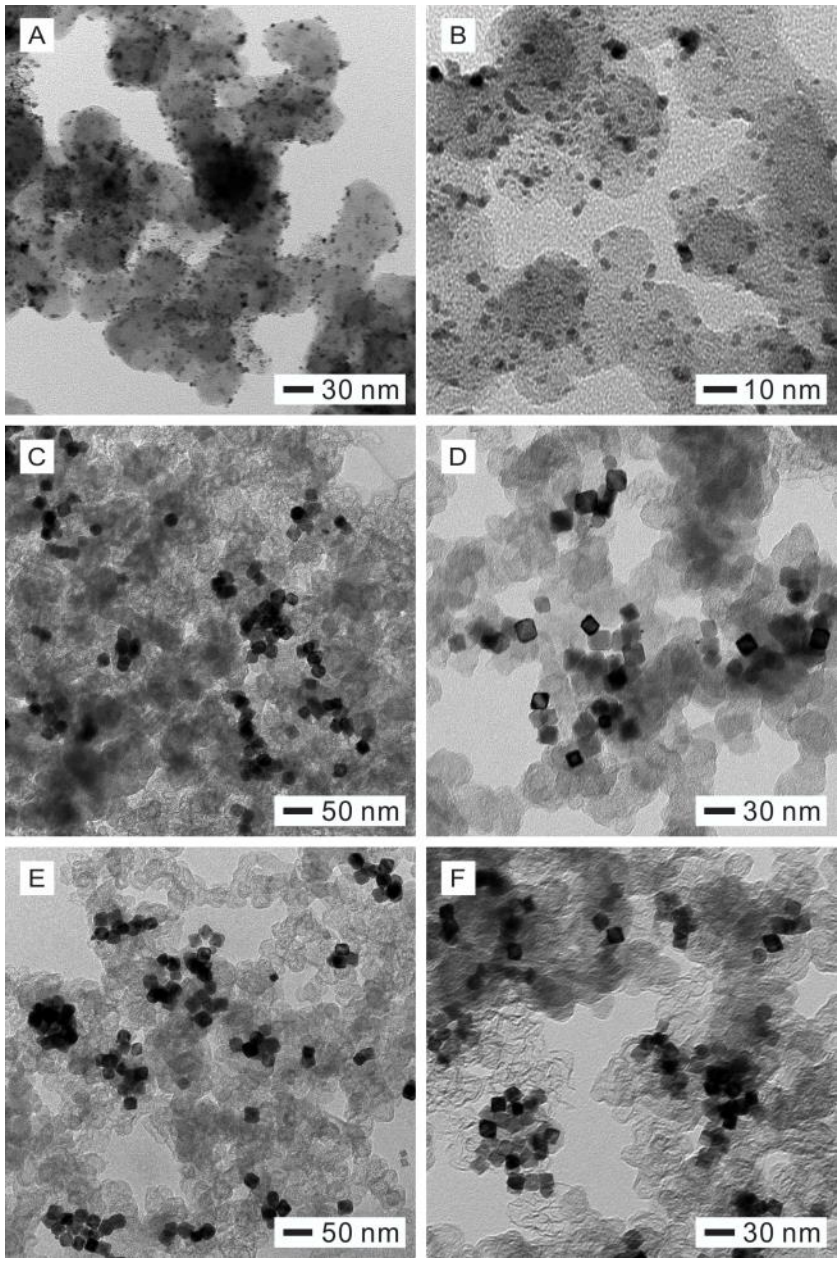

Figure 2.9. TEM images of the (A, B) Pt/C and (C−F) Pd@Pt_{nL}/C catalysts. The Pd@$Pt_{2–3L}$, Pd@$Pt_{3–4L}$, and Pd@$Pt_{4–5L}$ octahedra shown in (C−E) were synthesized *via* the polyol-based protocol while the Pd@$Pt_{2–3L}$ octahedra in (F) were synthesized *via* the water-based protocol. (Reprinted with permission from [57]. Copyright 2015 American Chemical Society.)

I then measured the ORR current densities of the Pd@Pt_{nL}/C and Pt/C catalysts at room temperature in an O_2-saturated aqueous $HClO_4$ solution (0.1 M) with a rotation speed of 1,600 rpm for the working electrode (Figure 2.11B). From each polarization curve, I calculated the kinetic current density (j_k) for ORR using the Koutecky−Levich equation and then normalized it to the ECSA for specific activity ($j_{k,specific}$, Figure 2.11C) and to the Pt mass for the mass activity ($j_{k,mass}$, Figure 2.11D). To quantitatively understand their performance for ORR, I took the values of both specific and mass activities at 0.9 V_{RHE} and plotted them in Figure 2.11, E and F, relative to those of Pt/C. All the Pd@Pt_{nL}/C catalysts exhibited around 4-fold enhancement in specific activity relative to Pt/C (Table 2.5). Such an enhancement in specific activity could be attributed to a combination of the enlargement in proportion of the {111} facets on the surface and the electronic coupling between Pd and Pt.

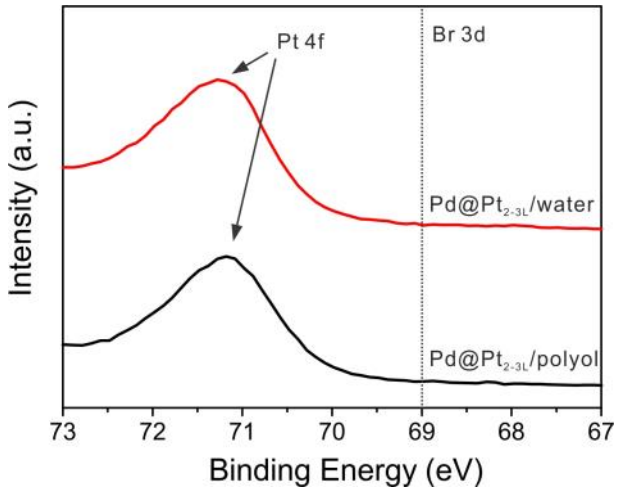

Figure 2.10. X-ray photoelectron spectra of the Pd@Pt_{2-3L} octahedra prepared using the polyol- (black) and water-based protocols (red), respectively. (Reprinted with permission from [57]. Copyright 2015 American Chemical Society.)

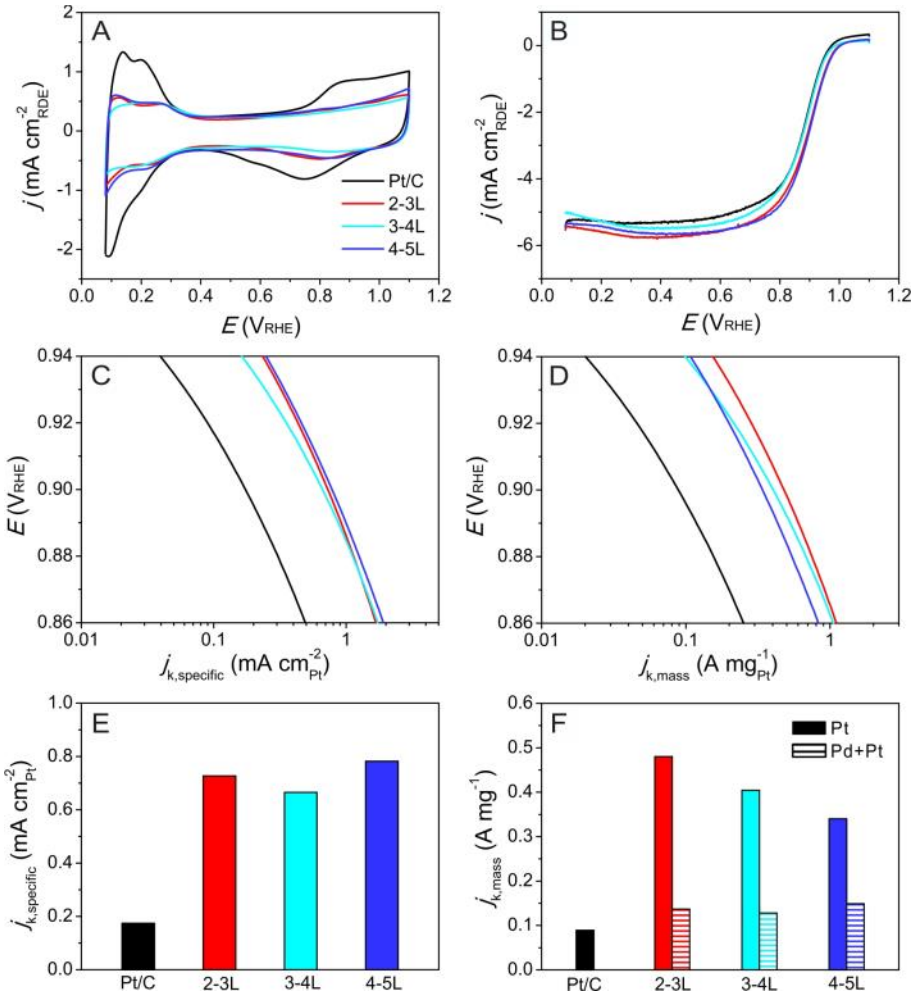

Figure 2.11. (A) CVs and (B) ORR polarization curves for the Pd@Pt_{nL}/C and commercial Pt/C catalysts. The Pd@Pt_{nL} octahedra were synthesized using the standard, polyol-based protocol. The current densities (*j*) were normalized against the geometric area of RDE (0.196 cm^2). (C) Specific and (D) mass activities given as kinetic current densities (j_k) normalized against the ECSA of the catalyst and the mass of Pt, respectively. (E) Specific and (F) mass activities (normalized against the masses of Pt and Pd+Pt, respectively) at 0.9 V_{RHE} for the catalysts. (Reprinted with permission from [57]. Copyright 2015 American Chemical Society.)

As shown by DFT calculations and experimental measurements, Pt(111) is more active than Pt(100) toward ORR. While the small Pt particles in the Pt/C catalyst were likely enclosed by a mix of {100}, {111}, and {211} facets, the Pd@Pt_{nL} octahedra were mainly enclosed by {111} facets in addition to the minor presence of {100} facets at the

corner sites. As indicated by DFT calculations, the Pd core could weaken the binding of OH on the surface of the catalyst by modulating the electronic structure of the Pt shell, leading to acceleration of the ORR kinetics. The mass activities of the Pd@Pt_{2-3L}/C, Pd@Pt_{3-4L}/C, and Pd@Pt_{4-5L}/C based upon the mass of Pt were 0.48, 0.40, and 0.34 A mg_{Pt}^{-1}, respectively, which were 5.4, 4.5, and 3.8 times higher than that of the Pt/C catalyst (Table 2.5). The significant improvement in mass activity for the Pd@Pt_{nL}/C catalysts could be attributed to the enhancement in both specific ORR activity and dispersion of Pt atoms. While the mass activities of the Pd@Pt_{nL}/C in terms of Pt decreased with increasing number (n) of Pt overlayers, the mass activities in terms of precious metals (*i.e.*, both Pt and Pd) did not change significantly (Figure 2.11F).

Table 2.5. Comparison of the specific ECSA, specific activity (SA), and mass activity (MA) for the ORR catalysts based upon Pt/C and Pd@Pt_{nL}/C.

Catalyst	Specific ECSA ($m^2\ g_{Pt}^{-1}$)	SA at 0.9 V_{RHE} (mA cm_{Pt}^{-2})	MA at 0.9 V_{RHE} (A mg_{Pt}^{-1})	Synthesis method
Pt/C	51.0	0.17	0.089	-
Pd@Pt_{2-3L}/C	79.0	0.73	0.48	Polyol-based system
Pd@Pt_{3-4L}/C	60.8	0.67	0.40	
Pd@Pt_{4-5L}/C	43.4	0.78	0.34	
Pd@Pt_{2-3L}/C	53.6	0.91	0.49	Water-based system

Reprinted with permission from [57]. Copyright 2015 American Chemical Society.

Synthesis of Pd@Pt_{nL} Octahedra Using the Water-Based Protocol. For the water-based synthesis, I focused only on Pd@$Pt_{2–3L}$ octahedra because they were anticipated to exhibit the highest mass activity toward ORR among all the samples with n varying between 2 and 5. To establish the optimal protocol for the synthesis of Pd@$Pt_{2–3L}$ octahedra in a water-based system, I conducted a systematic study by changing the experimental parameters one by one from the standard procedure for the polyol-based protocol. Figure 2.12 shows a series of TEM images for the products obtained during the optimization of the protocol. First, I carried out the synthesis using the standard procedure for the polyol-based protocol except for the drop in reaction temperature from 200 ^{o}C to 95 ^{o}C (Figure 2.12A). I then conducted the reaction in water instead of EG at 95 ^{o}C (Figure 2.12B). For both samples, the particle surfaces were not as smooth as those for the Pd@$Pt_{2–3L}$ octahedra obtained using the standard procedure at 200 ^{o}C (Figure 2.12A). Due to the reduction in temperature, the Pt adatoms deposited on the Pd octahedra could not readily diffuse across the entire surface to generate smooth overlayers. In addition, the Pt(IV) precursor could not be completely reduced to Pt atoms due to the weakened reducing power of EG and AA at a low temperature, and thus the Pt content in the product dropped from 29.1 wt% (Figure 2.6A) to 13.0 wt% (Figure 2.12A) and 10.7 wt% (Figure 2.12B).

To deposit more Pt atoms on the seeds, I added more Pt(IV) precursor (from 2.1 to 31.3 μmol of Na_2PtCl_6) into the reaction solution (Figure 2.12C). In this case, self-nucleated Pt particles were found to coexist with the core−shell octahedra, and the Pt content remained at a low level of 11.5 wt %. This result implies that small Pt particles were formed through self-nucleation due to the increase in concentration for the newly formed Pt atoms in the reaction solution, thought most of these small Pt particles were lost during centrifugation and washing. To avoid self-nucleation, I switched to a mild reducing agent such as CA in an effort to maintain the Pt atoms at a sufficiently low concentration in the reaction solution (Figure 2.12D) [10, 34, 35]. Using this protocol, I

obtained nanoparticles with a hollow structure, which is believed to result from the galvanic replacement reaction between $PtCl_6^{2-}$ and Pd octahedral seeds. To prevent the galvanic replacement reaction, I switched the precursor from $PtCl_6^{2-}$ to $PtCl_4^{2-}$. However, the product still suffered from Pd hollowing (Figure 2.12E). It has been reported that the galvanic replacement reaction between $PtCl_4^{2-}$ and Pd could be accelerated in the presence of Br^- ions in the reaction solution [10, 36]. When I removed KBr from the reaction solution, I successfully obtained solid nanocrystals with smooth surfaces (Figure 2.12F). I then added the precursor solution rapidly in one shot in lieu of injecting dropwise (Figure 2.13A). If I can introduce the precursor solution in one shot to synthesize the Pd@Pt_{nL} octahedra, the protocol can be easily extended to the continuous droplet reactor for large-scale production [31].

Figure 2.13A shows a TEM image of the Pd@$Pt_{2–3L}$ octahedra, representing the uniform deposition of Pt on the Pd seeds as evidenced by their smooth surfaces. Although I rapidly added the K_2PtCl_4 solution into the reaction solution in one shot, I could obtain only the Pd@$Pt_{2–3L}$ octahedra without small Pt nanoparticles. This shows that the use of a mild reducing agent, CA, could result in a very low concentration of the free Pt atoms in the reaction solution, suppressing the self-nucleation. In particular, different from the Pd@Pt_{nL} octahedra from the polyol-based system, the product particles possess sharp corners. This indicates that the decreased reaction temperature in the water-based protocol slowed down the diffusion of the Pt adatoms from the corners to side faces. The HAADF-STEM images in Figure 2.13, B−E, clearly reveal the formation of a conformal shell of Pt epitaxially grown on the Pd(111) surface. The Pt atoms were evenly deposited on all the side faces of a Pd octahedron, with an average Pt shell thickness of 2−3 atomic layers. The average number of Pt layers was further confirmed as 2−3 by calculating the Pt and Pd contents obtained from ICP-MS analysis (Table 2.4). An EDX line scan in Figure 2.13F indicates that the Pt shell was formed on the surface of the Pd core with a thickness around 0.6 nm, which corresponds to the STEM images.

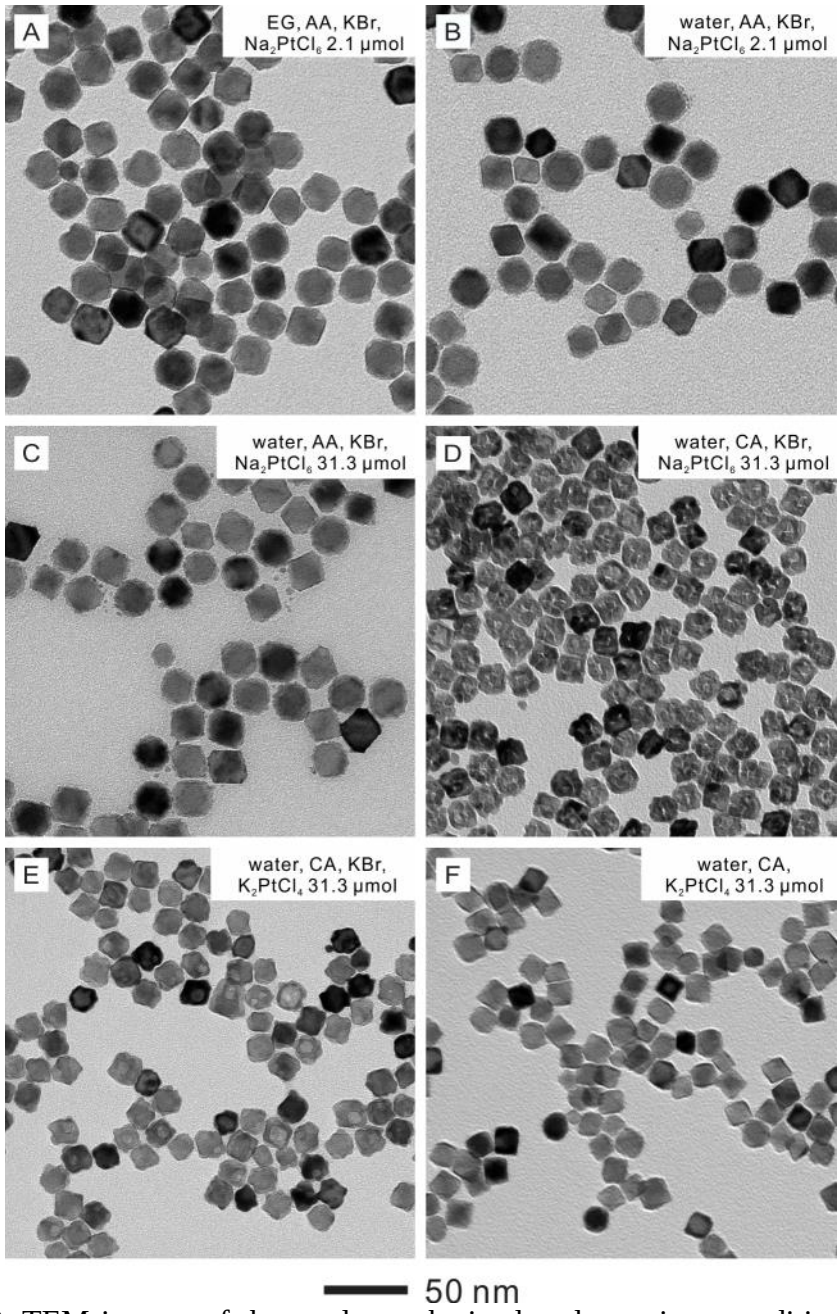

Figure 2.12. TEM images of the products obtained under various conditions where the experimental parameters were changed one by one from the standard protocol for the polyol-based system to the water-based system: (A) the standard procedure for the polyol-based synthesis of Pd@$Pt_{2–3L}$ octahedra except for the reduction of temperature from 200 ^{o}C to 95 ^{o}C; (B) the procedure used for the synthesis in (A) except for the use of water as a solvent; (C) the procedure for the synthesis in (B) except for the increase of Na_2PtCl_6 to 31.3 μmol; (D) the procedure for the synthesis in (C) except for the change of reducing agent from AA to CA; (E) the procedure for the synthesis in (D) except for the use of K_2PtCl_4 for a precursor; and (F) the procedure for the synthesis in (E) except for the absence of KBr. (Reprinted with permission from [57]. Copyright 2015 American Chemical Society.)

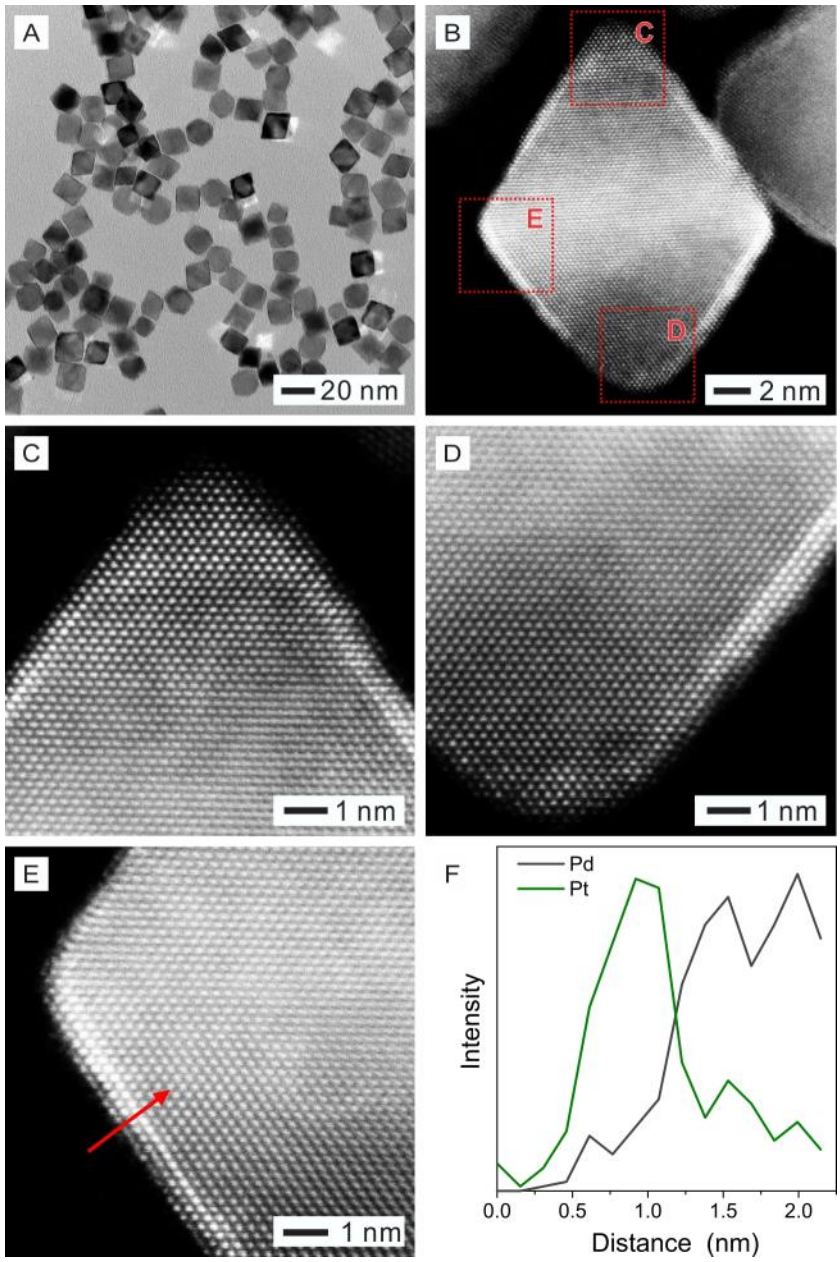

Figure 2.13. (A) TEM and (B−E) HAADF-STEM images of the Pd@$Pt_{2–3L}$ octahedra synthesized using the standard protocol based upon water. In the STEM images, the dark and bright regions correspond to Pd and Pt, respectively. (F) EDX line scan profiles of Pd and Pt for the Pd@$Pt_{2–3L}$ octahedron along the red arrow marked in (E). (Reprinted with permission from [57]. Copyright 2015 American Chemical Society.)

To understand the possible impact of solvent on the synthesis of Pd@$Pt_{2–3L}$ octahedra, I have also conducted additional syntheses by employing the standard procedure for the water-based protocol, except for the use of EG or DEG as a solvent. As

shown in Figure 2.14, small Pt nanoparticles were formed due to self-nucleation. Different from water, this result indicates that both EG and DEG have reducing power toward K_2PtCl_4. To eliminate self-nucleation, the precursor has to be used at a lower concentration (Figure 2.12) and introduced dropwise if EG or DEG is used as the solvent. As such, it is difficult to directly compare the products prepared using different solvents because experimental conditions other than the solvent also need to be altered in order to avoid self-nucleation.

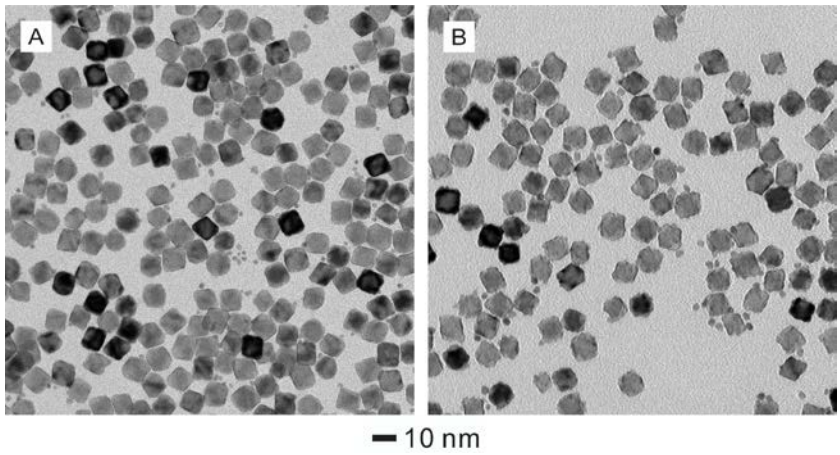

Figure 2.14. TEM images of the products prepared using the same standard procedure (water-based) as for the synthesis of Pd@$Pt_{2–3L}$ octahedra, except for the use of (A) EG and (B) DEG as the solvents, respectively. (Reprinted with permission from [57]. Copyright 2015 American Chemical Society.)

Electrocatalytic Measurements of the Pd@$Pt_{2–3L}$ Octahedra Synthesized in Water. I also measured the electrocatalytic properties of the Pd@$Pt_{2–3L}$ octahedra obtained using the water-based protocol. After obtaining the CV (Figure 2.15A), I estimated the ECSA of the Pd@$Pt_{2–3L}$/C catalyst, and the value was found to be slightly higher than that of the Pt/C (Table 2.5). However, the value was not as high as that of the Pd@$Pt_{2–3L}$/C prepared using the polyol-based protocol, which could be attributed to the increased amount of Pt atoms at the corner sites when the synthesis was conducted in

water at a much lower temperature. From the polarization curve in Figure 2.15B, I calculated the kinetic current density (j_k) for ORR using the Koutecky−Levich equation and then normalized it to the ECSA and Pt mass to obtain the specific activity ($j_{k,specific}$) and mass activity ($j_{k,mass}$), respectively (Figure 2.15, C and D). The specific and mass activities at 0.9 V_{RHE} based upon the Pt mass are plotted in Figure 2.15, E and F, showing that the Pd@Pt_{2-3L}/C exhibited 5-fold enhancement relative to the commercial Pt/C, for both the specific and mass activities (Table 2.5). Interestingly, the specific activity of the Pd@Pt_{2-3L}/C catalyst prepared in a water-based system was higher compared to that of its counterpart obtained from the polyol-based system (0.91 *vs* 0.73 mA cm_{Pt}^{-2}). This difference can be attributed to the fact that the nanocrystals synthesized in water were enclosed by well-defined {111} surfaces, while those obtained in polyol were enclosed by a mix of {111} and {100} facets due to truncation at the corner sites.

Evaluation of the Catalytic Durability of Pd@Pt_{2-3L} Octahedra toward ORR. In addition to the assessment of catalytic activity, I carried out an accelerated durability test to evaluate the long-term stability of the Pd@Pt_{2-3L}/C catalyst by benchmarking against the commercial P/C. For the test, I prepared another batch of the Pd@Pt_{2-3L} octahedra (Figure 2.16) using the standard, water-based protocol except for the use of 19-nm Pd octahedra as seeds. After the synthesis, the Pd@Pt_{2-3L} octahedra were dispersed on a carbon black (Vulcan XC-72, Cabot). In this case, I employed the same carbon black as the one used for the commercial Pt/C catalyst (Premetek) to minimize the impact of support on the catalytic performance. Figure 2.17, A and B, shows CVs and ORR polarization curves of the Pd@Pt_{2-3L}/C catalyst, respectively. To evaluate the long-term stability of the catalyst, I took measurements before and after applying 5,000, 10,000, 15,000, and 20,000 cycles of linear potential sweeps between 0.6 and 1.1 V_{RHE} in an O_2-saturated aqueous $HClO_4$ solution (0.1 M). Different from the measurements of ORR activities in the previous section, all ORR polarization curves in the durability test were corrected for *iR*-contribution in the RDE measurement system.

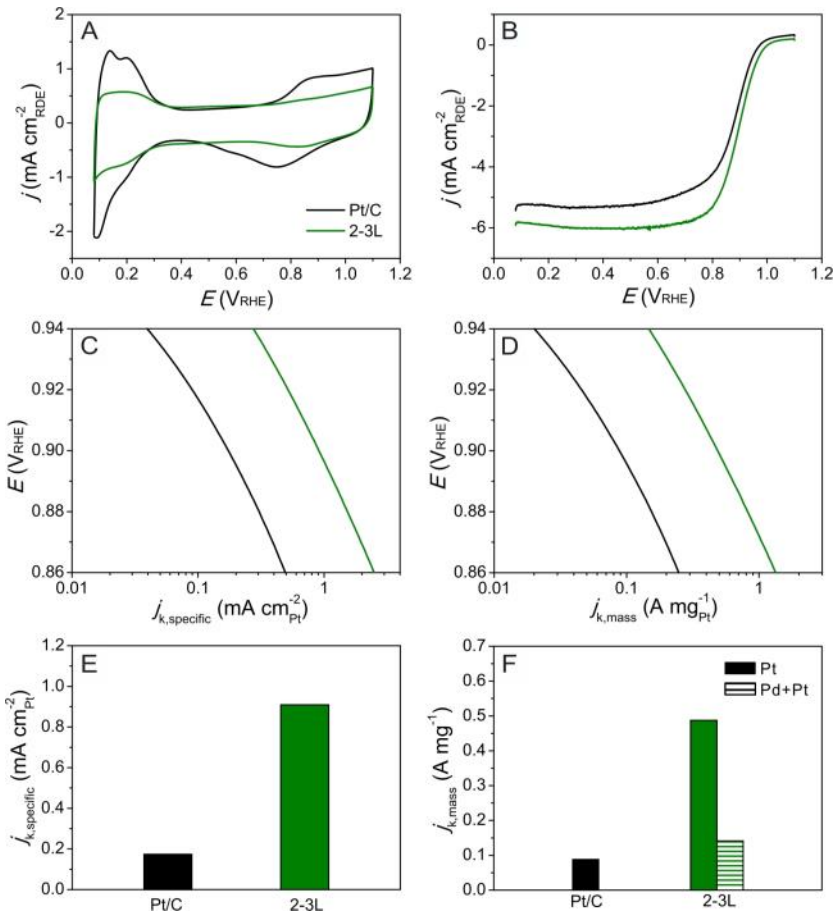

Figure 2.15. (A) CVs and (B) ORR polarization curves for the Pd@$Pt_{2–3L}$/C and commercial Pt/C catalysts. The Pd@$Pt_{2–3L}$ octahedra were synthesized using the standard, water-based protocol. The current densities (*j*) were normalized against the geometric area of the RDE (0.196 cm^2). (C) Specific and (D) mass activities given as kinetic current densities (j_k) normalized against the ECSA of the catalyst and the mass of Pt, respectively. (E) Specific and (F) mass activities (normalized against the masses of Pt and Pd+Pt, respectively) at 0.9 V_{RHE} for the catalysts. (Reprinted with permission from [57]. Copyright 2015 American Chemical Society.)

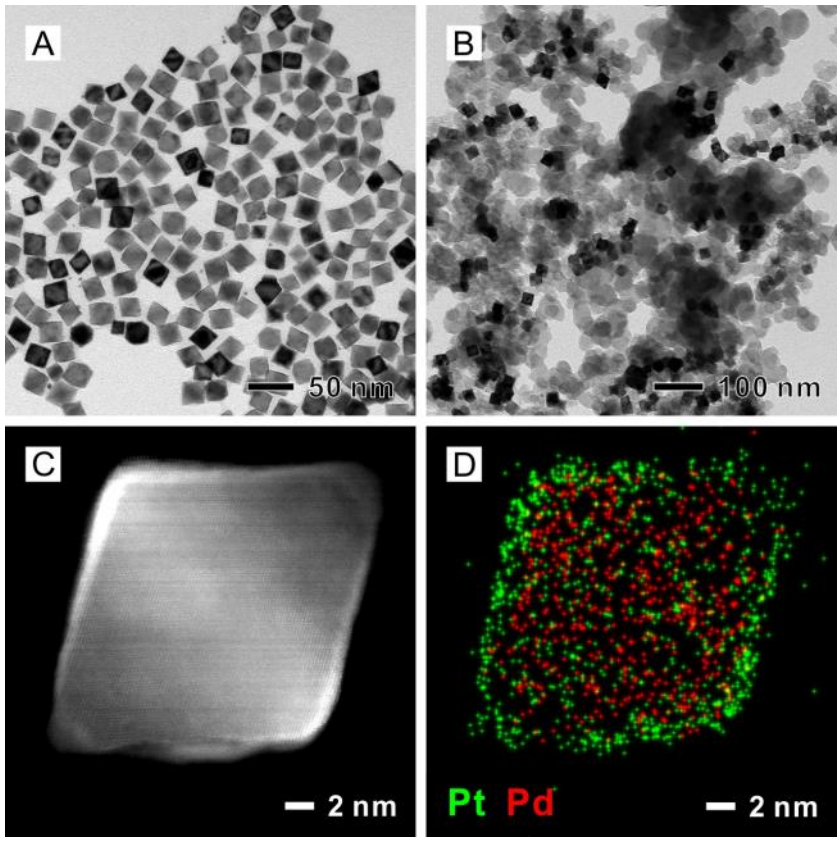

Figure 2.16. TEM images of (A) the as-obtained and (B) the carbon-supported Pd@$Pt_{2–3L}$ octahedra (Pd@$Pt_{2–3L}$/C) for the accelerated durability test. (C) HAADF-STEM image and (D) EDX elemental mapping of a Pd@$Pt_{2–3L}$ octahedron. In the EDX mapping, green and red colors correspond to Pt and Pd, respectively.

As shown in Figure 2.17E, the initial mass activity (at 0.9 V_{RHE}) of the Pd@$Pt_{2–3L}$/C was 1.25 A mg_{Pt}^{-1} and it gradually increased up to 1.40 A mg_{Pt}^{-1} after 10,000 cycles. However, it fell to 0.82 A mg_{Pt}^{-1} after 20,000 c ycles. To understand this trend in the observed mass activity, I also investigated the specific activity and the specific ECSA of the catalyst with repeating potential cycles. During the first 10,000 cycles, the specific activity (at 0.9 V_{RHE}) was maintained at around 1.6 mA cm_{Pt}^{-2}. However, it decreased to 0.89 mA cm_{Pt}^{-2} after 10,000 more cycles (Figure 2.17D). On the other hand, the specific ECSA of the Pd@$Pt_{2–3L}$/C steadily increased from 72 to 93 m^2 g_{Pt}^{-1} as I repeated up to 20,000 cycles (Figure 2.17C).

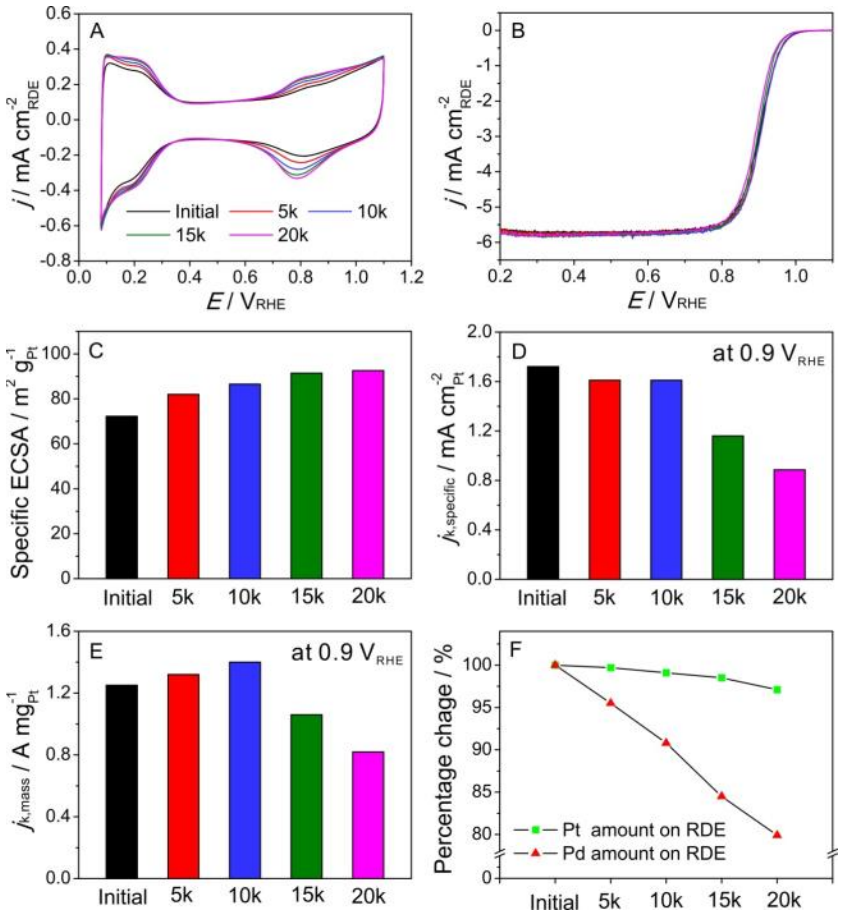

Figure 2.17. Electrocatalytic properties of the Pd@Pt_{2-3L}/C catalyst after repeating different number of potential cycles during an accelerated durability test: (A) CVs, (B) ORR polarization curves, (C) specific ECSAs, (D) specific activities, and (E) mass activities. All polarization curves were corrected for *iR*-contribution in the RDE measurement system. (F) Normalized Pt (green squares) and Pd (red triangles) contents in the catalyst remaining on the electrode during the durability test.

The observed changes to the specific activity and specific ECSA imply that the physicochemical properties (morphology, composition, and structure) of the catalyst are altered in the course of repeated potential cycles. To confirm the compositional changes, I first measured the Pt and Pd contents in the electrolyte after every 5,000 cycles using ICP-MS. Based on the results, I estimated the amounts of both metals remaining in the catalyst and plotted the results in Figure 2.17F. After 20,000 potential cycles, I did not

measure any significant loss of Pt content from the catalyst, however the Pd content dropped by ~20%. This substantial loss of Pd from the pristine catalyst can be attributed to the selective dissolution of Pd cores from the Pd@$Pt_{2–3L}$ octahedra due to sweeping electric potentials in a highly corrosive environment.

I also observed morphological changes to the Pd@$Pt_{2–3L}$/C by sampling and imaging the catalyst after every 5,000 cycles. The TEM images in Figure 2.18 indicate that the overall size and shape of the Pd@$Pt_{2–3L}$ octahedra were retained while repeating the potential cycles. Furthermore, no noticeable aggregation was observed among the catalytic nanoparticles. However, at 10,000 cycles, I started to observe some hollow octahedra in the sample. The population of hollow nanoparticles increased with the number of potential cycles. To better understand the transformation of Pd@$Pt_{2–3L}$ octahedra into hollow structures, I used STEM imaging and EDX elemental mapping to analyze the catalyst after 10,000 and 20,000 potential cycles, respectively. As shown in Figure 2.19, A and C, at 10,000 cycles I could clearly observe a Pd@$Pt_{2–3L}$ core−shell octahedron starting to evolve into a hollow structure from both upper and lower corner sites. Small holes were observed on the Pt surface around the upper and lower corners, which can be considered as channels for the dissolution of Pd from the core. Figure 2.19, B and D, clearly shows a Pt octahedral nanocage formed after complete dissolution of the Pd core from a Pd@$Pt_{2–3L}$ octahedron after 20,000 cycles. Although the holes in the Pt shell became enlarged relative to those in Figure 2.19, A and C, a thin Pt shell still remained even after the removal of Pd core.

The selective dissolution of the Pd cores from the Pd@$Pt_{2–3L}$ octahedra can be attributed to the higher reduction potential (E^0) of Pt than that of Pd (1.2 V *vs* 0.9 V at 25 ^oC) [37]. Thus, the Pd core could act as a sacrificial template, preferentially dissolving first and thereby preventing the Pt shell from being oxidized in the highly corrosive environment involved in the ORR test. Interestingly, even after removal of the Pd cores, the Pt shells still maintained their original octahedral shape and, thereby, their

catalytically active {111} facets. Based upon these results, it can be concluded that the Pd@Pt_{2-3L}/C catalyst could retain its initial specific activity without significant loss until 10,000 cycles. Reduction in the specific activity after 10,000 cycles can be attributed to the loss of {111} side faces due to the enlargement of holes. The increase in ECSA can be correlated to the structural transformation of the core−shell nanocrystals into nanocages when repeating the potential cycles. Once the Pd core has been removed, the catalytic particle could supply its interior surface to catalyze the ORR in addition to the exterior surface. As a combination of both the specific ECSA and specific activity, the mass activity of the Pd@Pt_{2-3L}/C increased until 10,000 cycles and decreased thereafter. Overall, the Pd@Pt_{2-3L}/C catalyst only lost 34% of its initial mass activity after 20,000 potential cycles.

To compare the catalytic durability of the Pd@Pt_{2-3L}/C catalyst with a commercial, state-of-the-art Pt/C catalyst, I conducted the accelerated durability test for the Pt/C using the same protocol (Figure 2.20). The initial mass activity of the Pt/C was 0.30 A mg_{Pt}^{-1}, which was around one-quarter of the value for the Pd@Pt_{2-3L}/C catalyst. In addition to its lower initial activity, the Pt/C exhibited significantly poorer durability than the Pd@Pt_{2-3L}/C. The Pt/C catalyst lost more than 60% of the initial mass activity after 15,000 potential cycles. This substantial reduction in mass activity for the Pt/C arose mainly from its decreasing specific ECSA during the repeated potential cycles. Contrary to the Pd@Pt_{2-3L}/C, the specific ECSA of Pt/C gradually decreased from 57 to 30 m^2 g_{Pt}^{-1} when repeating potential cycles (Figure 2.20C). The reduced ECSA of the Pt/C catalyst can be attributed to several causes: *i*) dissolution of Pt atoms from the Pt nanoparticles; *ii*) detachment of Pt nanoparticles from the carbon support; and *iii*) aggregation of the Pt nanoparticles [38, 39]. To quantitatively analyze the dissolution of Pt atoms and detachment of Pt nanoparticles during the repeated cycles of electric potential, I analyzed the Pt content in the electrolyte after every 5,000 cycles. As shown in Figure 2.20F, around 15% of the Pt was removed from the catalyst after 20,000

potential cycles. It is worth noting that the reduction of ECSA was even more significant, dropping by ~45% during the repeated cycling, suggesting that the aggregation of Pt nanoparticles also heavily impacts on the decrease of ECSA.

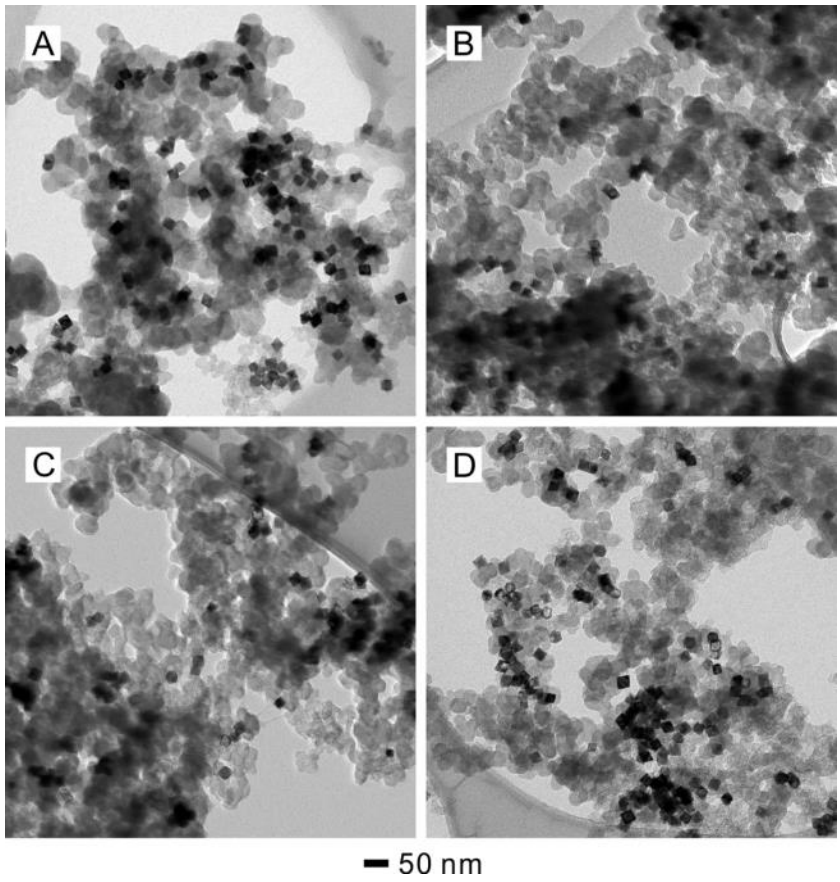

Figure 2.18. TEM images of the Pd@Pt_{2-3L}/C catalyst after (A) 5,000, (B) 10,000, (C) 15,000, and (D) 20,000 potential cycles, respectively, during the accelerated durability test.

To confirm the aggregation of the Pt nanoparticles in the Pt/C, I sampled catalyst from the electrode after the ORR tests for TEM imaging analysis. Figure 2.21 and Figure 2.9, A and B clearly show that the initial small spherical Pt nanoparticles were transformed into larger particles with irregular shapes, leading to further reduction in ECSA for the Pt/C. Recently, Toyota Motor Corporation and Japan Fine Ceramics Center have reported

that they directly observed the migration and then aggregation of Pt nanoparticles on a carbon support using an *in-situ* TEM technique, while under an electric potential loaded on an electrode [40]. It is also possible that the contact area between a nanoparticle and the carbon support may be critical to the migration of Pt nanoparticles. Note that the much smaller contact area between a Pt nanoparticle and the carbon support in the Pt/C catalyst, relative to the case of Pd@Pt_{2-3L}/C catalyst, could accelerate the migration, resulting in more significant aggregation.

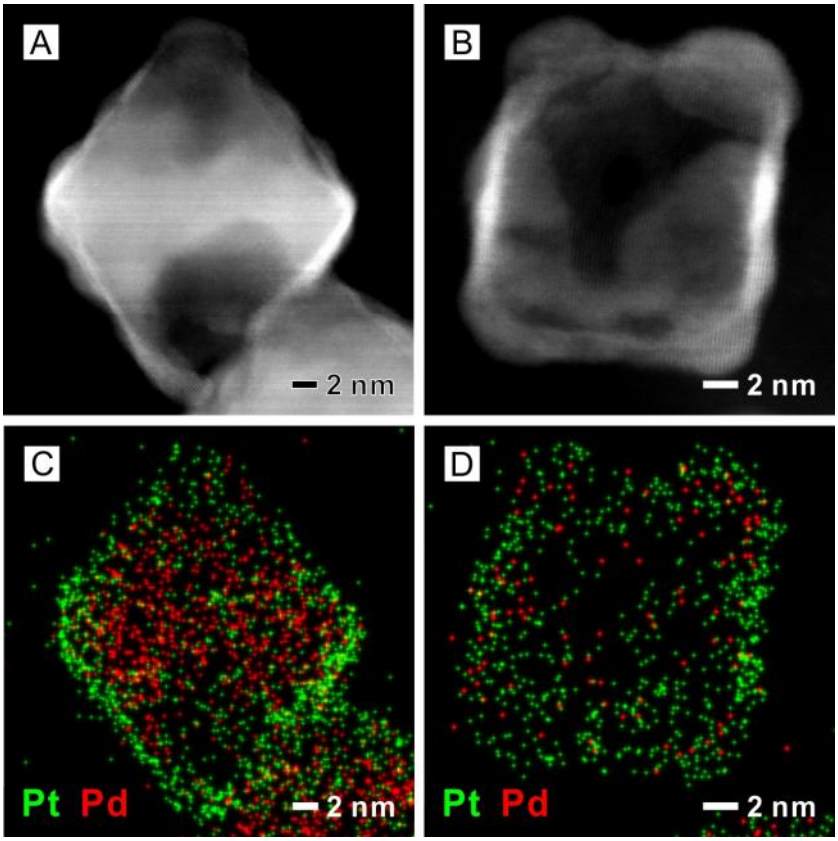

Figure 2.19. (A and B) HAADF-STEM images and (C and D) EDX elemental mappings recorded from a Pd@Pt_{2-3L} octahedron after (A and C) 10,000 and (B and D) 20,000 potential cycles. In the EDX mappings, the green and red colors correspond to Pt and Pd, respectively.

The morphological transformation, confirmed by TEM images in Figure 2.21, can also provide information regarding changes in specific activity for the Pt/C during the repeated cycles of electric potential. After 5,000 potential cycles (Figure 2.21A), the Pt nanoparticles became enlarged relative to the pristine ones before ORR (Figure 2.9, A and B), but the shape did not show noticeable transformation. The ORR specific activity has been reported to increase with an increased size for the Pt nanoparticles in the commercial Pt/C. It is primarily attributed to the fact that the increased size leads to a decreased proportion of low-coordinated surface atoms at edge and corner sites, which are less effective in catalyzing the ORR relative to atoms on the terrace [9, 41, 42]. I observed a similar slight enhancement in specific activity for the Pt/C after 5,000 cycles, consistent with the prior report (Figure 2.20D). However, the specific activity then gradually decreased with further cycling electric potential. This is likely caused by sharp transformation in shape for the Pt nanoparticles, generating many kinks and steps at the junctions between aggregated particles, which are generally not preferred for ORR due to their strong interaction with OH* [43].

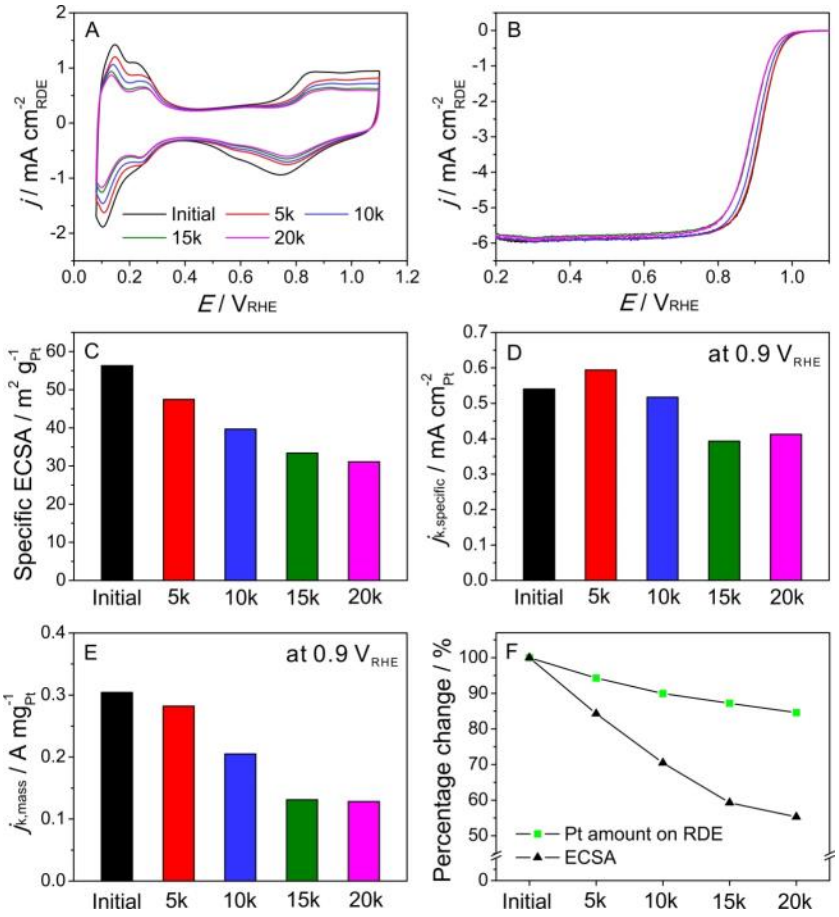

Figure 2.20. Electrocatalytic properties of the Pt/C catalyst after repeating different number of potential cycles during an accelerated durability test: (A) CVs, (B) ORR polarization curves, (C) specific ECSAs, (D) specific activities, and (E) mass activities. (F) Normalized Pt (green squares) and Pd (black triangles) contents in the catalyst remaining on the electrode during the durability test.

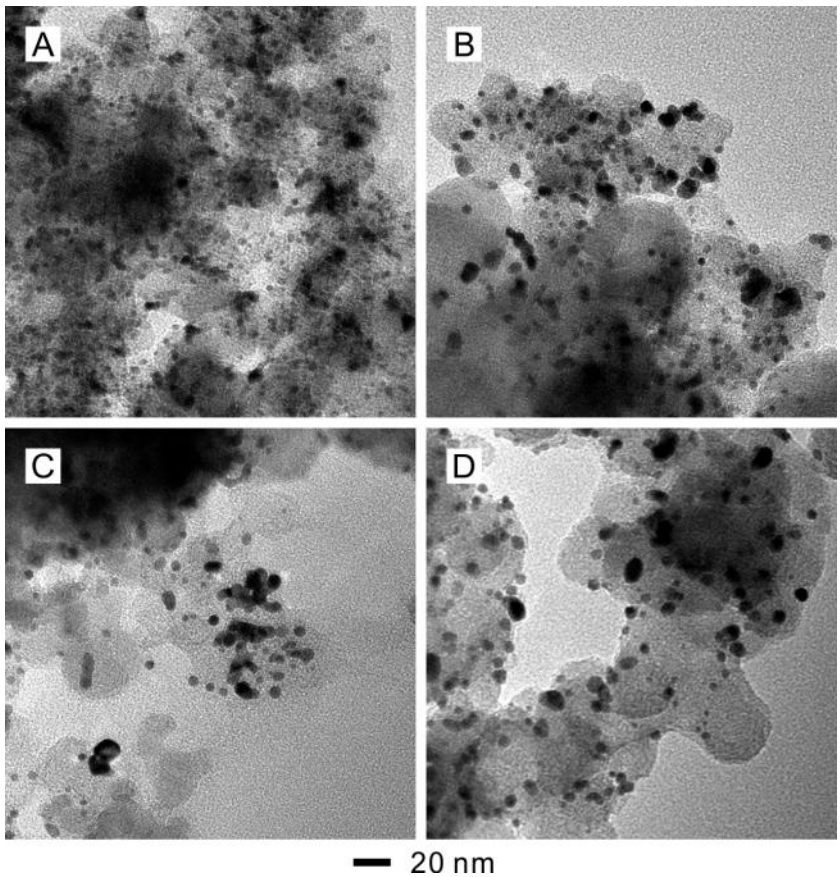

Figure 2.21. TEM images of the commercial Pt/C catalyst after (A) 5,000, (B) 10,000, (C) 15,000, and (D) 20,000 potential cycles, respectively, during an accelerated durability test.

2.3 Summary

In this chapter, I have demonstrated the syntheses of Pd@Pt_{nL} (n = 2−5) core−shell octahedra through the conformal, epitaxial deposition of Pt on Pd octahedral seeds using two different protocols based upon polyol and water, respectively. For the polyol-based system, the slow injection of a Pt(IV) precursor, the accelerated surface diffusion of Pt adatoms at a relatively high temperature, and the small mismatch in lattice constants between Pd and Pt all played important roles in enabling the layer-by-layer overgrowth. Significantly, the number (n) of Pt atomic layers could be tuned from two to five by

simply introducing more precursor into the growth solution. Significantly, I was able to extend the concept of atomic layer-by-layer deposition from a polyol- to a water-based system and, at the same time, significantly reduce the reaction temperature from 200 ^{o}C to 95 ^{o}C. Furthermore, I could introduce all the precursor in one shot by slowing down the reduction of a Pt(II) compound with the use of a mild reducing agent. All of the Pd@Pt_{nL} octahedra exhibited at least 4-fold enhancement in specific activity toward ORR when compared to a commercial Pt/C based upon 3.2-nm Pt particles. The DFT calculations suggested that this enhancement could be attributed to the destabilization of OH on the surfaces of the Pd@Pt_{nL} octahedra with respect to the Pt/C. This destabilization facilitates OH hydrogenation, the rate-limiting step for ORR on these materials. As a result of the enhancement in specific activity and the increase in dispersion for the Pt atoms, the Pd@Pt_{nL} octahedra also showed significant enhancement in mass activity when compared to the commercial Pt/C. Due to both the involvement of enlarged large particles and the presence of the sacrificial template (Pd cores), the catalysts based upon Pd@Pt_{nL} octahedra exhibited remarkably improved durability, making them a potential replacement for the current commercial ORR catalyst based upon Pt/C.

2.4 Experimental Section

Materials. All the chemicals were used as received from Sigma-Aldrich (unless specified). These include sodium tetrachloropalladate(II) (Na_2PdCl_4, 98%), sodium hexachloroplatinate(IV) hexahydrate ($Na_2PtCl_6 \cdot 6H_2O$, 98%), potassium tetrachloroplatinate(II) (K_2PtCl_4, 99.99%), poly(vinylpyrrolidone) (PVP, MW ≈ 55 000), formaldehyde (Fisher Scientific), ascorbic acid (AA, 99%), citric acid (CA, 99.5%), potassium bromide (KBr, 99%), ethylene glycol (EG, 99%, J. T. Baker), and ethanol (200 proof, KOPTEC). All aqueous solutions were prepared using deionized (DI) water with a resistivity of 18.2 MΩ cm.

Synthesis of Pd Cubes and Octahedra. The Pd nanocubes (6 and 10 nm in edge length) [44] and Pd octahedra (15 and 19 nm in edge length) [45] were synthesized, respectively, using protocols recently reported by the Xia group. For the synthesis of Pd octahedra, a suspension of the Pd cubes (0.3 mL, 2.0 mg mL^{-1}) and formaldehyde (0.1 mL) were added into an aqueous solution (8 mL) containing PVP (105 mg), and the mixture was heated at 60 ^{o}C for 10 min under magnetic stirring. An aqueous solution (3 mL) containing Na_2PdCl_4 (29 mg) was then quickly added into the preheated solution. The reaction solution was kept at 60 ^{o}C for 3 h under magnetic stirring. The reaction solution was cooled to room temperature. The product was collected by centrifugation, washed twice with DI water, and redispersed in EG (2 mL) or DI water (10 mL). The Pd octahedra of 15 and 19 nm in edge length were synthesized from the Pd cubes of 6 and 10 nm in edge length, respectively.

Synthesis of Pd@Pt_{nL} Octahedra in the Polyol-Based System. For the synthesis of Pd@Pt_{nL} octahedra in polyol, 1 mL of the Pd octahedra suspension (19 nm in edge length, 0.83 mg mL^{-1}), 67 mg of PVP, 100 mg of AA, 54 mg of KBr, and 12 mL of EG were mixed in a three-neck flask and heated at 110 ^{o}C for 1 h under magnetic stirring. The temperature was then quickly ramped to 200 ^{o}C within 20 min, and a specific amount of EG solution containing $Na_2PtCl_6 \cdot 6H_2O$ (0.1 mg mL^{-1}) was added dropwise with a syringe pump at a rate of 4.0 mL h^{-1}. After complete injection, the reaction solution was kept at 200 ^{o}C for 1 h under magnetic stirring and then cooled to room temperature. The product was collected by centrifugation, washed twice with ethanol and three times with DI water, and redispersed in DI water.

Synthesis of Pd@$Pt_{2–3L}$ Octahedra in the Water-Based System. For the typical synthesis of Pd@$Pt_{2–3L}$ octahedra in water, 35 mg of PVP and 60 mg of CA were added into 10 mL of the aqueous suspension of Pd octahedra (15 nm, 0.19 mg mL^{-1}) and then heated at 95 ^{o}C for 10 min under magnetic stirring. Meanwhile, 13 mg of K_2PtCl_4 was dissolved in 3 mL of DI water, and the solution was quickly added into the preheated

solution using a pipet. The reaction solution was kept at 95 ^{o}C for 24 h under magnetic stirring and then cooled to room temperature. The product was collected by centrifugation, washed three times with DI water, and redispersed in DI water. I also prepared another batch of Pd@$Pt_{2–3L}$ octahedra using the same protocol except for the use of the 19-nm Pd octahedra as the seeds.

Preparation of Carbon-Supported Pd@Pt_{nL} Octahedra Catalysts (Pd@Pt_{nL}/C). The Pd@Pt_{nL} octahedra were collected by centrifugation and redispersed in 20 mL of ethanol. A specific amount of carbon black (Ketjenblack EC-300J, AkzoNobel) was added into the suspension to obtain a loading of about 20 wt % for both Pt and Pd. It is worth noting that I employed a different carbon black (Vulcan XC-72, Cabot) to prepare the Pd@$Pt_{2–3L}$/C for the durability test. The mixture was then ultrasonicated for 3 h, and the resulting Pd@Pt_{nL}/C was collected by centrifugation, redispersed in 10 mL of acetic acid, and heated at 60 ^{o}C for 2 h to remove PVP or bromide on the surface of the particles. The Pd@Pt_{nL}/C catalyst was washed three times with ethanol and dried in an oven at 70 ^{o}C for 30 min prior to the use for ORR tests.

Morphological, Structural, and Elemental Characterizations. TEM was done with an HT-7700 microscope (Hitachi) operated at 120 kV. HAADF-STEM and EDX scanning analyses were performed using an ARM200F aberration-corrected STEM (JEOL) or an HD-2700 aberration-corrected STEM (Hitachi) both operated at 200 kV. ICP-MS (NexION 300Q, PerkinElmer) was used for a quantitative analysis of metal content in the samples.

Electrochemical Measurements. Electrochemical measurements were performed using a glassy carbon RDE (Pine Research Instrumentation) connected to a potentiostat (CHI 600E, CH Instruments). An ink for the electrochemical measurement was prepared by adding 3 mg of the Pd@Pt_{nL}/C into a mixture of DI water (1 mL), 2-propanol (1 mL, Sigma-Aldrich), and Nafion (5% solution, Sigma-Aldrich, 40 μL), followed by sonication for 10 min. A working electrode was prepared by loading the ink (20 μL) on the glassy

carbon electrode. Another working electrode was prepared from the carbon-supported Pt catalyst (Pt/C, 20 wt% 3.2-nm nanoparticles on Vulcan XC-72 carbon support, Premetek) using the same protocol. An Ag/AgCl electrode (BASi) or RHE (Gaskastel) was used as the reference electrode. A Pt mesh (or coil) was used as the counter electrode. The potentials (V_{RHE}) were converted to values with reference to the RHE if needed. The electrolyte was an aqueous $HClO_4$ solution (Baker or GFS chemicals) with a concentration of 0.1 M. The cyclic voltammograms were measured in a N_2-saturated electrolyte by cycling between 0.08 and 1.1 V_{RHE} at a sweep rate of 0.05 V s^{-1}. To calculate the ECSA, I measured the charges generated from both adsorption and/or desorption of hydrogen between 0.08 and 0.4 V_{RHE} with a reference value of 210 (Pt/C) or 240 μC cm^{-2} (octahedra) for underpotentially deposited hydrogen from a Pt surface. The ORR test was carried out in an O_2-saturated electrolyte with a scan rate of 0.01 V s^{-1} and a rotation speed of 1,600 rpm. The kinetic current density (j_k) was derived from the Koutecky−Levich equation as follows:

$$\frac{1}{j} = \frac{1}{j_k} + \frac{1}{j_d}$$

where j is the measured current density and j_d is the diffusion-limiting current density. For the accelerated durability tests, the CVs and ORR polarization curves were measured after sweeping 5,000, 10,000, 15,000, and 20,000 cycles between 0.6 and 1.1 V_{RHE} at a rate of 0.1 V s^{-1} in an O_2-saturated aqueous $HClO_4$ solution at room temperature.

2.5 DFT Calculations

Calculations were performed by the Mavrikakis group using plane wave DFT, as implemented in the Dacapo code [46, 47]. The exchange-correlation potential and energy were described self-consistently by the GGA-PW91 functional [48, 49]. The ionic cores

were described by ultrasoft Vanderbilt pseudopotentials [50]. Due to the relatively small differences in measured ORR activities, the surface Brillouin zone was sampled with a 10x10x1 Monkhorst-Pack k-point mesh [51], and the Kohn-Sham one-electron valence states were expanded on the basis of plane waves with a kinetic energy cutoff of 400 eV; these criteria are tighter than would typically be used for this type of calculation. Eighteen special Chadi-Cohen k-points [52] and a kinetic energy cutoff of 340 eV were used for calculations of diffusion activation energy barriers, which were determined using the CI-NEB method [53]. The vibrational frequencies of adsorbed intermediates were determined from the diagonalization of the mass-weighted Hessian matrix. A second order finite difference approach, using a step size of 0.015 Å, was used to numerically differentiate the forces [54]. The entropies and ZPE of surface species were calculated from the vibrational frequencies using the harmonic oscillator approximation. ZPE and entropic contributions to total energy for adsorption on Pt_{nL}*/Pd(111) surfaces were assumed to be the same as on Pt(111), due to the similar optimized geometries of each intermediate on those surfaces. All calculations were performed on slabs with seven metal layers, in which the top five layers were allowed to fully relax. The Pt_{nL}*/Pd(111) surfaces were modeled by replacing the top n layers by Pt atoms (n = 2−5). These slabs were constructed using the optimized bulk lattice constant of Pd (3.99 Å). A pure Pt(111) slab was also constructed using the optimized bulk lattice constant of Pt (4.00 Å). Both optimized lattice constants are in good agreement with the experimental values (3.89 Å and 3.92 Å for Pd and Pt, respectively) [55]. A 2x2 periodic surface unit cell was used, corresponding to a surface coverage of 0.25 ML of each adsorbate.

Surface Diffusion of Pt Adatoms. The Pd@Pt_{nL} octahedra could be synthesized at 95 ^{o}C, which is a considerably lower temperature than what was needed for the synthesis of Pd@Pt_{nL} nanocubes (200 ^{o}C) [20]. In general, a sufficiently high temperature is required to accelerate the diffusion of Pt adatoms across the Pd surface, thereby avoiding the formation of Pt islands on the surface. As a first investigation of this phenomenon,

Mavrikakis and coworkers calculated the diffusion barrier of Pt adatoms across a Pd(100) surface (as a model for the cubes) and a Pd(111) surface (as a model for the octahedra). My collaborator and I found that the diffusion of a Pt adatom across Pd(100) has a relatively large activation energy barrier (E_A) of 1.06 eV. In contrast, the diffusion of Pt across Pd(111) has a very small barrier of only 0.16 eV, which corresponds to a rate constant, k ($k \propto \exp\left(-\frac{E_A}{k_B T}\right)$, where k_B is the Boltzmann constant and T is absolute temperature), which is more than 15 orders of magnitude higher at room temperature. A fundamental reason for the difficulty of diffusion across the (100) facet is the stronger binding of adatoms due to its under coordination relative to the (111) facet. The Pt atoms bind to three-fold hollow sites on the Pd(111) surface, while they bind to four-fold hollow sites on the Pd(100) surface. The diffusion barrier of adsorbates across a metal surface has been shown to correlate with the binding energy of adsorbates [56]. In particular, the calculations indicate that Pt binds more strongly to the Pd(100) facet than the Pd(111) by 0.63 eV. These findings are therefore in agreement with this expectation, and support the experimental observations that higher temperatures are needed to facilitate energetically demanding diffusion on Pd cubic seeds.

ORR Activity of Surface Models. To understand the experimentally observed enhanced activity of the Pd@Pt_{nL} octahedra relative to Pt/C and the Pd@Pt_{nL} cubes, Mavrikakis and coworkers performed self-consistent periodic DFT calculations to determine the binding energies of adsorbed O and OH on model surfaces. The Pd@Pt_{nL} octahedra were modeled as Pt_{nL}*/Pd(111) extended surfaces (with the lattice constant of Pd), while Pt/C was modeled using Pt(111) and Pt(100) extended surfaces (with the lattice constant of Pt). In a previous work by Xia and coworkers [20], the Pd@Pt_{nL} cubes were modeled as Pt_{nL}*/Pd(100) extended surfaces (with nearly identical calculation parameters as in this study). The binding energies (*BE*s) of adsorbed species were calculated as $BE = E_{\text{total}} - E_{\text{clean slab}} - E_{\text{gas phase}}$, where E_{total} is the total energy of the

adsorbate on the slab, $E_{\text{clean slab}}$ is the total energy of the slab without the adsorbate, and E_{gas} phase is the total energy of the isolated adsorbate in the gas phase.

The free energy changes (ΔG) of elementary steps with proton/electron transfer were calculated as a function of electrode potential using the computational hydrogen electrode developed by Nørskov and coworkers [29]: $\Delta G = \Delta E + \Delta ZPE - T\Delta S + |e|U$, where ΔE is the change in total energy, ΔZPE is the zero-point-energy correction, T is the absolute temperature (298 K), ΔS is the change in entropy, $|e|$ is the absolute value of charge of an electron, and U is the electrode operating potential. The electrochemical reference was chosen to be the RHE, in which the reaction $H_2 \leftrightarrow 2\,(H^+ + e^-)$ is in equilibrium at a defined potential of 0 V under standard conditions. Therefore, the hydrogenation reactions considered in this study become more endothermic as U becomes more positive. When calculating free energies, adsorbed OH was stabilized by 0.5 eV on (111) surface and by 0.1 eV on (100) surface to account for interactions with the water bilayer [40]. The free energies of reaction were tabulated in Table 2.1. For all surfaces studied, OH hydrogenation is more difficult than O hydrogenation, and therefore is assumed to be the rate-limiting step.

As in a previous work by Xia and coworkers [20], a simple Sabatier analysis [29] was performed to understand the effect of OH binding on the ORR activity. Mavrikakis and coworker calculated the rate constant of OH hydrogenation (the rate-limiting step) with an Arrhenius formula. They set the activation energy of elementary reaction steps equal to the change in free energy of the reaction step, or zero, whichever value is larger. This provides a thermodynamic lower bound for the activation energy of elementary steps [30]. The rate constant of OH hydrogenation on surface i (k_i) was therefore calculated as $k_i = \exp(\frac{-\Delta G_i}{k_B T})$, where ΔG_i is the free energy change on surface i, k_B is the Boltzmann constant, and T is the absolute temperature (298 K). Mavrikakis group calculated the relative activity of each surface by normalizing the rate constants to $k_{Pt(111)}$; therefore, the

relative activities shown in Figure 2.2 of the main text were calculated as $k_i/k_{Pt(111)}$. It is particularly noteworthy that all of the Pt_{nL}*/Pd(111) (n = 2−5) surfaces exhibit weaker OH binding than pure Pt(111), suggesting that the Pd@Pt_{nL} octahedra would have higher specific activity than pure Pt octahedra.

2.6 Notes to Chapter 2

Part of this chapter is adapted from the paper "Atomic Layer-by-Layer Deposition of Platinum on Palladium Octahedra for Enhanced Catalysts toward the Oxygen Reduction Reaction" published in *ACS Nano* [57]. The DFT calculations in this chapter were performed by the Mavrikakis group at the University of Wisconsin-Madison.

2.7 References

[1] Tian, N.; Zhou, Z.-Y.; Sun, S.-G.; Ding, Y.; Wang, Z. L. *Science* **2007**, *316*, 732−735.

[2] Bratlie, K. M.; Lee, H.; Komvopoulos, K.; Yang, P.; Somorjai, G. A. *Nano Lett.* **2007**, *7*, 3097−3101.

[3] Wang, C.; Daimon, H.; Onodera, T.; Koda, T.; Sun, S. *Angew. Chem. Int. Ed.* **2008**, *47*, 3588−3591.

[4] Chen, C.; Kang, Y.; Huo, Z.; Zhu, Z.; Huang, W.; Xin, H. L.; Snyder, J. D.; Li, D.; Herron, J. A.; Mavrikakis, M.; Chi, M.; More, K. L.; Li, Y.; Marković, N. M.; Somorjai, G. A.; Yang, P.; Stamenkovic, V. R. *Science* **2014**, *343*, 1339−1343.

[5] Zhang, H.; Jin, M.; Xia, Y. *Chem. Soc. Rev.* **2012**, *41*, 8035−8049.

[6] Stamenkovic, V. R.; Mun, B. S.; Arenz, M.; Mayrhofer, K. J. J.; Lucas, C. A.; Wang, G.; Ross, P. N.; Marković, N. M. *Nat. Mater.* **2007**, *6*, 241−247.

[7] Choi, S.-I.; Xie, S.; Shao, M.; Odell, J. H.; Lu, N.; Peng, H.-C.; Protsailo, L.; Guerrero, S.; Park, J.; Xia, X.; Wang, J.; Kim, M. J.; Xia, Y. *Nano Lett.* **2013**, *13*,

3420−3425.

[8] Choi, S.-I.; Xie, S.; Shao, M.; Lu, N.; Guerrero, S.; Odell, J. H.; Park, J.; Wang, J.; Kim, M. J.; Xia, Y. *ChemSusChem* **2014**, *7*, 1476−1483.

[9] Lim, B.; Jiang, M.; Camargo, P. H. C.; Cho, E. C.; Tao, J.; Lu, X.; Zhu, Y.; Xia, Y. *Science* **2009**, *5*, 1302−1305.

[10] Zhang, H.; Jin, M.; Wang, J.; Kim, M. J.; Yang, D.; Xia, Y. *J. Am. Chem. Soc.* **2011**, *133*, 10422−10425.

[11] Zhang, J. L.; Vukmirovic, M. B.; Xu, Y.; Mavrikakis, M.; Adzic, R. R. *Angew. Chem. Int. Ed.* **2005**, *44*, 2132−2135.

[12] Vukmirovic, M. B.; Zhang, J.; Sasaki, K.; Nilekar, A. U.; Uribe, F.; Mavrikakis, M.; Adzic, R. R. *Electrochim. Acta* **2007**, *52*, 2257−2263.

[13] Liu, Y.; Gokcen, D.; Bertocci, U.; Moffat, T. P. *Science* **2012**, *338*, 1327−1330.

[14] Kitchin, J. R.; Nørskov, J. K.; Barteau, M. A.; Chen, J. G. *Phys. Rev. Lett.* **2004**, *93*, 156801-1−156801-4.

[15] Wang, J. X.; Inada, H.; Wu, L.; Zhu, Y.; Choi, Y.; Liu, P.; Zhou, W.-P.; Adzic, R. R. *J. Am. Chem. Soc.* **2009**, *131*, 17298−17302.

[16] Wang, X.; Orikasa, Y.; Takesue, Y.; Inoue, H.; Nakamura, M.; Minato, T.; Hoshi, N.; Uchimoto, Y. *J. Am. Chem. Soc.* **2013**, *135*, 5938−5941.

[17] Strasser, P.; Koh, S.; Anniyev, T.; Greeley, J.; More, K.; Yu, C.; Liu, Z.; Kaya, S.; Nordlund, D.; Ogasawara, H.; Toney, M. F.; Nilsson, A. *Nat. Chem.* **2010**, *2*, 454−460.

[18] Greeley, J.; Mavrikakis, M. *Nat. Mater.* **2004**, *3*, 810−815.

[19] Alayoglu, S.; Nilekar, A. U.; Mavrikakis, M.; Eichhorn, B. *Nat. Mater.* **2008**, *7*, 333−338.

[20] Xie, S.; Choi, S.-I.; Lu, N.; Roling, L. T.; Herron, J. A.; Zhang, L.; Park, J.; Wang, J.; Kim, M. J.; Xie, Z.; Mavrikakis, M.; Xia, Y. *Nano. Lett.* **2014**, *14*, 3570−3576.

[21] Stamenkovic, V. R.; Fowler, B.; Mun, M. S.; Wang, G. F.; Ross, P. N.; Lucas, C. A.;

Marković, N. M. *Science* **2007**, *315*, 493−497.

[22] Zhang, J.; Yang, H.; Fang, J.; Zou, S. *Nano Lett.* **2010**, *10*, 638−644.

[23] Zhou, W.; Wu, J.; Yang, H. *Nano Lett.* **2013**, *13*, 2870−2874.

[24] Adzic, R. R., Zhang, J.; Sasaki, K.; Vukmirovic, M. B.; Shao, M.; Wang, J. X.; Nilekar, A. U.; Mavrikakis, M.; Valerio, J. A.; Uribe, F. *Top. Catal.* **2007**, *46*, 249−262.

[25] Shao, M.; He, G.; Peles, A.; Odell, J. H.; Zeng, J.; Su, D.; Tao, J.; Yu, T.; Zhu, Y.; Xia, Y. *Chem. Commun.* **2013**, *49*, 9030−9032.

[26] Xia, X.; Xie, S.; Liu, M.; Peng, H.-C.; Lu, N.; Wang, J.; Kim, M. J.; Xia, Y. *P. Natl. Acad. Sci. U. S. A.* **2013**, *110*, 6669−6673.

[27] Xia, Y.; Xiong, Y.; Lim, B.; Skrabalak, S. E. *Angew. Chem. Int. Ed.* **2009**, *48*, 60−103.

[28] Lim, B.; Jiang, M.; Tao, J.; Camargo, P. H. C.; Zhu, Y.; Xia, Y. *Adv. Funct. Mater.* **2009**, *19*, 189−200.

[29] Nørskov, J. K.; Rossmeisl, J.; Logadottir, A.; Lindqvist, L. *J. Phys. Chem. B* **2004**, *108*, 17886−17892.

[30] Koper, M. T. M. *J. Electroanal. Chem.* **2011**, *660*, 254−260.

[31] Zhang, Lei; Xia, Y. *Adv. Mater.* **2014**, *26*, 2600–2606.

[32] Lim, B.; Kobayashi, H.; Camargo, P. H. C.; Allard, L. F.; Liu, J.; Xia, Y. *Nano Res.* **2010**, *3*, 180−188.

[33] Zhang, Z.; Lagally, M. G. *Science* **1997**, *276*, 377−383.

[34] Lim, B.; Wang, J.; Camargo, P. H. C.; Jiang, M.; Kim, M.; Xia, Y. *Nano Lett.* **2008**, *8*, 2535−2540.

[35] Jiang, M.; Lim, B.; Tao, J.; Camargo, P. H. C.; Ma, C.; Zhu, Y.; Xia, Y. *Nanoscale* **2010**, *2*, 2406−2411.

[36] Zhang, H.; Jin, M.; Wang, J.; Li, W.; Camargo, P. H. C.; Kim, M. J.; Yang, D.; Xie, Z.; Xia, Y. *J. Am. Chem. Soc.* **2011**, *133*, 6078−6089.

[37] Sasaki, K.; Naohara, H.; Cai, Y.; Choi, Y. M.; Liu, P.; Vukmirovic, M. B.; Wang, J. X.; Adzic, R. R. *Angew. Chem., Int. Ed.* **2010**, *49*, 8602−8607.

[38] Ferreira, P. J., la O', G. J.; Shao-Horn, Y.; Morgan, D.; Makharia, R.; Kocha, S.; Gasteiger, H. A. *J. Electrochem. Soc.* **2005**, *152*, A2256−A2271.

[39] Bruijn, F. A. de; Dam, V. A. T.; Janssen, G. J. M. *Fuel Cells* **2008**, *8*, 3−22.

[40] Toyota Motor Corporation. *R&D Breakthrough Sets Stage for More Efficient, Durable Fuel Cell Stacks*, http://newsroom.toyota.co.jp, 2015.

[41] Greeley, J.; Rossmeisl, J.; Hellmann, A.; Nørskov, J. K. *Z. Phys. Chem.* **2007**, *221*, 1209−1220.

[42] Xie, S.; Choi, S.-I.; Xia, X.; Xia, Y. *Curr. Opin. Chem. Eng.* **2013**, *2*, 142−150.

[43] Kuzume, A.; Herrero, E.; Feliu, J. M.; *J. Electroanal. Chem.* **2007**, *599*, 333−343.

[44] Jin, M.; Liu, H.; Zhang, H.; Xie, Z.; Liu, J.; Xia, Y. *Nano Res.* **2011**, *4*, 83−91.

[45] Jin, M.; Zhang, H.; Xie, Z.; Xia, Y. *Energy Environ. Sci.* **2012**, *5*, 6352−6357.

[46] Hammer, B.; Hansen, L. B.; Nørskov, J. K. *Phys. Rev. B* **1999**, *59*, 7413−7421.

[47] Greeley, J.; Nørskov, J. K.; Mavrikakis, M. **2002**, *53*, 319−348.

[48] Perdew, J. P.; Chevary, J. A.; Vosko, S. H.; Jackson, K. A.; Pederson, M. R.; Singh, D. J.; Fiolhais, C. *Phys. Rev. B* **1992**, *46*, 6671−6687.

[49] White, J. A.; Bird, D. M. *Phys. Rev. B* **1994**, *50*, 4954−4957.

[50] Vanderbilt, D. *Phys. Rev. B* **1990**, *41*, 7892−7895.

[51] Monkhorst, H. J.; Pack, J. D. *Phys. Rev. B* **1976**, *13*, 5188−5192.

[52] Chadi, D. J.; Cohen, M. L. *Phys. Rev. B* **1973**, *8*, 5747−5753.

[53] Henkelman, G.; Uberuaga, B. P.; Jonsson, H. A. *J. Chem. Phys.* **2000**, *113*, 9901−9904.

[54] Greeley, J.; Mavrikakis, M. *Surf. Sci.* **2003**, *540*, 215−229.

[55] Haynes W. M. *CRC Handbook of Chemistry and Physics*; 94th ed.; Taylor and Francis: Boca Raton, 2014.

[56] Nilekar, A. U.; Greeley, J.; Mavrikakis, M. *Angew. Chem. Int. Ed.* **2006**, *45*,

7046−7049.

[57] Park, J.; Zhang, L.; Choi, S.-I.; Roling, L. T.; Lu, N.; Herron, J. A.; Xie, S.; Wang, J.; Kim, M. J.; Mavrikakis, M.; Xia, Y. *ACS Nano* **2015**, *9*, 2635−2647.

CHAPTER 3

IMPROVING THE CATALYTIC DURABILITY OF PLATINUM−NICKEL OCTAHEDRA WITH ULTRATHIN, CONFORMAL SHELLS OF PLATINUM

3.1 Introduction

In order to make the technology based on PEMFC viable for large scale use, many strategies have been explored for maximizing the mass activity of Pt-based catalysts for toward ORR. In general, the activity of an ORR catalyst can be enhanced by engineering the nanoparticles involved, including their size [1, 2], shape [3, 4], surface structure [5−12], and elemental composition [13−18]. Among the advanced catalysts, those based on Pt−M (M=Ni, Co, and Fe) bimetallic octahedral nanocrystals have demonstrated remarkably high activities toward ORR [13−18]. Mixing Pt with another transition metal could alter the electronic structure of surface Pt atoms and thus optimize the binding energies of various oxygen species (*e.g.*, O and OH) involved in ORR [13]. In particular, Pt−Ni octahedral nanocrystals represent the most successful development in recent years, showing record-setting mass activity [14, 16, 18]. Although the activity of Pt−Ni octahedral nanocrystals have exceeded the value recommended by DOE, their poor durability arising from the dissolution of Ni still needs to be addressed before the catalysts can be applied to commercial use [14, 19]. In particular, the low pH, high oxygen content, and highly positive cathode potential will result in a highly corrosive environment during the operation of a PEMFC, readily oxidizing and then dissolving Ni atoms from the surface of Pt−Ni nanocrystals. The dissolution of Ni will not only compromise the ORR activity by degrading the optimized Pt−O (or Pt−OH) interaction but also lead to deterioration of the device as a result of contamination to the membrane or ionomer by the released Ni ions [20].

Passivating the surface of Pt−Ni octahedral nanocrystals with ultrathin Pt shells offers an attractive strategy for addressing this issue. Deposition of a uniform, ultrathin shell of Pt on the surface of a Pt−Ni octahedron is anticipated to effectively protect the Ni atoms in the subsurface from oxidation and dissolution. In a recent publication, Yang, Stamenkovic, and their coworkers reported that Pt_3Ni nanoframes with an ultrathin skin of Pt on the surface exhibited remarkable durability for ORR [8]. Sun and coworkers also observed significant improvement for both the ORR activity and durability of Fe−Ni−Pt alloy nanowires in the presence of Pt skins [21]. In all these cases, the Pt skins, generated by a post heat treatment, were kept at one or two atomic layers in thickness to ensure that the Pt coatings would not adversely impact the excellent ORR activity of the underlying Pt–Ni component.

Owing to the high bond energy of Pt–Pt (307 kJ mol^{-1}), island growth and self-nucleation can often prove challenging when trying to deposit Pt atoms as a conformal overlayer on the surface of a nanocrystal substrate [22]. It has been reported that monolayers or sub-monolayers of Pt could be deposited on nanocrystals made of another metal through the galvanic replacement reaction between underpotentially deposited monolayers of Cu and a Pt(II) precursor [23−25]. The capability of this method is, however, rather limited in terms of large scale production due to the necessary involvement of electrodes in the deposition process. Our group recently developed a robust protocol for coating Pd nanocrystals with Pt conformal shells of 1−6 atomic layers in thickness [9−11, 26]. The key to the success of this new coating protocol is the use of both a slow deposition kinetics and a relatively high reaction temperature, so the deposited Pt atoms could diffuse across the entire surface of a Pd nanocrystal to generate a Pt conformal shell in a layer-by-layer fashion. When benchmarked against a commercial Pt/C catalyst, the $Pd@Pt_{nL}$ (n = 1−6) core−shell nanocrystals showed great enhancement in terms of activity as well as durability toward ORR. In principle, this

protocol can be extended to generate Pt conformal shells on the surfaces of Pt–Ni octahedra with some minor modifications.

Here I demonstrate a new method for the conformal deposition of ultrathin shells of Pt on the surfaces of Pt−Ni octahedra to generate Pt−Ni@Pt octahedra *via* dropwise introduction of a Pt precursor into a suspension of Pt−Ni octahedra. After processing the Pt−Ni and Pt−Ni@Pt octahedra into carbon-supported catalysts, I evaluated their chemical stability in a harsh environment (*e.g.*, a strong acid) for an extended period of time. During the acid treatment, the Pt shells could effectively prevent the Ni from dissolution whereas a substantial loss of Ni was observed for the Pt−Ni counterparts without Pt shells. In addition to the improvement in chemical stability, the Pt−Ni@Pt octahedra catalyst showed significant enhancement in the electrocatalytic durability toward ORR relative to the Pt−Ni octahedra catalyst. After repeating 10,000 potential sweeps in an acidic electrolyte, the Pt−Ni@Pt octahedra exhibited a mass activity 2.6 times greater than the Pt−Ni octahedra or 9-fold higher than the initial mass activity of a state-of-the-art Pt/C catalyst.

3.2 Results and Discussion

Figure 3.1 shows a schematic illustration of the synthesis of Pt−Ni@Pt octahedral nanocrystals. I first synthesized Pt−Ni octahedra (11.2 nm in edge length, Figure 3.2A) using the protocol reported by our group with some minor modifications [14]. The as-synthesized Pt−Ni octahedra were directly used as seeds for the synthesis of Pt−Ni@Pt octahedra without further harvesting and washing. I deposited Pt shells onto the surfaces of the Pt−Ni octahedra by injecting a $Pt(acac)_2$ solution into the as-obtained suspension of Pt−Ni octahedra. One challenge to achieve conformal deposition of Pt shells is the formation of self-nucleated Pt nanoparticles or dendritic structures arising from the large Pt−Pt bond energy. To address these issues, we have to ensure that the diffusion rate of Pt adatoms across the surface of a seed is greater than the deposition rate of Pt atoms. In this

work, I met this requirement by dropwise introducing the Pt precursor through a syringe pump at a high reaction temperature of 200 ^{o}C. As shown in Figure 3.2B, Pt atoms could be deposited as smooth shells rather than islands or dendritic structures. The average edge length of the Pt−Ni@Pt octahedra was 11.8 nm. Based on the data obtained from ICP-MS analysis, the number of Pt atomic layers deposited on the Pt−Ni octahedra was around 1.5 (Table 3.1). Figure 3.2C shows a typical HAADF-STEM image taken from an individual Pt−Ni@$Pt_{1.5L}$ octahedron, confirming that a Pt shell was deposited conformally on the Pt−Ni octahedron. However, the presense of a Pt shell on the Pt−Ni octahedron could not be resolved by the EDX elemental mapping (Figure 3.2D). I attribute this to the formation of oxidized Ni species on the surface of the Pt−Ni octahedra during the synthesis, veiling the Pt shell [14].

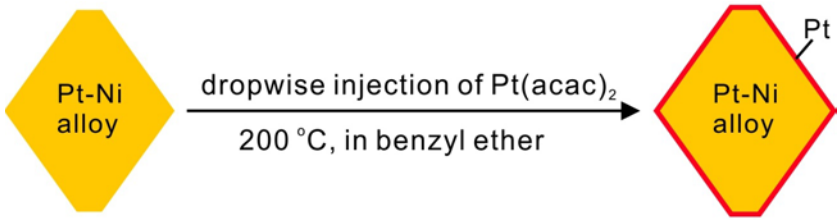

Figure 3.1. A schematic diagram showing the synthesis of a Pt−Ni@Pt octahedron *via* the deposition of an ultrathin Pt shell on the surface of a preformed Pt−Ni octahedron. To achieve the conformal deposition of Pt shells on the Pt−Ni octahedra, $Pt(acac)_2$ in benzyl ether is injected dropwise into a suspension of Pt−Ni octahedra at 200 ^{o}C.

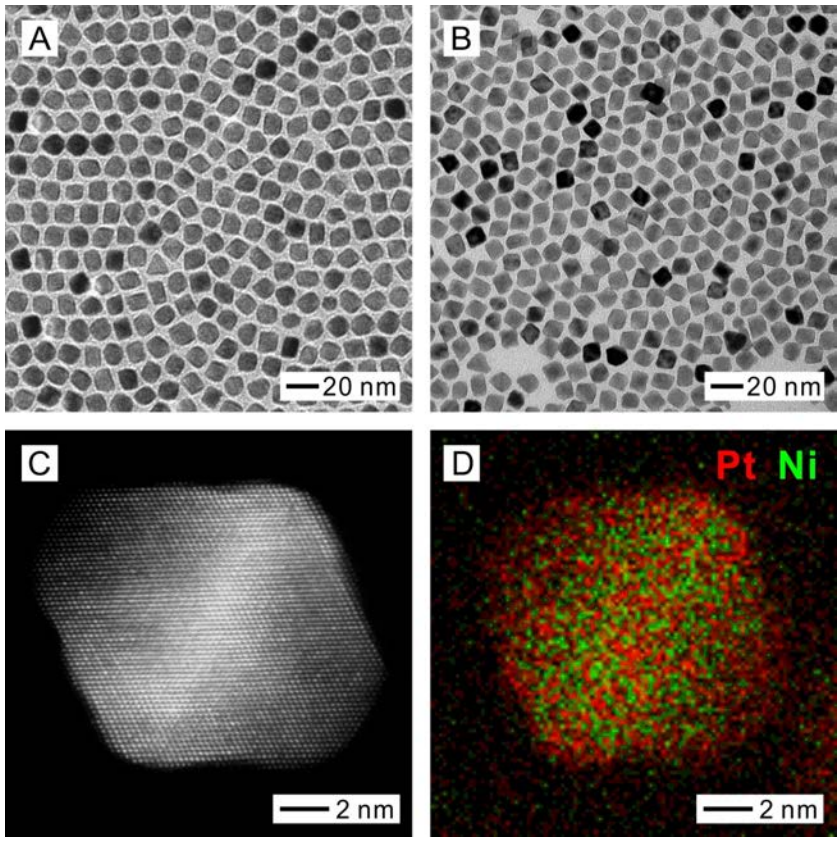

Figure 3.2. TEM images of (A) Pt−Ni and (B) Pt−Ni@$Pt_{1.5L}$ octahedra, respectively. (C) STEM image and (D) EDX elemental mapping of a Pt−Ni@$Pt_{1.5L}$ octahedron, respectively. For the EDX mapping, red and green colors represent Pt and Ni, respectively.

To remove the oxidized Ni from the surface of the Pt−Ni@$Pt_{1.5L}$ octahedra, I dispersed the particles on a carbon support (Ketjenblack EC-300J, AkzoNobel) to obtain Pt−Ni@$Pt_{1.5L}$/C, followed by treatment with HAc at 60 ^{o}C for 2 h. As shown in Figure 3.3A, the Pt−Ni@$Pt_{1.5L}$ octahedra did not show significant morphological changes after the HAc treatment. After the acid treatment, I could readily confirm the presence of Pt shells by EDX mapping (Figure 3.3C). The thickness of the Pt shells was estimated to be around 0.4 nm, corresponding to 1−2 atomic layer of Pt{111} planes. I also characterized the elemental compositions of the Pt−Ni@$Pt_{1.5L}$/C before and after the acid treatment using ICP-MS and the results are shown in Table 3.1.

Table 3.1. Comparison of the Pt/Ni molar ratios for Pt−Ni/C and Pt−Ni@$Pt_{1.5L}$/C catalysts measured by ICP-MS before and after treatments with acetic acid and/or sulfuric acid.

Catalysts	Pt/Ni molar ratio
Pt−Ni/C before the treatment	1.7
Pt−Ni/C after the treatment with acetic acid	2.1
Pt−Ni/C after the treatments with acetic acid and then sulfuric acid	2.3
Pt-Ni@$Pt_{1.5L}$/C before the treatment	2.2
Pt−Ni@$Pt_{1.5L}$/C after the treatment with acetic acid	2.5
Pt−Ni@$Pt_{1.5L}$/C after the treatments with acetic acid and then sulfuric acid	2.5

After treating the Pt−Ni@$Pt_{1.5L}$/C with HAc, the Pt/Ni molar ratio increased from 2.3 to 2.6. To systemically investigate this compositional change, I also measured the contents of Pt and Ni in the HAc solution after the treatment. This analysis indicates that 9% of the Ni was removed from the Pt−Ni@$Pt_{1.5L}$/C during the acetic acid treatment while the Pt content was well preserved. The XPS spectra (Figure 3.4C) taken from the Pt−Ni@$Pt_{1.5L}$/C provide more information regarding the loss of Ni caused by the HAc treatment. The peaks of $Ni(OH)_2$ disappeared whereas those of Ni(0) did not change significantly. These results clearly support the argument that the HAc treatment could effectively remove the $Ni(OH)_2$ from the surface of the catalytic particles. It is well-documented that the $Ni(OH)_2$ can have an adverse impact on the operation of a fuel cell

due to the poisoning of the ionomer and membrane [20, 14]. I also carried out HAc treatment for the carbon-supported Pt−Ni octahedra (Pt−Ni/C catalyst). Like the case of the Pt−Ni@$Pt_{1.5L}$/C, the HAc treatment did not markedly affect the morphology of the Pt−Ni octahedra (Figure 3.5A) but it could effectively remove $Ni(OH)_2$ from the surface of the catalytic particles (Table 3.1 and Figure 3.4A).

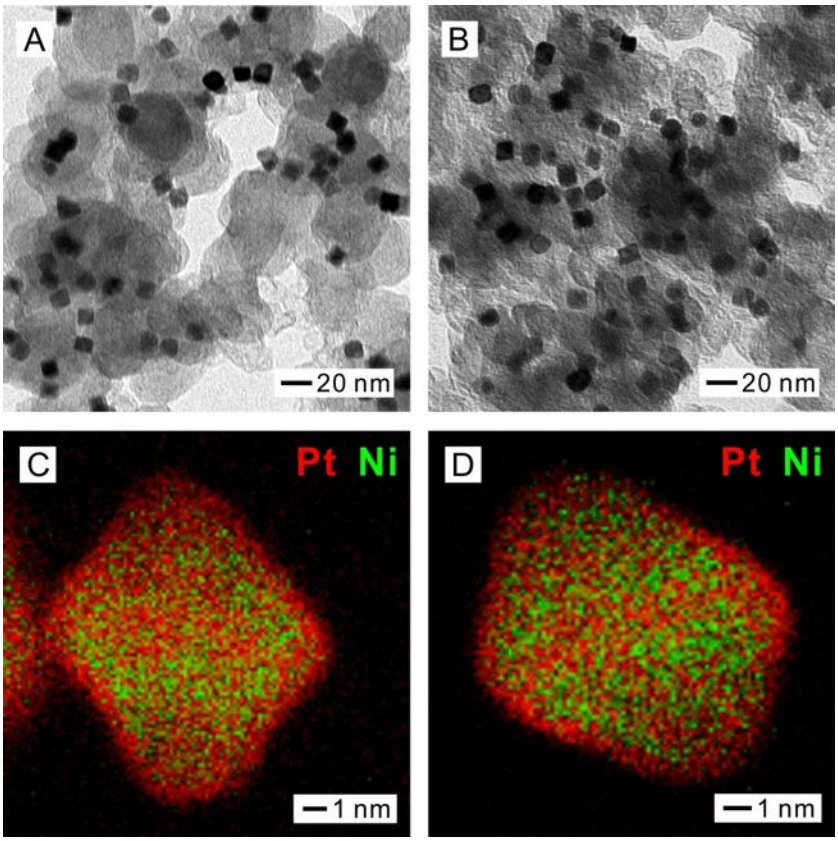

Figure 3.3. TEM images of (A) Pt−Ni@$Pt_{1.5L}$/C after the treatment with acetic acid and (B) Pt−Ni@$Pt_{1.5L}$/C after the treatment with acetic acid and then sulfuric acid. (C and D) EDX elemental mappings of an individual octahedron selected from samples (A) and (B), respectively.

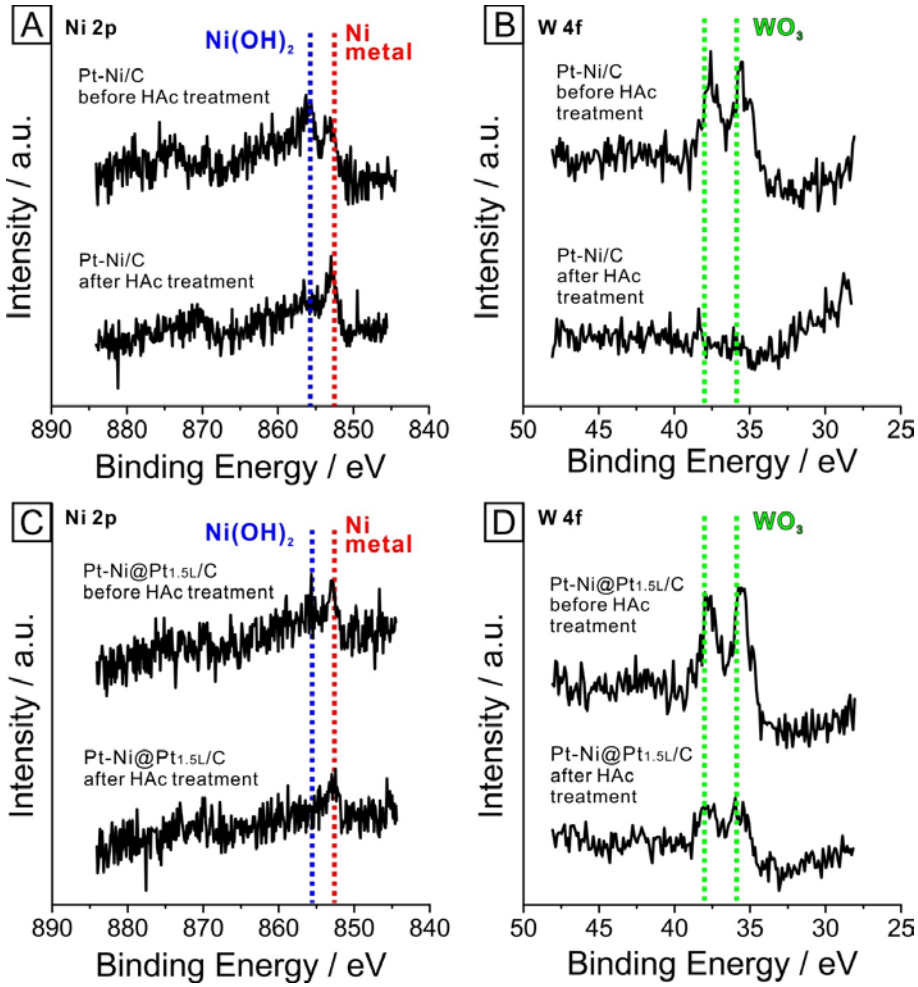

Figure 3.4. XPS spectra of (A and B) Pt−Ni/C and (C and D) Pt−Ni@$Pt_{1.5L}$/C catalysts measured before and after the treatment with HAc, respectively.

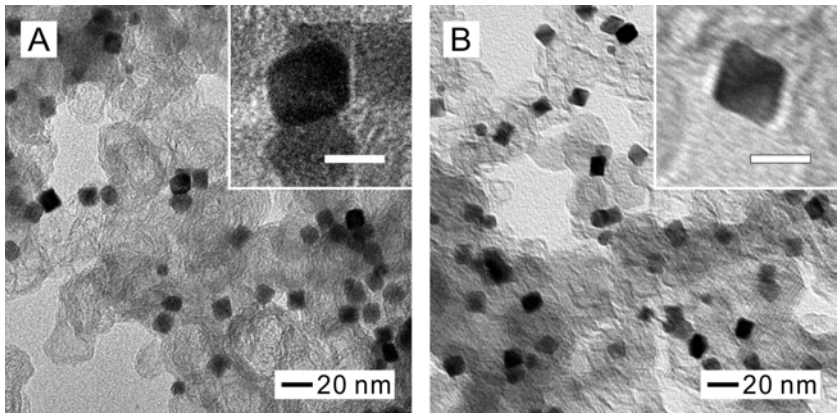

Figure 3.5. TEM images of (A) Pt−Ni/C after the treatment with acetic acid and (B) Pt−Ni/C after the treatment with acetic acid and then sulfuric acid. The insets show TEM images at a higher magnification (scale bar: 10 nm).

Since I added $W(CO)_6$ to help reduce the metal precursors and control the shape of the nanocrystals, a possible concern is that the final product is a Pt−Ni−W ternary alloy rather than a Pt−Ni binary alloy. To determine the content and oxidation state of tungsten (W) in both the Pt−Ni/C and Pt−Ni@$Pt_{1.5L}$/C catalysts, I conducted ICP-MS (Table 3.2) and XPS (Figure 3.4, B and D) analyses, respectively. The data confirmed that around 4.5 mol% of tungsten remained in both the Pt−Ni/C and Pt−Ni@$Pt_{1.5L}$/C catalysts and the W content was reduced to a negligible level after the HAc treatment. Furthermore, in the catalysts, the tungsten was found to exist as tungsten(VI) oxide (WO_3), rather than zero-valent tungsten, W(0). Taken together, I can exclude the formation of a Pt−Ni−W ternary alloy.

For the HAc-treated catalysts, I further incubated them in aqueous sulfuric acid (0.5 M) at 60 ^{o}C for 24 h under magnetic stirring to evaluate their long-term stability. I believe this condition can simulate the corrosive environment at the cathode of a PEMFC during its operation, involving both low pH and high oxygen content. After the treatment with sulfuric acid, both the catalytic particles in the Pt−Ni/C and Pt−Ni@$Pt_{1.5L}$/C catalysts showed very little changes to their morphology (Figure 3.3B and 3.5B). In particular, the Pt shells on the Pt−Ni@$Pt_{1.5L}$ octahedra were found to be well preserved in terms of uniformity as well as thickness during the sulfuric acid treatment (Figure 3.3D). However, the Pt−Ni/C and Pt−Ni@$Pt_{1.5L}$/C exhibited remarkable difference in terms of composition after the sulfuric acid treatment. While the Pt/Ni molar ratio of the Pt−Ni/C increased from 2.1 to 2.3 after the sulfuric acid treatment, that for the Pt−Ni@$Pt_{1.5L}$/C was maintained at 2.5 (Table 3.1). I also found that 11% of the Ni was dissolved from the Pt−Ni/C catalyst during the sulfuric acid treatment whereas only less than 1% of the Ni was lost for the Pt−Ni@$Pt_{1.5L}$/C. These results indicate that the ultrathin Pt shells on the surface of Pt−Ni octahedra could effectively protect the Pt−Ni alloy octahedra in the cores in a highly corrosive environment.

Table 3.2. Comparison of the tungsten (W) contents in the Pt−Ni/C and Pt−Ni@$Pt_{1.5L}$/C catalysts before and after the treatment with acetic acid, respectively. The W content is presented as mole percentage, $n_W/(n_{Pt}+n_{Ni}+n_W)$x100, where n represents the molar concentration of each component determined using ICP-MS.

Catalysts	W content (mol%)
Pt−Ni/C before the treatment	4.4
Pt−Ni/C after the treatment	0.8
Pt−Ni@$Pt_{1.5L}$/C before the treatment	4.5
Pt−Ni@$Pt_{1.5L}$/C after the treatment	2.8

I then examined the electrochemical properties of both the Pt−Ni/C and Pt−Ni@$Pt_{1.5L}$/C catalysts (after treatment with HAc) using the RDE method. In this case, I prepared another batch of the Pt−Ni@$Pt_{1.5L}$ octahedra using the same standard protocol except I reduced the reaction scale by one third for both the seeds and reagents involved. The physicochemical properties of the catalytic particles were essentially identical in terms of morphology and elemental composition (Figure 3.6). Before measuring ORR polarization curves, I preconditioned the catalysts by sweeping CVs in a N_2-saturated aqueous $HClO_4$ solution (typically 50 cycles from 0.08 to 1.1 V_{RHE}). The ORR polarization curves were measured in an O_2-saturated aqueous $HClO_4$ solution with a rotation speed of 1,600 rpm for the working electrode (Figure 3.7B). From each polarization curve, I calculated the kinetic current density (j_k) for ORR using the Koutecky−Levich equation and then normalized it to the ECSA for specific activity ($j_{k,specific}$) and to the Pt mass for mass activity ($j_{k,mass}$). The ECSA was calculated from the total charges corresponding to the desorption of underpotentially deposited Cu (Cu_{UPD}),

as shown in Figure 3.7A. Depending on the facets involved, the reference charge densities for the commercial Pt/C and the octahedra-based catalysts were assumed to be 420 and 480 μC cm^{-2}, respectively [27]. The CVs of Cu_{UPD} were measured in a solution of 50 mM H_2SO_4 and 50 mM $CuSO_4$ by sweeping potential from 0.3 to 0.8 V_{RHE} at rate of 0.05 V s^{-1}.

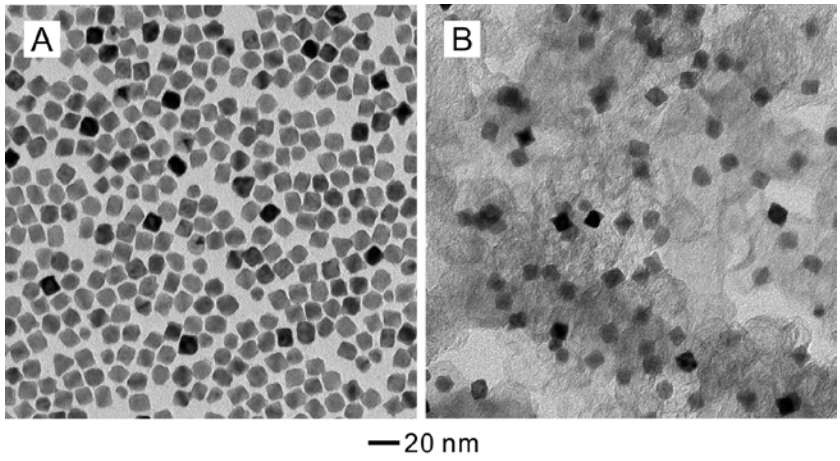

Figure 3.6. TEM images of (A) the as-obtained, freestanding Pt−Ni@$Pt_{1.5L}$ octahedra and (B) Pt−Ni@$Pt_{1.5L}$/C after the treatment with acetic acid, which was used for the ORR measurements and accelerated durability test. The Pt/Ni molar ratio was 2.2 and 2.5, respectively, for these two samples, which were almost identical to those for the samples shown in Figures, 3.2 and 3.3.

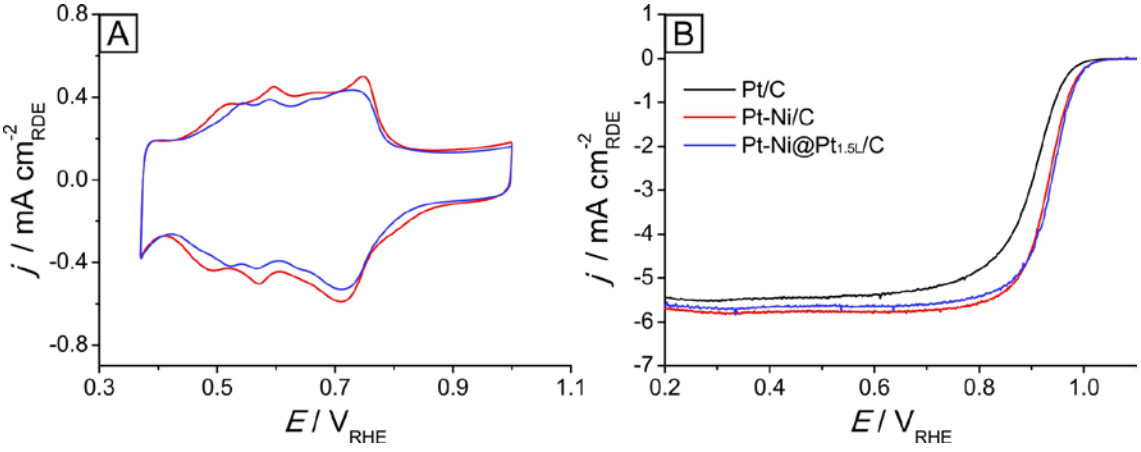

Figure 3.7. (A) CVs of Cu_{UPD} for the Pt−Ni/C and Pt−Ni@$Pt_{1.5L}$/C catalysts, respectively, and (B) ORR polarization curves recorded from the Pt/C, Pt−Ni/C, and Pt−Ni@$Pt_{1.5L}$/C catalysts, respectively.

To quantitatively compare the ORR activities of the catalysts, I selected mass and specific activities at 0.9 V_{RHE} and plotted them in Figure 3.8. Specifically, I compare the specific ECSAs, specific activities, and mass activities of the state-of-the-art Pt/C (20 wt% 3.2-nm Pt particles on Vulcan XC-72 carbon support, Premetek), the Pt−Ni/C, and the Pt−Ni@$Pt_{1.5L}$/C catalysts. As shown in Figure 3.8A, the specific ECSAs of the Pt−Ni/C and Pt−Ni@$Pt_{1.5L}$/C were 46 $m^2\ g_{Pt}^{-1}$ and 40 $m^2\ g_{Pt}^{-1}$, respectively, indicating a slight decrease due to the deposition of ultrathin Pt shells. The specific activities of the Pt−Ni/C and Pt−Ni@$Pt_{1.5L}$/C catalysts at 0.9 V_{RHE} were 5.7 and 5.6 mA cm_{Pt}^{-2}, respectively, and they both showed a 17-fold enhancement relative to that of the Pt/C catalyst (Figure 3.8B). It is worth pointing out that the Pt−Ni@$Pt_{1.5L}$/C still maintained a specific activity almost identical to that of the Pt−Ni/C despite the presence of an ultrathin Pt shell on the surface. Combined together, the mass activity of the Pt−Ni@$Pt_{1.5L}$/C catalyst was only compromised by 13% relative to the Pt−Ni/C catalyst. Significantly, the mass activity of the Pt−Ni@$Pt_{1.5L}$/C catalyst was still 12-fold higher than that of the state-of-the-art Pt/C, exceeding the recommended value by United States DOE in 2012 [28].

I used accelerated durability tests to compare the catalytic durability of different catalysts. The test was conducted by applying a linear potential sweep between 0.6 and 1.1 V_{RHE} at a rate of 0.1 V s^{-1} in an O_2-saturated aqueous $HClO_4$ solution at room temperature. As shown in Figure 3.8, the Pt−Ni@$Pt_{1.5L}$/C catalyst exhibited significantly improved durability compared to both the Pt−Ni/C and state-of-the-art Pt/C catalysts. The mass activity (at 0.9 V_{RHE}) of the Pt−Ni/C catalyst dropped by 55% and 75% after 5,000 and 10,000 potential cycles, respectively. In contrast, the mass activity of the Pt−Ni@$Pt_{1.5L}$/C only dropped by 6% and 25% after 5,000 and 10,000 cycles, respectively, confirming the role of ultrathin Pt shell in greatly enhancing the catalytic durability. The changes to mass activity during the durability tests correlated well to the changes in specific activity.

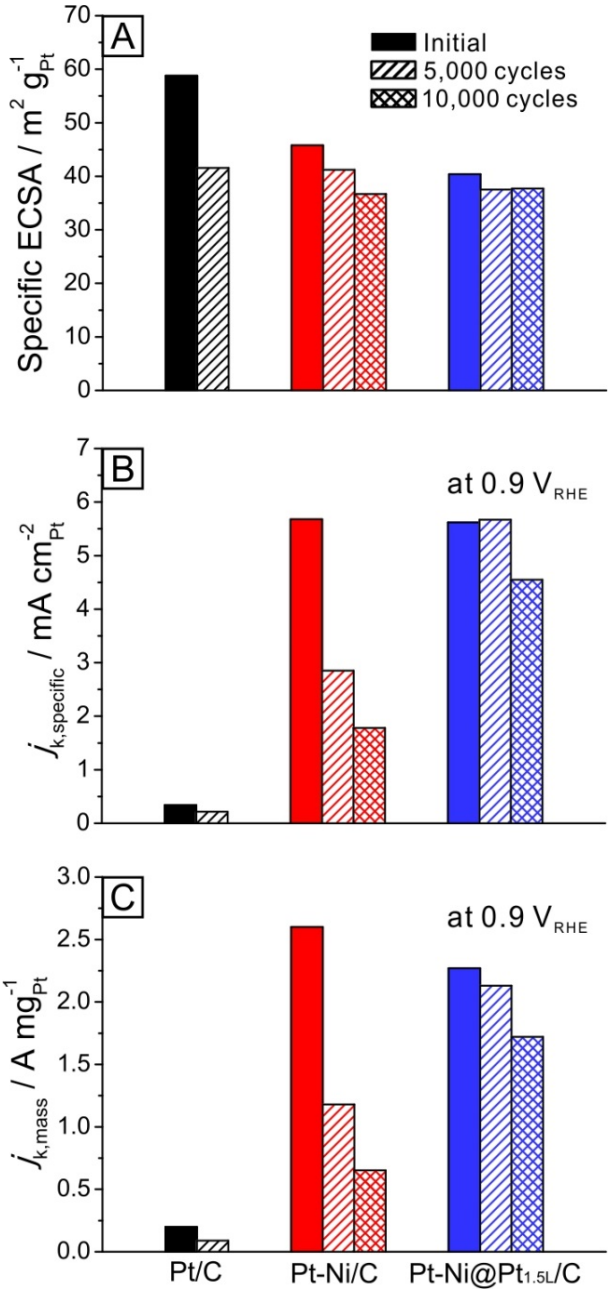

Figure 3.8. (A) Specific ECSAs, (B) specific ORR activities, and (C) mass ORR activities of the Pt/C (black), Pt−Ni/C (red), and Pt−Ni@$Pt_{1.5L}$/C (blue) catalysts before and after the accelerated durability tests. The ECSAs of the catalysts were obtained from the desorption peaks of CVs for Cu_{UPD}. The specific and mass activities were given as kinetic current densities (j_k) at 0.9 V_{RHE} normalized to the ECSAs of the catalysts and masses of Pt, respectively.

To achieve a better understanding of the changes to specific activity, I examined the catalysts after the accelerated durability tests by TEM. As shown in Figure 3.9, A and B, the Pt−Ni catalytic nanocrystals lost their original sharp corners and became spherical or irregular in shape after 10,000 cycles. It is worth pointing out that the morphological change to the Pt−Ni octahedra was similar to what was observed by Strasser and coworkers for $Pt_{1.5}Ni$ octahedra during repeated potential cycles [29]. In addition, I observed some aggregation among the Pt−Ni octahedra after the test. Different from the Pt−Ni/C, the catalytic nanocrystals in the Pt−Ni@$Pt_{1.5L}$/C catalyst essentially retained their original octahedral shape and no aggregation was observed even after 10,000 potential cycles (Figure 3.9, C and D). Taken together, it can be concluded that conformal deposition of ultrathin Pt shells on Pt−Ni octahedra could effectively enhance the long-term stability of the electrocatalyst toward ORR.

In addition to the accelerated durability tests, I compared the electrocatalytic properties of the Pt−Ni/C and Pt−Ni@$Pt_{1.5L}$/C catalysts before and after the treatments with sulfuric acid. While the Pt−Ni/C catalyst lost 28% of its original mass activity after the treatment with sulfuric acid, the Pt−Ni@$Pt_{1.5L}$/C catalyst only exhibited a loss of 1%. The significant drop in mass activity for the Pt−Ni/C catalyst can be largely attributed to the reduction in specific activity caused by the acid treatment. The reduction in specific activity for the Pt−Ni/C catalyst implies that the surface of the catalytic particles degraded during the acid treatment, including changes to elemental composition and the formation of surface defects due to the dissolution of Ni atoms. On the other hand, it was found that the Pt−Ni@$Pt_{1.5L}$/C retained its physicochemical and electrochemical properties during the acid treatment. These results suggest that the Pt−Ni@$Pt_{1.5L}$/C should be a better ORR catalyst than the Pt−Ni/C for any long-term use.

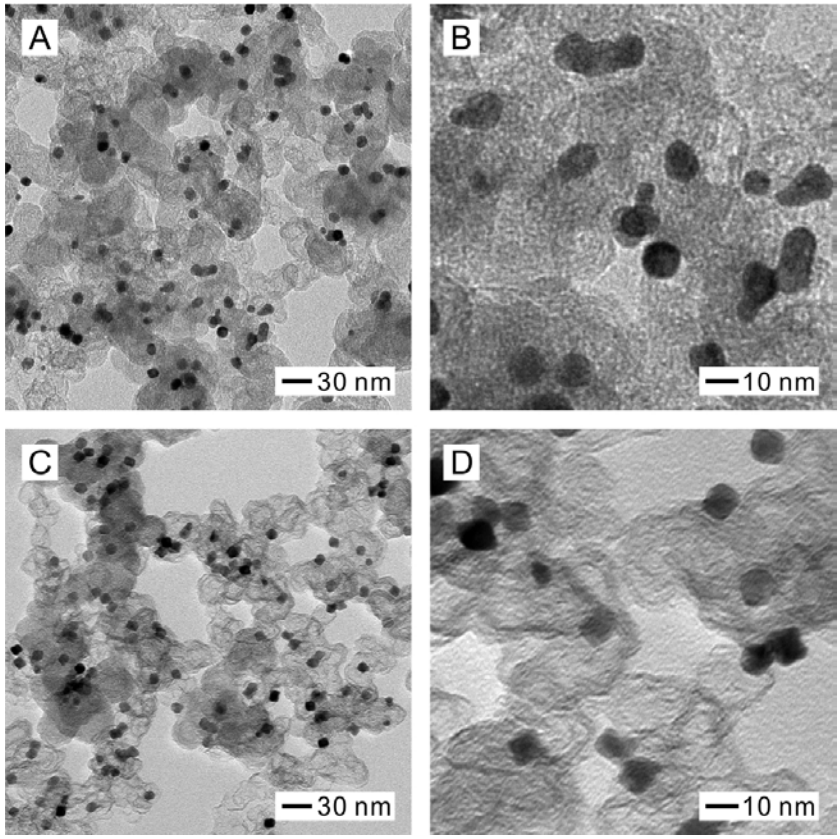

Figure 3.9. TEM images of (A and B) Pt−Ni/C and (C and D) Pt−Ni@$Pt_{1.5L}$/C catalysts, respectively, after the accelerated durability tests (10,000 potential cycles).

3.3 Summary

In this work, I have synthesized the Pt−Ni@$Pt_{1.5L}$ octahedra to improve the catalytic durability of ORR catalysts based upon Pt−Ni octahedra. The Pt−Ni@$Pt_{1.5L}$ octahedra were obtained through the conformal deposition of Pt thin shells on the surface of Pt−Ni octahedra, which was achieved by dropwise injecting a Pt precursor solution into the as-obtained suspension of Pt−Ni octahedra at 200 ^{o}C. To evaluate the long-term stability of both catalysts based upon the Pt−Ni and Pt−Ni@$Pt_{1.5L}$ octahedral nanocrystals, I have treated the catalysts by incubating them in the sulfuric acid at 60 ^{o}C for 24 h. The

Pt−Ni@$Pt_{1.5L}$/C catalyst exhibited significantly enhanced chemical stability as compared with the Pt−Ni/C catalyst in terms of the compositional changes during the treatment. The Pt−Ni@$Pt_{1.5L}$ octahedra maintained their original elemental composition during the treatment while the Pt−Ni octahedra lost 11% of Ni, suggesting that the thin Pt shells could effectively protect the Pt−Ni cores under the highly corrosive environment. In addition to the improvement in chemical stability, the Pt−Ni@$Pt_{1.5L}$/C catalyst showed remarkable enhancement in the electrocatalytic durability toward ORR relative to the Pt−Ni/C. While the mass activity of the Pt−Ni/C was dropped by 75% after 10,000 cycles of ORR, the mass activity of the Pt−Ni@$Pt_{1.5L}$/C was only reduced by 25%, which was 9-fold higher than the initial activity of the state-of-the-art Pt/C catalyst. The great improvement in durability suggests that the Pt−Ni@$Pt_{1.5L}$ octahedra would be promising for future use in commercial PEMFCs.

3.4 Experimental Section

Materials. All the chemicals were used as received from Sigma-Aldrich (unless specified). These include platinum(II) acetylacetonate ($Pt(acac)_2$, 98%, Acros Organics), nickel(II) acetylacetonate ($Ni(acac)_2$, 95%), tungsten hexacarbonyl ($W(CO)_6$, 99.99%), oleylamine (OAm, 70%), oleic acid (OAc, 90%), and benzyl ether (BE, 98%).

Synthesis of Pt−Ni Octahedra. For the synthesis of Pt−Ni octahedra, $Pt(acac)_2$ (60 mg), $Ni(acac)_2$ (24 mg), OAm (6 mL), OAc (2.4 mL), and BE (21 mL) were mixed in a 250 mL four-neck flask and heated to 130 °C (in an oil bath) under magnetic stirring and argon protection. Subsequently, $W(CO)_6$ (150 mg) was quickly added into the mixture held at 130 °C while argon purging was stopped at the same time. The mixture was then ramped to 230 °C at a rate of 10 °C min^{-1} and maintained at 230 °C for 40 min. The synthesis was terminated by naturally cooling down the reaction solution in air to room temperature (it took about 30 min). This as-obtained suspension containing Pt−Ni octahedra was directly used for the synthesis of Pt−Ni@$Pt_{1.5L}$ octahedra without further

separation and washing. Otherwise, the Pt−Ni octahedra were collected by centrifugation at 8,000 rpm for 10 min after adding toluene (30 mL) and ethanol (30 mL). The collected Pt–Ni octahedra were re-dispersed in toluene (30 mL) for the preparation of catalysts and further characterization.

Synthesis of Pt–Ni@$Pt_{1.5L}$ Octahedra. For a standard synthesis of Pt–Ni@$Pt_{1.5L}$ octahedra, the Pt–Ni octahedra were directly employed as seeds for Pt coating. After heating the as-obtained suspension of Pt–Ni octahedral seeds at 200 ^{o}C for 15 min, a $Pt(acac)_2$ solution in BE (0.5 mg mL^{-1}) was dropwise injected using a syringe pump at a rate of 12 mL h^{-1}. After 48 mL of the $Pt(acac)_2$ solution had been added, the reaction mixture was kept at 200 ^{o}C for another 1 hour under magnetic stirring and then cooled down to room temperature. The product was collected by centrifugation at 8,000 rpm for 10 min after adding toluene (50 mL) and ethanol (50 mL). The resulting Pt–Ni@$Pt_{1.5L}$ octahedra could be readily dispersed in toluene (30 mL). I also prepared some samples of Pt–Ni@$Pt_{1.5L}$ octahedra using the same protocol except for the reduction in scale (by one third) for the Pt−Ni octahedral seeds and all reagents involved.

Preparation of Pt–Ni/C and Pt–Ni@$Pt_{1.5L}$/C Catalysts. A specific amount of carbon black (Ketjenblack EC-300J, AkzoNobel) was added into 150 mL of toluene and then ultrasonicated for 10 min. A specific amount (to achieve a Pt loading of *ca.* 15 wt%) of the suspension of Pt–Ni or Pt–Ni@$Pt_{1.5L}$ octahedra in toluene was then added using a pipette. The mixture was ultrasonicated for 3 h and the resulting Pt–Ni/C or Pt–Ni@$Pt_{1.5L}$/C was collected by centrifugation at 12,000 rpm for 15 min. The catalyst was washed three times with toluene and dried in an oven at 60 ^{o}C for 30 min prior to the treatment with acid(s).

Treatment of the Pt–Ni/C or Pt–Ni@$Pt_{1.5L}$/C with Acetic and Sulfuric Acids. For the treatment of Pt–Ni/C or Pt–Ni@$Pt_{1.5L}$/C with HAc, 20 mg of the catalyst was dispersed in 10 mL of HAc (99.7%, Sigma-Aldrich) and then heated at 60 ^{o}C for 2 h under magnetic stirring. Afterwards, the catalyst was washed three times with ethanol and

dried in an oven at 60 ^{o}C for 30 min. I further treated the both catalysts with sulfuric acid (H_2SO_4). In this case, 20 mg of the catalyst was dispersed in 10 mL of aqueous H_2SO_4 (0.5 M, Sigma-Aldrich) and then heated at 60 ^{o}C for 24 h under magnetic stirring. Afterwards, the catalyst was washed three times with ethanol and dried in an oven at 60 ^{o}C for 30 min.

Morphological, Structural, and Elemental Characterizations. The TEM images were taken using a microscope (HT-7700, Hitachi) operated at 120 kV by drop-casting the samples on carbon-coated copper grids and drying under ambient conditions. Sub-angstrom resolution HAADF-STEM images of the nanocrystals were obtained on a JEOL ARM-200F TEM/STEM operated at 200 kV with a guaranteed resolution of 0.08 nm. The EDX mapping was conducted using a JEOL silicon drift detector with a large solid angle for fast elemental analysis. Before microscopy examination, the samples were ultrasonically dispersed in ethanol and then a drop of the solution was placed on a copper grid coated with a thin lacey carbon film. The elemental compositions of the samples were determined using ICP-MS (NexION 300Q, PerkinElmer).

Electrochemical Measurements. Electrochemical measurements were performed using a glassy carbon RDE (Pine Research Instrumentation) connected to a potentiostat (CHI 600E, CH Instruments). An ink for the electrochemical measurement was prepared by adding 1 mg of the carbon-supported catalyst into a mixture of DI water (0.5 mL), 2-propanol (0.5 mL, Sigma-Aldrich), and Nafion (5% solution, Sigma-Aldrich, 20 μL), followed by ultrasonication for 10 min. A working electrode was prepared by loading the ink (10 μL) on the glassy carbon electrode. Another working electrode was prepared from the state-of-the-art Pt catalyst (Pt/C, 20 wt% 3.2-nm nanoparticles on Vulcan XC-72 carbon support, Premetek) using the same protocol. An RHE (Gaskastel) and a Pt coil (Pine Research Instrumentation) were used as the reference and counter electrodes, respectively. The electrolyte was an aqueous $HClO_4$ solution (70%, double-distilled, GFS chemicals) of 0.1 M in concentration. Some of the impurities on the surface of the

catalyst could be removed using a nondestructive method at room temperature by holding the electrode potential at −0.05 V_{RHE} for 1 min. The CVs were measured in a N_2-saturated electrolyte by cycling between 0.08 and 1.1 V_{RHE} at a sweep rate of 0.05 V s^{-1}. The ORR test was carried out in an O_2-saturated electrolyte with a scan rate of 0.01 V s^{-1} and a rotation speed of 1,600 rpm. All polarization curves were corrected for *iR*-contribution within the RDE measurement system. The kinetic current density (j_k) was derived from the Koutecky−Levich equation as follows:

$$\frac{1}{j} = \frac{1}{j_k} + \frac{1}{j_d}$$

where j is the measured current density and j_d is the diffusion-limiting current density. The UPD of Cu was conducted in a solution of 50 mM H_2SO_4 and 50 mM $CuSO_4$ by sweeping potential from 0.3 to 0.8 V_{RHE} at a rate of 0.05 V s^{-1}. To calculate the ECSA, I measured the charges generated from the desorption of Cu between 0.35 and 0.75 V_{RHE} with a reference value of 420 (Pt/C) or 480 μC cm^{-2} (octahedra) for the desorption of a monolayer of Cu from a Pt surface and then divided by the mass of Pt loaded on the working electrode. For the accelerated durability tests, the CVs and ORR polarization curves were measured after sweeping 5,000 and 10,000 cycles between 0.6 and 1.1 V_{RHE} at a rate of 0.1 V s^{-1} in an O_2-saturated aqueous $HClO_4$ solution at room temperature.

3.5 References

[1] Mayrhofer, K. J. J.; Strmcnik, D.; Blizanac, B. B.; Stamenkovic, V.; Arenz, M.; Markovic, N. M. *Electrochimica Acta* **2008**, *53*, 3181−3188.

[2] Greeley, J.; Rossmeisl, J.; Hellman, A.; Nørskov, J. K. *Z. Phys. Chem.* **2007**, *221*, 1209−1220.

[3] Wang, C.; Daimon, H.; Onodera, T.; Koda, T.; Sun, S. *Angew. Chem. Int. Ed.* **2008**,

47, 3588−3591.

[4] Zhou, W.; Wu, J.; Yang, H. *Nano Lett.* **2013**, *13*, 2870−2874.

[5] Lim, B.; Jiang, M.; Camargo, P. H. C.; Cho, E. C.; Tao, J.; Lu, X.; Zhu, Y.; Xia, Y. *Science* **2009**, *5*, 1302−1305.

[6] Strasser, P.; Koh, S.; Anniyev, T.; Greeley, J.; More, K.; Yu, C.; Liu, Z.; Kaya, S.; Nordlund, D.; Ogasawara, H.; Toney, M. F.; Nilsson, A. *Nat. Chem.* **2010**, *2*, 454−460.

[7] Choi, S.-I.; Shao, M.; Lu, N.; Ruditskiy, A.; Peng, H.-C.; Park, J.; Guerrero, S.; Wang, J.; Kim, M. J.; Xia, Y. *ACS Nano* **2014**, *8*, 10363−10371.

[8] Chen, C.; Kang, Y.; Huo, Z.; Zhu, Z.; Huang, W.; Xin, H. L.; Snyder, J. D.; Li, D.; Herron, J. A.; Mavrikakis, M.; Chi, M.; More, K. L.; Li, Y.; Markovic, N. M.; Somorjai, G. A.; Yang, P.; Stamenkovic, V. R. *Science* **2014**, *343*, 1339−1343.

[9] Xie, S.; Choi, S.-I.; Lu, N.; Roling, L. T.; Herron, J. A.; Zhang, L.; Park, J.; Wang, J.; Kim, M. J.; Xie, Z.; Mavrikakis, M.; Xia, Y. *Nano. Lett.* **2014**, *14*, 3570−3576.

[10] Park, J.; Zhang, L.; Choi, S.-I.; Roling, L. T.; Lu, N.; Herron, J. A.; Xie, S.; Wang, J.; Kim, M. J.; Mavrikakis, M.; Xia, Y. *ACS Nano* **2015**, *9*, 2635−2647.

[11] Wang, X.; Choi, S.-I.; Roling, L. T.; Luo, M.; Ma, C.; Zhang, L.; Chi, M.; Liu, J.; Xie, Z.; Herron, J. A.; Mavrikakis, M.; Xia, Y. *Nat. Commun.* **2015**, *6*, 7594.

[12] Zhang, L.; Roling, L. T.; Wang, X.; Vara, M.; Chi, M.; Liu, J.; Choi, S.-I.; Park, J.; Herron, J. A.; Xie, Z.; Mavrikakis, M.; Xia, Y. *Science* **2015**, *349*, 412−416.

[13] Stamenkovic, V. R.; Mun, B. S.; Arenz, M.; Mayrhofer, K. J. J.; Lucas, C. A.; Wang, G.; Ross, P. N.; Marković, N. M. *Nat. Mater.* **2007**, *6*, 241−247.

[14] Choi, S.-I.; Xie, S.; Shao, M.; Odell, J. H.; Lu, N.; Peng, H.-C.; Protsailo, L.; Guerrero, S.; Park, J.; Xia, X.; Wang, J.; Kim, M. J.; Xia, Y. *Nano Lett.* **2013**, *13*, 3420−3425.

[15] Wang, D.; Xin, H. L.; Hovden, R.; Wang, H.; Yu, Y.; Muller, D. A.; DiSalvo, F. J.; Abruña, H. D. *Nat. Mater.* **2013**, *12*, 81−87.

[16] Choi, S.-I.; Xie, S.; Shao, M.; Lu, N.; Guerrero, S.; Odell, J. H.; Park, J.; Wang, J.; Kim, M. J.; Xia, Y. *ChemSusChem* **2014**, *7*, 1476−1483.

[17] Sun, X.; Jiang, K.; Zhang, N.; Guo, S.; Huang, X. *ACS Nano* **2015**, *9*, 7634−7640.

[18] Huang, X.; Zhao, Z.; Cao, L.; Chen, Y.; Zhu, E.; Lin, Z.; Li, M.; Yan, A.; Zettl, A.; Wang, Y. M.; Duan, X.; Mueller, T.; Huang, Y. *Science* **2015**, *348*, 1230−1234.

[19] Kang, Y.; Snyder, J.; Chi, M.; Li, D.; More, K. L.; Markovic, N. M.; Stamenkovic, V. R. *Nano Lett.* **2014**, *14*, 6361−6367.

[20] Gasteiger, H. A.; Kocha, S. S.; Sompalli, B.; Wagner, F. T. *Appl. Catal., B* **2005**, *56*, 9−35.

[21] Zhu, H.; Zhang, S.; Su, D.; Jiang, G.; Sun, S. *Small* **2015**, *11*, 3545−3549.

[22] Zhang, H.; Jin, M.; Xia, Y. *Chem. Soc. Rev.* **2012**, *41*, 8035−8049.

[23] Zhang, J.; Vukmirovic, M. B.; Xu, Y.; Mavrikakis, M.; Adzic, R. R. *Angew. Chem. Int. Ed.* **2005**, *44*, 2132−2135.

[24] Adzic, R. R.; Zhang, J.; Sasaki, K.; Vukmirovic, M. B.; Shao, M.; Wang, J. X.; Nilekar, A. U.; Mavrikakis, M.; Valerio, J. A.; Uribe, F. *Top. Catal.* **2007**, *46*, 249−262.

[25] Shao, M.; He, G.; Peles, A.; Odell, J. H.; Zeng, J.; Su, D.; Tao, J.; Yu, T.; Zhu, Y.; Xia, Y. *Chem. Commun.* **2013**, *49*, 9030−9032.

[26] Xia, X.; Xie, S.; Liu, M.; Peng, H.-C.; Lu, N.; Wang, J.; Kim, M. J.; Xia, Y. *P. Natl. Acad. Sci. U. S. A.* **2013**, *110*, 6669−6673.

[27] Shao, M.; Odell, J. H.; Choi, S.-I.; Xia, Y. *Electrochem. Commun.* **2013**, *31*, 46−48.

[28] Department of Energy. *Multi-Year Research, Development and Demonstration Plan*, http://www.eere.energy.gov, 2012.

[29] Cui, C.; Gan, L.; Heggen, M.; Rudi, S.; Strasser, P. *Nat. Mater*. **2013**, 12, 765−771.

CHAPTER 4

PLATINUM CUBIC NANOFRAMES WITH ENHANCED CATALYTIC DURABILITY TOWARD OXYGEN REDUCTION

4.1 Introduction

As discussed in Chapter 1, the current commercial ORR catalysts are based upon Pt nanoparticles of 3−5 nm in size. Despite their extremely high specific ECSAs, the commercial Pt/C catalysts suffer from poor durability, not mentioning their low specific activity, which can be attributed to the low-coordinated Pt atoms on the surface [1, 2]. To address these issues, researchers have been searching for strategies that can enhance both the catalytic activity and durability of an ORR catalyst by tailoring the crystal facets, composition, and structure of the nanoparticles involved [3−10]. Please refer to Chapter 1 for a detailed discussion of these strategies. As I demonstrated in Chapters 2 and 3, deposition of a few atomic layers of Pt on the surface of facet-controlled nanocrystals made of another metal, such as Pd or Pt−Ni alloy, offers an attractive strategy for increasing the mass activity while greatly enhancing the durability [11−18]. However, these core−shell nanocrystals are not the optimal structure for maximizing the utilization efficiency of Pt atoms since the interior surfaces of the Pt shell are inaccessible for catalyzing chemicals.

In order to involve both the outer and inner Pt surfaces in the catalysis, in 2015 the Xia group successfully fabricated Pt-based hollow nanocages comprising well-defined facets by selectively etching away Pd cores from the Pd@Pt_{nL} nanocrystals [10]. The catalyst based upon the nanocages exhibited great enhancement in both mass activity and durability when compared to the Pt/C. An alternative strategy is to use nanoframes composed of ultrathin ridges (a few nanometers in thickness). In addition to the extremely high specific surface area, the nanoframes, as a highly open structure, provide

another advantage in terms of accelerated diffusion of the chemicals involved and thus enhancement of overall kinetics of catalytic reaction. In 2014, the Yang and Stamenkovic groups developed an ORR catalyst based upon Pt_3Ni alloy nanoframes and achieved an extraordinary mass activity of 5.7 A mg_{Pt}^{-1} at 0.9 V_{RHE} [9]. However, this catalyst still faces challenges arising from the use of a transition metal such as Ni, which can be readily oxidized and leached from the catalyst during long-term operation of the fuel cell. Relative to Pt, transition metals have lower reduction potentials and thus can be readily dissolved under the highly corrosive environment at the cathode of a PEMFC. As discussed in Chapter 3, the dissolution of Ni from the Pt−Ni alloy can lead to decrease in specific activity for the catalyst as well as deterioration of the device due to contamination of the membrane or ionomer [19]. For these reasons, nanoframes made of pure Pt should be considered as an ORR catalyst despite the compromised specific activity.

In general, the nanoframes based on noble metals can be synthesized using a combination of two steps: *i*) site-selectied overgrowth of a noble metal on a template and *ii*) selective removal of the template [20−24]. To this end, the Xia group demonstrated, in 2012, the synthesis of Rh cubic nanoframes with well-controlled structures and ridge thickness through selective removal of the Pd cores from the Pd–Rh core−frame nanocubes [21]. In this synthesis, Pd nanocubes served as a template and Rh was deposited specifically onto corners and edges of the Pd nanocubes. The site-selected growth of Rh atoms on the Pd cubic template was accomplished through both kinetic control of Rh deposition and the involvement of Br^- ions for blocking the Pd{100} side faces from the deposition of Rh. Although this strategy is extendable to the synthesis of Pt nanoframes, formation of dendritic Pt on Pd or self-nucleated Pt nanoparticles remains a challenge in obtaining Pd−Pt core−frame nanocubes due to the relatively high bond energy of Pt−Pt [17, 25]. To address this issue, the kinetics for diffusion of Pt adatoms

across the Pd surface should be carefully controlled during the overgrowth of Pt on the Pd cubes [26].

In this chapter, I developed a new ORR catalyst based upon the Pt cubic nanoframes composed of thin ridges (<2 nm). For the synthesis of Pt nanoframes, I obtained the Pd−Pt core−frame nanocubes *via* site-selected deposition of Pt on Pd nanocubes. The kinetics for the deposition of Pt atom and the diffusion of Pt adatoms were carefully controlled through the injection rate of the Pt precursor and reaction temperature, respectively. To generate Pt cubic nanoframes, the Pd templates were selectively removed by chemical etching with H_2O_2, HCl, and Br^- ions. I then evaluated the electrocatalytic properties of the catalyst based on the Pt nanoframes toward the ORR by benchmarking against a commercial Pt/C. Even though the Pt frame/C catalyst showed only 1.5 times higher initial mass activity relative to Pt/C, the catalytic durability was surprisingly improved. While repeating the potential sweeps (0.6−1.1 V_{RHE}) up to 30,000 cycles, the mass activity of the Pt frames/C rose up to 1.4 times higher than its initial value. Based on the results, the Pt frames/C catalyst is anticipated as another candidate to replace the commercial Pt/C catalyst for ORR.

4.2 Results and Discussion

Figure 4.1 shows a schematic illustration describing the synthesis of Pt cubic nanoframes. Two major steps are involved: (A) deposition of Pt atoms on the edges and corners of Pd nanocubes and (B) selective etching of the Pd nanocubes. For the synthesis of Pt nanoframes, I used Pd nanocubes of 18 nm in edge length (Figure 4.2) as templates, whose ridges and corners were slightly truncated. It is important to note that the side faces of the Pd nanocubes, composed of {100} facets, were capped by Br^- ions. For the deposition process of Pt atoms, a Pt precursor was dropwise injected into the reaction solution at a slow rate using a syringe pump in order to avoid self-nucleation of the Pt atoms. During deposition, the Pt atoms were initially deposited onto the corners and

ridges of the Pd nanocube because of their higher surface energy relative to the side faces capped with the Br^- ions (1). The deposited Pt adatoms on the corner and ridge sites then diffused across the ridges (2) and also side faces (3) of the Pd nanocube. It is worth pointing out that the Pt adatoms across the ridges (2) should be more predominant than that to the side faces (3), since the side faces of the Pd cube are blocked by Br^- ions. The Pd core of resultant Pd−Pt core−frame nanocube was selectively removed by a chemical etching. During the etching process, Pd tend to be oxidized and dissolved much faster than Pt due to its lower reduction potential than that of Pt. Thus, the Pd nanocube could act as a template for the synthesis of Pt cubic nanoframe, selectively being removed. In an acidic medium, H_2O_2 is able to oxidize the zero-valent Pd to Pd^{2+} ions. The Br^- ions from KBr also contributed to the oxidation of the Pd atoms by decreasing their reduction potential.

Figure 4.3A shows TEM images of Pd−Pt core−frame nanocubes obtained by dropwise introducing Na_2PtCl_6 solution (in EG) into a reaction solution containing Pd nanocubes at 190 ^oC. Due to both the slow injection rate and low concentration of the Pt precursor solution, I obtained the Pd−Pt core−frame nanocubes with a purity approaching 100%, avoiding self-nucleation of Pt atoms. Different from the flat side faces of Pd nanocubes (Figure 4.2), the Pd−Pt core−frame nanocubes instead showed concave side faces, indicative of the preferred deposition of Pt on the edge and corner sites. To further confirm the morphology, I took TEM images from a Pd−Pt core−frame nanocube by tilting the TEM grid. Figure 4.3C shows the TEM images of the Pd−Pt core−frame nanocube taken at tilting angles of -20^o, 0^o, and $+20^o$, respectively, and their corresponding atomic models. In the atomic models, the gray, blue, and red spheres represent Pd atoms, Pt atoms, and Br^- ions, respectively.

In order to selectively remove the Pd cubes, I added the Pd−Pt core−frame nanocubes into an aqueous solution containing H_2O_2, KBr, HCl, and PVP, and then heated the mixture to 100 ^oC for 2 h. During the etching process, zero-valent Pd atoms can be

oxidized to $PdBr_4^{2-}$ by H_2O_2 and then dissolved. After the etching, I measured the Pd content in the nanoframes using ICP-MS which was less than 5 wt%, confirming that Pd was successfully removed from the Pd−Pt core−frame nanocubes. Figure 4.3B shows a TEM image of the Pt cubic nanoframes obtained through etching of the Pd−Pt core−frame nanocubes. Even though I observed some frames with broken ridges, most of the frames still maintained the cubic structure after removal of the Pd cores. The average thickness of the ridges on the cubic frames was measured as ~1.7 nm. Some side faces were observed at around the corners of cubic frames, which were formed by surface diffusion of Pt adatoms from the corners to side faces during the deposition process. However, the surface diffusion to the side faces was limited since the side faces of Pd cubes were blocked by the Br^- ions. By taking TEM images of a Pt cubic nanoframe at different tilting angles, I could further confirm the cubic frame structure (Figure 4.3D).

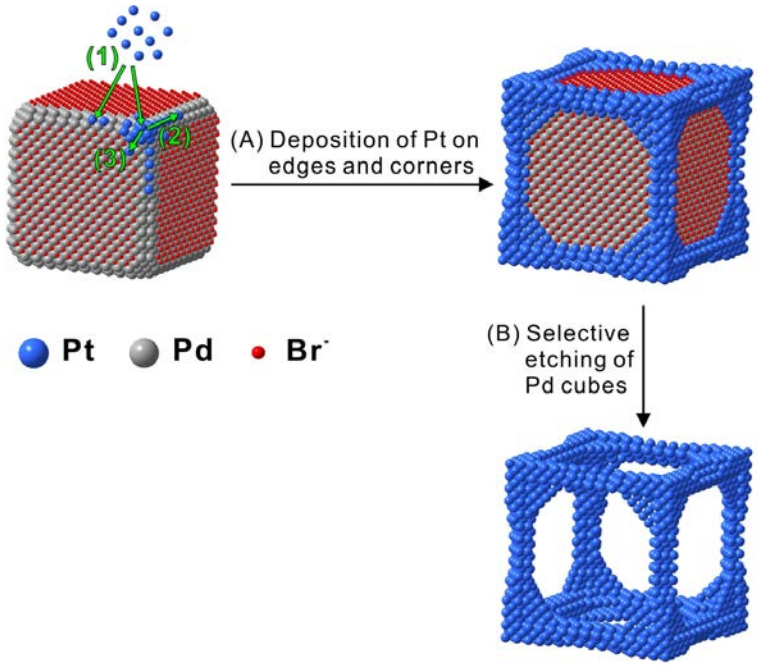

Figure 4.1. Schematic illustration of the synthesis of a Pt cubic nanoframe: (A) formation of a Pd−Pt core−frame nanocube through site-selected deposition of Pt atoms (blue) on a Pd nanocube (gray) and (B) generation of a Pt cubic nanoframe by selective removal of the Pd cubic core.

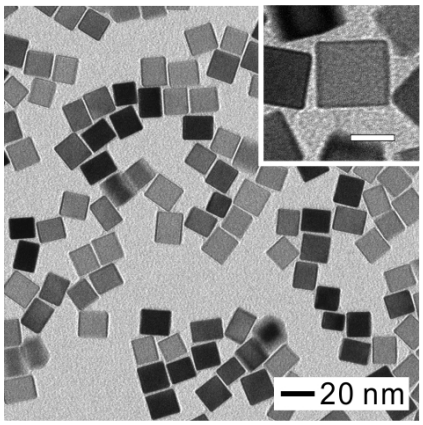

Figure 4.2. TEM image of Pd nanocubes used as seeds for the synthesis of Pd−Pt core−frame nanocubes. The inset shows a TEM image at a high magnification (scale bar: 10 nm).

To better understand the effect of temperature on the deposition process, I conducted deposition of Pt on Pd nanocubes at lower (170 ^{o}C) and higher (200 ^{o}C) temperatures, maintaining the other conditions of the standard protocol. When I conducted the Pt deposition at 170 ^{o}C, Pt dendrites grew along the edges and corners of the cubic seeds instead of forming the smooth ridges observed at 190 ^{o}C (Figure 4.4A). In this case, the surface diffusion rate of the Pt adatoms decreased relative to the standard protocol due to the lower temperature, thus resulting in island growth and the formation of the Pt dendrites on the edges and corners of the Pd nanocube. After etching away the Pd nanocubes, I observed many Pt dendrites on the Pt frames (Figure 4.4B). On the other hand, when the Pt deposition was carried out at 200 °C, I obtained cubic nanocrystals enclosed by slightly concave side faces instead (Figure 4.4C). As the surface diffusion rate increased at higher temperature, no dendritic Pt was generated in this case. Rather, Pt adatoms readily diffused from the edges and corners to the side faces, forming core−shell structures. This was further confirmed by the etching of the nanocrystals, resulting in Pt cubic nanocages with a large amount of side faces intact (Figure 4.4D). Based upon these results, I could conclude that the temperature for Pt deposition is a critical factor in

controlling the surface diffusion rate of Pt adatoms and in determining the structure of Pd−Pt bi-metallic nanocrystals generated through the seed-mediated synthesis.

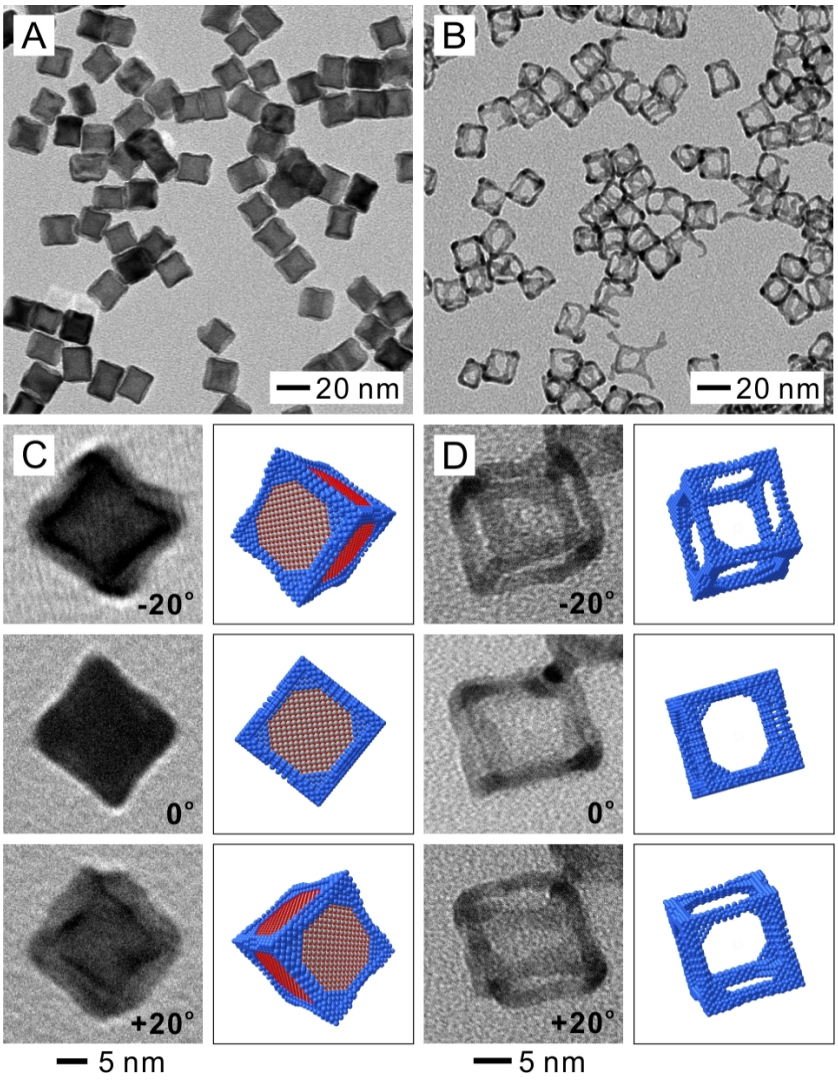

Figure 4.3. TEM images of (A) Pd−Pt core−frame nanocubes and (B) Pt cubic nanoframes. TEM images and corresponding atomic models of (C) a Pd−Pt core−frame nanocube and (D) a Pt cubic nanoframe. To confirm the morphology, the TEM images of each single nanocrystal in C and D were obtained by tilting TEM grids with three different tilting angles of -20^{o}, 0^{o}, $+20^{o}$, respectively. In the atomic models, blue, gray, and red colors represent Pt, Pd, and Br^{-}, respectively.

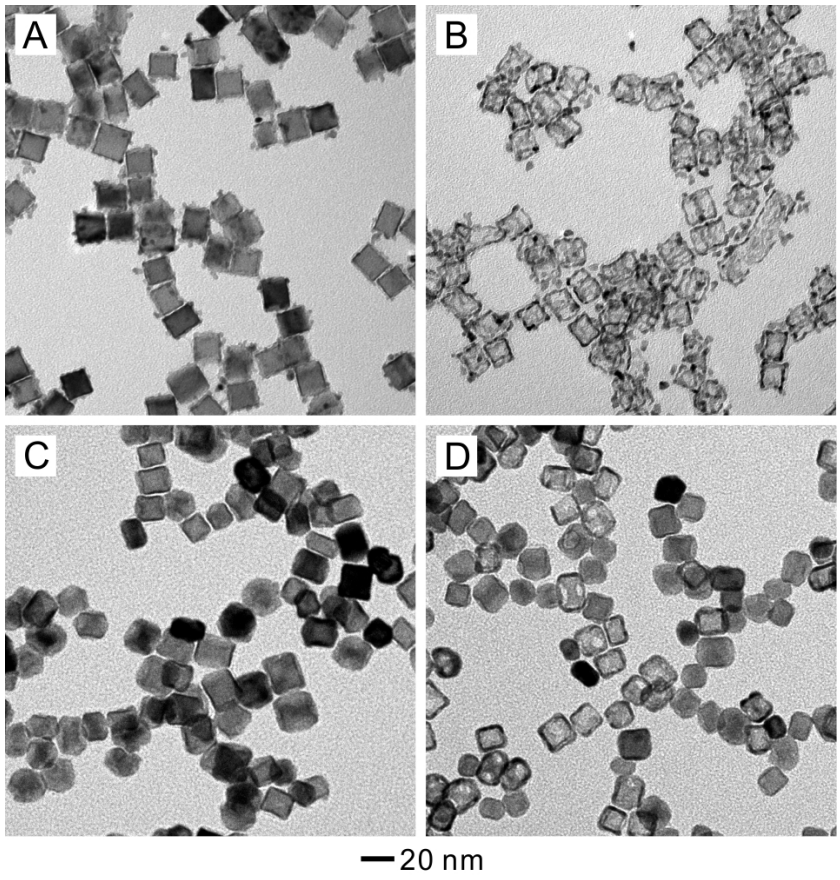

Figure 4.4. (A and C) TEM images of Pd−Pt nanocrystals obtained through deposition of Pt at (A) 170 and (C) 200 ^{o}C. (B and D) TEM images of nanocrystals obtained through etching the Pd−Pt nanocrystals in A and B, respectively.

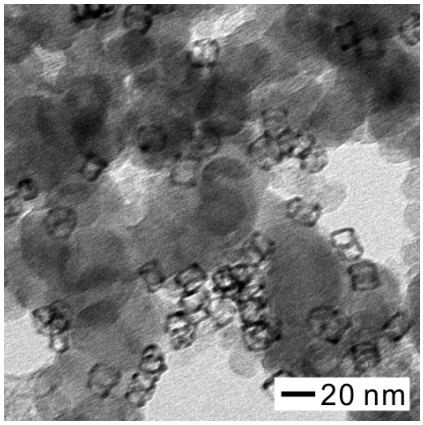

Figure 4.5. TEM image of the Pt frames/C catalyst before the ORR measurement.

In order to evaluate the electrocatalytic performance of the Pt cubic nanoframes toward ORR, I dispersed them on a carbon support, obtaining the Pt frames/C catalyst (Figure 4.5). To minimize the impact of the support on the catalytic performance, I employed the same carbon (Vulcan XC-72, Cabot) as the one used for the commercial Pt/C catalyst (Premetek). Prior to the electrocatalytic study, I treated the Pt frames/C catalyst by incubating it in acetic acid at 60 ^{o}C for 2 h to remove any residual PVP.

Figure 4.6 shows CVs and ORR polarization curves of the Pt frames/C catalyst (A and C) and the commercial Pt/C (B and D), respectively. To evaluate their catalytic durability, I took measurements before and after applying 5,000, 10,000, 15,000, 20,000, 25,000 (only for the Pt frames/C), and 30,000 (only for the Pt frames/C) cycles of linear potential sweeps between 0.6 and 1.1 V_{RHE} in an O_2-saturated aqueous $HClO_4$ solution (0.1 M). From the CVs, I derived ECSAs of the catalyst based upon the charges associated with both the adsorption and desorption of the underpotentially deposited hydrogen. In Figure 4.7A, I plotted the specific ECSAs of the Pt frames/C relative to the repeated potential cycles. From the ORR polarization curves, I calculated the kinetic current densities (j_k) using the Koutecky−Levich equation and then normalized them to the ECSAs and Pt mass to obtain the specific activity ($j_{k,specific}$) and mass activity ($j_{k,mass}$), respectively. For a quantitative comparison of the catalytic activities, I focused on the specific (Figure 4.7C) and mass ORR activities (Figure 4.7D) at 0.9 V_{RHE}.

As shown in Figure 4.7D, the initial mass activity (at 0.9 V_{RHE}) of the Pt frames/C was 0.45 A mg_{Pt}^{-1}, and it gradually increased up to 0.82 A mg_{Pt}^{-1} over the first 15,000 cycles of potential sweep. However, it fell to 0.61 A mg_{Pt}^{-1} while further cycling 15,000 potential sweeps. To understand this trend in the observed mass activity, I investigated the specific activity and the specific ECSA of the catalyst with repeating potential cycles. The specific activity (at 0.9 V_{RHE}) increased from 0.53 to 1.17 mA cm_{Pt}^{-2} during the first 15,000 potential cycles and it was maintained at around 1.10 mA cm_{Pt}^{-2} until the 30,000 cycles (Figure 4.7C). However, the specific ECSA of the Pt frames/C steadily decreased

from 85 to 55 m^2 g_{Pt}^{-1} while I repeated potential sweeping up to 30,000 cycles (Figure 4.7A).

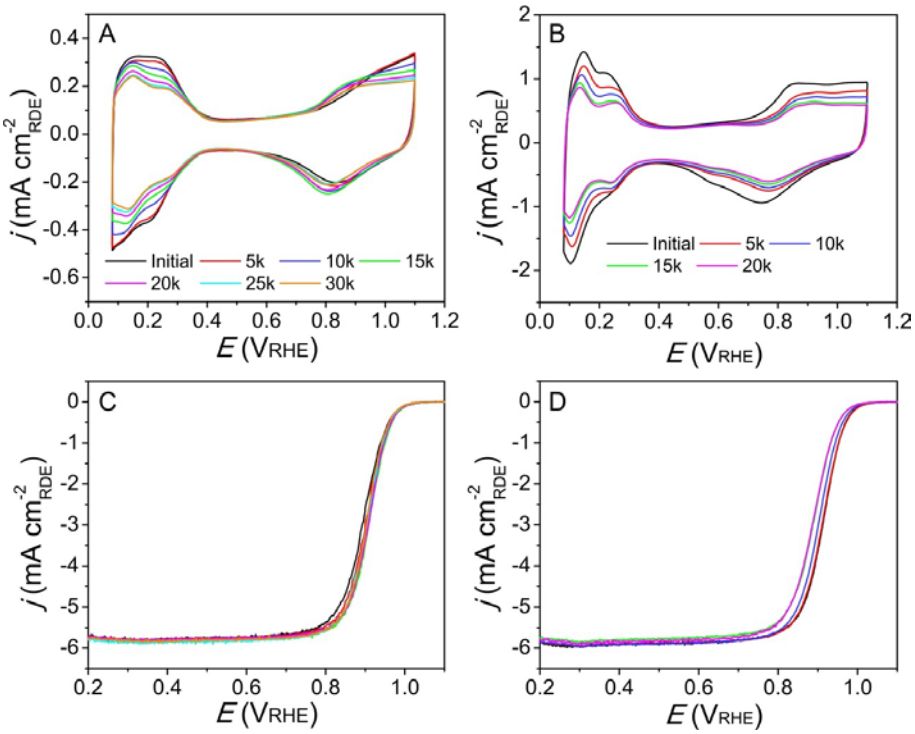

Figure 4.6. (A and B) CVs and (C and D) ORR polarization curves of the (A and C) Pt frames/C and (B and D) commercial Pt/C catalysts, respectively. For the accelerated durability tests, the CVs and ORR polarization curves were measured after sweeping 5,000, 10,000, 15,000, 20,000, 25,000 (only for Pt frames/C), and 30,000 (only for Pt frames/C) cycles between 0.6 and 1.1 V_{RHE} at a rate of 0.1 V s^{-1} in an O_2-saturated 0.1 M $HClO_4$ solution.

The observed changes in the specific activity and specific ECSA imply that the physicochemical properties (morphology and structure) of the catalyst are altered over the course of repeated potential cycles. First, I measured the Pt contents in the electrolyte after every 5,000 cycles using ICP-MS to confirm loss of Pt from the catalyst during the repeated potential sweeps. Based on the results, I calculated the amounts of Pt remaining in the catalyst and plotted the result in Figure 4.7B. After repeating 30,000 cycles of

potential sweeping, I measured only ~10% of Pt lost from the Pt frames/C catalyst. Although the loss of Pt from the catalyst over the repeated cycles could contribute to the decreased ECSA, the significant reduction of the ECSA (indicated with red squares in Figure 4.7B) implies that another factor is also contributing.

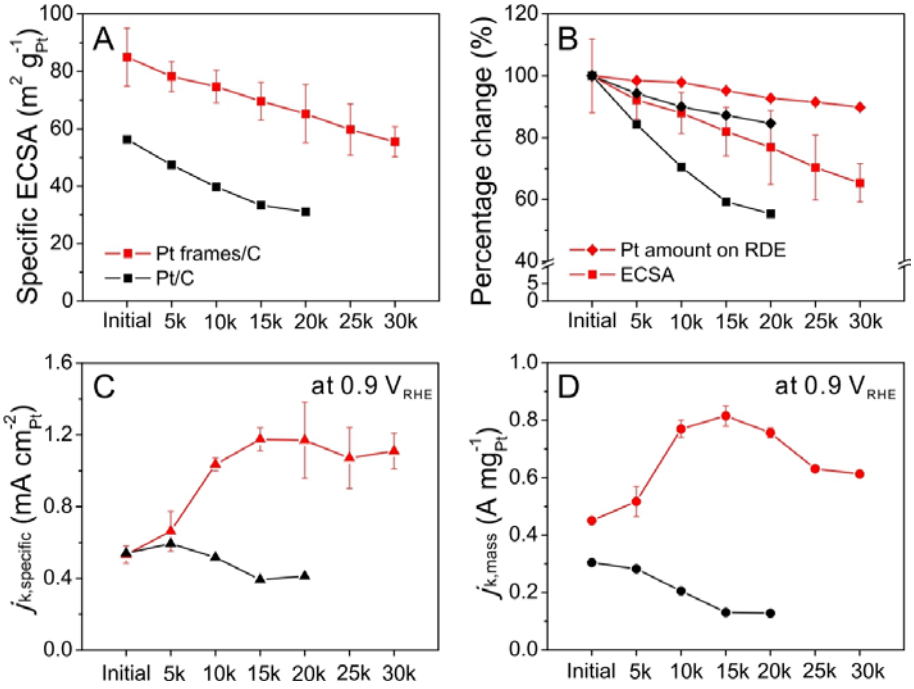

Figure 4.7. Electrocatalytic properties of the Pt frames/C (red) and commercial Pt/C (black) catalysts after repeating different number of potential cycles during accelerated durability tests: (A) Specific ECSAs, (B) Normalized amount of Pt on the electrodes (diamond) and normalized ECSAs (square), (C) Specific activities, and (D) mass activities.

I therefore investigated the morphological changes to the Pt frames/C by sampling and imaging the catalyst after every 5,000 cycles. As shown in Figure 4.8, no noticeable aggregation was observed among the nanoframes as the cycles of potential sweeping increased. Although the catalysts contain the slightly aggregated nanoframes on the carbon supports, this was also found in the catalyst before the durability test (Figure 4.5).

Thus, I can still conclude that the nanoframes did not suffer from the significant aggregation. While the small Pt nanoparticles in the Pt/C showed substantial aggregation after the durability test, the greatly enlarged contact area between the Pt nanoframes and carbon support may slow down migration of the nanoframes on the carbon surfaces, hindering aggregation among them.

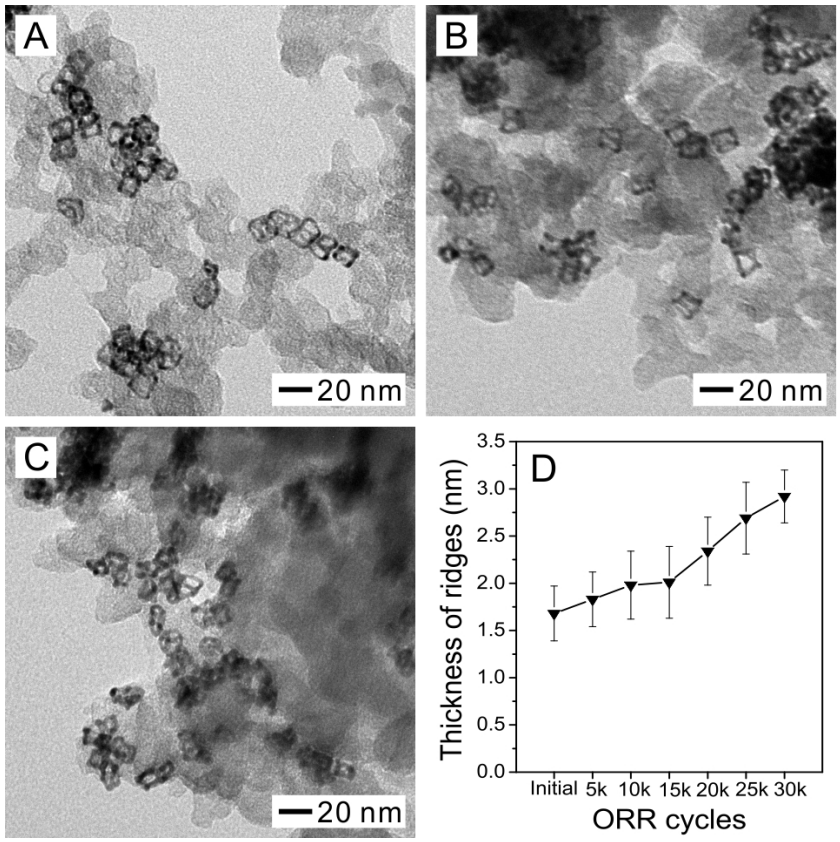

Figure 4.8. TEM images of Pt frames/C catalyst after (A) 10,000, (B) 20,000, and (C) 30,000 cycles of ORR, respectively. (D) Average ridge thickness as a function of the cycles of repeated potential sweepwing.

Even though the nanoframes seem to be slightly deformed, their open structure was still clearly maintained after 30,000 potential cycles. However, the cubic nanoframes shrank in terms of particle size. Furthermore, the average thickness of the ridges of nanoframes

increased in measurement from 1.7 to 2.6 nm, suggesting the migration of Pt atoms during cycling potential sweeps. In addition to the loss of Pt from the catalyst, the increased thickness of the Pt nanoframe ridges could contribute to the decrease in the specific ECSA during the potential cycles. The change in specific activity during the durability test also correlates to the increase in the ridge thickness. This can be attributed to the fact that the increased thickness of ridges results in a decreased proportion of low-coordinated surface atoms, thus enhancing the overall ORR activity per unit area of the frames. It is worth noting that the specific activity increases with the enlarged size of the Pt nanoparticles in the Pt/C as discussed in Chapter 2 [27−29].

Based upon their structural characteristics, the Pt nanoframes exhibited excellent improvement in catalytic durability when compared to the commercial Pt/C. The Pt/C catalyst lost more than 60% of the initial mass activity after 15,000 potential cycles. In contrast, the mass activity of Pt frames/C overall increased during 30,000 cycles to 1.4 times higher than its initial activity. It is worth pointing out that although the mass activity of Pt frames/C was only 1.5 times higher than that of the pristine Pt/C, it became more than 6-fold higher relative to the Pt/C after 15,000 cycles. Please refer to Chapter 2 for in-depth discussion regarding electrocatalytic and physicochemical properties of the commercial Pt/C with the durability test.

4.3 Summary

In this work, I have successfully synthesized Pt cubic nanoframes and evaluated their electrochemical characteristics toward ORR. The synthesis of the Pt cubic nanoframes was achieved through a two-step procedure: *i*) site-selected deposition of Pt on the Pd nanocubes and *ii*) selective removal of the Pd nanocubes by chemical etching. For the first step, I could deposit Pt atoms largely on the edges and corners of the Pd cubes by carefully controlling both the deposition rate of the free Pt atoms and the surface diffusion rate of Pt adatoms. The involvement of Br^- ions for capping Pd{100} facets

also played a crucial role for the site-selected deposition of Pt. By etching away Pd cubes from the Pd−Pt core−frame nanocubes, I obtained the Pt cubic nanoframes with an average ridge thickness of less than 2 nm. When benchmarked against the commercial Pt/C, the Pt frames/C catalyst exhibited not only higher initial mass activity toward ORR but also showed tremendously improved durability. Different from the case of Pt/C, the enlarged contact area between the nanoframes and the carbon support prevented aggregation as well as leaching of the Pt from the catalyst. Due to the increase in ridge thickness of the Pt nanoframes during repeated potential cycling, the specific ECSA of Pt frames/C steadily decreased while the specific activity increased. As a result, the mass activity of the Pt frames/C increased with cycling and to almost double the initial value after cycling 15,000 potential sweeps. Although it decreased with further potential cycling, the mass activity of the Pt frames/C catalyst rose up to 1.4-fold while repeating 30,000 cycles of potential sweeps. All findings in this work suggest that the Pt frames/C catalyst would be a excellent catalyst for ORR relative to the current commercial Pt/C for long-term use.

4.4 Experimental Section

Materials. All the chemicals were used as received from Sigma-Aldrich (unless specified). These include sodium tetrachloropalladate(II) (Na_2PdCl_4, 98%), sodium hexachloroplatinate(IV) hexahydrate ($Na_2PtCl_6 \cdot 6H_2O$, 98%), poly(vinyl pyrrolidone) (PVP, MW≈55,000), ascorbic acid (AA, 99%), potassium bromide (KBr, 99%), ethylene glycol (EG, 99%, J. T. Baker), hydrochloric acid (HCl, 34−37%, Fisher Scientific), hydrogen peroxide (H_2O_2, 30%, J. T. Baker), and ethanol (200 proof, KOPTEC). All aqueous solutions were prepared using de-ionized (DI) water with a resistivity of 18.2 MΩ cm.

Synthesis of Pd Nanocubes. The Pd nanocubes (18 nm in edge length) were synthesized using protocols reported by the Xia group [30]. In a typical synthesis of Pd

nanocubes, PVP (105 mg), AA (60 mg), and KBr (600 mg) were added into an aqueous solution (8 mL) and the mixture was heated at 80 ^{o}C for 10 min under magnetic stirring. An aqueous solution (3 mL) containing Na_2PdCl_4 (57 mg) was then quickly added into the preheated solution. The reaction solution was kept at 80 ^{o}C for 3 h under magnetic stirring. The reaction solution was cooled down to room temperature. The product was collected by centrifugation, washed twice with DI water, and re-dispersed in EG (2 mL).

Synthesis of Pd−Pt Core−Frame Nanocubes. For the synthesis of Pd−Pt core−frame nanocubes, 5 mL of the Pd nanocubes suspension (18 nm in edge length, 2 mg mL^{-1}), PVP (333 mg), AA (500 mg), KBr (324 mg), and EG (60 mL) were mixed in a three-neck flask and heated at 110 ^{o}C for 1 h under magnetic stirring. The temperature was then quickly ramped to 190 ^{o}C within 20 min, and a 60 mL of EG solution containing $Na_2PtCl_6 \cdot 6H_2O$ (0.3 mg mL^{-1}) was added dropwise with a syringe pump at a rate of 40 mL h^{-1}. After completing the injection, the reaction solution was cooled down to room temperature. The product was collected by centrifugation, washed twice with ethanol and three times with DI water, and re-dispersed in DI water.

Synthesis of Pt Cubic Nanoframes. For the synthesis of Pt cubic nanoframes, 10 mL of the aqueous suspension of Pd−Pt core−frame nanocubes (0.9 mg of Pd and 0.6 mg Pt per mL) was added into a 5 mL of aqueous solution containing PVP (1 g), KBr (6 g), HCl (6 mL), and H_2O_2 (0.24 mL). The reaction solution was kept at 100 ^{o}C for 2 h under magnetic stirring and then cooled down to room temperature. The product was collected by centrifugation, washed twice with DI water, and re-dispersed in DI water.

Preparation of a Carbon-Supported Catalyst of Pt Cubic Nanoframes (Pt Frames/C). The Pt cubic nanoframes were collected by centrifugation and re-dispersed in 10 mL of ethanol. A specific amount of carbon black (Vulcan XC-72, Cabot) was added into the suspension to obtain a loading of about 20 wt% for Pt. The mixture was then ultrasonicated for 3 h and the resultant Pt frames/C catalyst was collected by centrifugation, re-dispersed in 10 mL of acetic acid, and heated at 60 ^{o}C for 2 h under

magnetic stirring to remove residual PVP or bromide on the surface of the particles. The Pt frames/C catalyst was washed three times with ethanol and dried in an oven at 70 ^{o}C for 30 min prior to the use for ORR tests.

Morphological, Structural, and Elemental Characterizations. TEM was done with an HT-7700 microscope (Hitachi) operated at 120 kV. The elemental compositions of the samples were determined using ICP-MS (NexION 300Q, PerkinElmer).

Electrochemical Measurements. Electrochemical measurements were performed using a glassy carbon rotating disk electrode (RDE, Pine Research Instrumentation) connected to a potentiostat (CHI 600E, CH Instruments). An ink for the electrochemical measurement was prepared by adding 3 mg of the Pt frames/C into a mixture of DI water (1 mL), 2-propanol (1 mL, Sigma-Aldrich), and Nafion (40 μL, 5% solution, Sigma-Aldrich), followed by sonication for 10 min. A working electrode was prepared by loading the ink (10 μL) on the glassy carbon electrode. Another working electrode was prepared using the commercial Pt catalyst (Pt/C, 20 wt% 3.2-nm nanoparticles on Vulcan XC-72 carbon support, Premetek) using the same protocol. A reversible hydrogen electrode (RHE, Gaskastel) and a Pt coil (Pine Research Instrumentation) were used as the reference and counter electrodes, respectively. The electrolyte was an aqueous $HClO_4$ solution (70%, double-distilled, GFS chemicals) with a concentration of 0.1 M. Any residual impurities on surfaces of the catalysts were removed using a nondestructive method at room temperature by keeping the electrode potential at −0.05 V_{RHE} for 1 min. The CVs were measured in a N_2-saturated electrolyte by cycling between 0.08 and 1.1 V_{RHE} at a sweep rate of 0.05 V s^{-1}. To calculate the ECSA, I measured the charges generated from both adsorption and desorption of hydrogen between 0.08 and 0.4 V_{RHE} with a reference value of 210 μC cm^{-2} for underpotentially deposited hydrogen from a Pt surface. The ORR test was carried out in an O_2-saturated electrolyte with a scan rate of 0.01 V s^{-1} and a rotation speed of 1,600 rpm. All polarization curves were corrected for

iR-contribution within the RDE measurement system. The kinetic current density (j_k) was derived from the Koutecky−Levich equation as follows:

$$\frac{1}{j} = \frac{1}{j_k} + \frac{1}{j_d}$$

where j is the measured current density and j_d is the diffusion-limiting current density. For the accelerated durability tests, the CVs and ORR polarization curves were measured after sweeping 5,000, 10,000, 15,000, 20,000, 25,000 (only for Pt frames/C), and 30,000 (only for Pt frames/C) cycles, respectively, between 0.6 and 1.1 V_{RHE} at a rate of 0.1 V s^{-1} in an O_2-saturated aqueous $HClO_4$ solution at room temperature.

4.5 References

[1] Ferreira, P. J.; la O', G. J.; Shao-Horn, Y.; Morgan, D.; Makharia, R.; Kocha, S.; Gasteiger, H. A. *J. Electrochem. Soc.* **2005**, *152*, A2256−A2271.

[2] Chen, J.; Lim, B.; Lee, E. P.; Xia, Y. *Nano Today* **2009**, *4*, 81–95.

[3] Yu, T.; Kim, D. Y.; Zhang, H.; Xia, Y. *Angew. Chem. Int. Ed.* **2011**, *50*, 2773−2777.

[4] Zhou, W.; Wu, J.; Yang, H. *Nano Lett.* **2013**, *13*, 2870−2874.

[5] Zhang, J.; Yang, H.; Fang, J.; Zou, S. *Nano Lett.* **2010**, *10*, 638−644.

[6] Choi, S.-I.; Xie, S.; Shao, M.; Odell, J. H.; Lu, N.; Peng, H.-C.; Protsailo, L.; Guerrero, S.; Park, J.; Xia, X.; Wang, J.; Kim, M. J.; Xia, Y. *Nano Lett.* **2013**, *13*, 3420−3425.

[7] Wu, J.; Qi, L.; You, H.; Gross, A.; Li, J.; Yang, H. *J. Am. Chem. Soc.* **2012**, *134*, 11880−11883.

[8] Cui, C.; Gan, L.; Heggen, M.; Rudi, S.; Strasser, P. *Nat. Mater.* **2013**, *12*, 765−771.

[9] Chen, C.; Kang, Y.; Huo, Z.; Zhu, Z.; Huang, W.; Xin, H. L.; Snyder, J. D.; Li, D.; Herron, J. A.; Mavrikakis, M.; Chi, M.; More, K. L.; Li, Y.; Markovic, N. M.; Somorjai, G. A.; Yang, P.; Stamenkovic, V. R. *Science* **2014**, *343*, 1339−1343.

[10] Zhang, L.; Roling, L. T.; Wang, X.; Vara, M.; Chi, M.; Liu, J.; Choi, S.-I.; Park, J.; Herron, J. A.; Xie, Z.; Mavrikakis, M.; Xia, Y. *Science* **2015**, *349*, 412−416.

[11] Zhang, J.; Mo, Y.; Vukmirovic, M. B.; Klie, R.; Sasaki, K.; Adzic, R. R. *J. Phys. Chem.* B **2004**, *108*, 10955−10964.

[12] Zhang, J.; Vukmirovic, M. B.; Xu, Y.; Mavrikakis, M.; Adzic, R. R. *Angew. Chem. Int. Ed.* **2005**, *44*, 2132−2135.

[13] Adzic, R. R.; Zhang, J.; Sasaki, K.; Vukmirovic, M. B.; Shao, M.; Wang, J. X.; Nilekar, A. U.; Mavrikakis, M.; Valerio, J. A.; Uribe, F. *Top. Catal.* **2007**, *46*, 249−262.

[14] Sasaki, K.; Naohara, H.; Choi, Y.; Cai, Y.; Chen, W.-F.; Liu, P.; Adzic, R. R. *Nat. Commun.* **2012**, *3*, 1115.

[15] Shao, M.; He, G.; Peles, A.; Odell, J. H.; Zeng, J.; Su, D.; Tao, J.; Yu, T.; Zhu, Y.; Xia, Y. *Chem. Commun.* **2013**, *49*, 9030−9032.

[16] Xie, S.; Choi, S.-I.; Lu, N.; Roling, L. T.; Herron, J. A.; Zhang, L.; Park, J.; Wang, J.; Kim, M. J.; Xie, Z.; Mavrikakis, M.; Xia, Y. *Nano Lett.* **2014**, *14*, 3570−3576.

[17] Park, J.; Zhang, L.; Choi, S.-I.; Roling, L. T.; Lu, N.; Herron, J. A.; Xie, S.; Wang, J.; Kim, M. J.; Mavrikakis, M.; Xia, Y. *ACS Nano* **2015**, *9*, 2635−2647.

[18] Wang, X.; Choi, S.-I.; Roling, L. T.; Luo, M.; Ma, C.; Zhang, L.; Chi, M.; Liu, J.; Xie, Z.; Herron, J. A.; Mavrikakis, M.; Xia, Y. *Nat. Commun.* **2015**, *6*, 7594.

[19] Gasteiger, H. A.; Kocha, S. S.; Sompalli, B.; Wagner, F. T. *Appl. Catal.*, B **2005**, *56*, 9−35.

[20] Fang, Z.; Wang, Y.; Liu, C.; Chen, S.; Sang, W.; Wang, C.; Zeng, J. *Small* **2015**, *11*, 2592−2592.

[21] Xie, S.; Lu, N.; Xie, Z.; Wang, J.; Kim, M. J.; Xia, Y *Angew. Chem. Inter. Ed.* **2012**, *51*, 10266−10270.

[22] Fan, N.; Yang, Y.; Wang, W.; Zhang, L.; Chen, W.; Zou, C.; Huang, S. *ACS Nano* **2012**, *6*, 4072−4082.

[23] Ham, S.; Jang, H.-J.; Song, Y.; Shuford, K. L.; Park, S. *Angew. Chem. Inter. Ed.* **2015**, *54*, 9025−9028.

[24] Zhang, Z.-P.; Zhu, W.; Yan, C.-H.; Zhang, Y.-W. *Chem. Commun.* **2015**, *51*, 3997−4000.

[25] Lim, B.; Jiang, M.; Camargo, P. H. C.; Cho, E. C.; Tao, J.; Lu, X.; Zhu, Y.; Xia, Y. *Science* **2009**, *5*, 1302−1305.

[26] Xia, X.; Xie, S.; Liu, M.; Peng, H.-C.; Lu, N.; Wang, J.; Kim, M. J.; Xia, Y. *P. Natl. Acad. Sci. U. S. A.* **2013**, *110*, 6669−6673.

[27] Greeley, J.; Rossmeisl, J.; Hellmann, A.; Nørskov, J. K. *Z. Phys. Chem.* **2007**, *221*, 1209−1220.

[28] Mayrhofer, K. J. J.; Strmcnik, D.; Blizanac, B. B.; Stamenkovic, V.; Arenz, M.; Markovic, N. M. *Electrochim. Acta* **2008**, *53*, 3181−3188.

[29] Xie, S.; Choi, S.-I.; Xia, X.; Xia, Y. *Curr. Opin. Chem. Eng.* **2013**, *2*, 142−150.

[30] Jin, M.; Liu, H.; Zhang, H.; Xie, Z.; Liu, J.; Xia, Y. *Nano Res.* **2011**, *4*, 83−91.

CHAPTER 5

CONCLUSIONS AND FUTURE DIRECTIONS

5.1 Conclusions

This dissertation covers a number of strategies for developing Pt-based electrocatalysts with enhanced performance toward ORR. I started with the fabrication of Pd@Pt_{nL} core−shell octahedral nanocrystals (n = 2−5) *via* two different protocols based upon polyol and aqueous solutions, respectively. In both the protocols, Pt atoms could be deposited as conformal, ultrathin shells on the entire surface of Pd octahedra by controlling the kinetics for the deposition of Pt atoms and subsequent diffusion of the Pt adatoms. In particular, the number (n) of Pt atomic layers could be tuned from two to five by simply varying the amount of precursor injected into the reaction solution. When benchmarked against a state-of-the-art commercial Pt/C catalyst, the Pd@Pt_{nL} core−shell octahedral nanocrystals exhibited significant improvement in both the activity and durability. DFT calculations suggested that the enhanced activity could be attributed to the destabilization of OH* on the surfaces of Pd@Pt_{nL} octahedral nanocrystal with respect to the Pt/C. This destabilization facilitates hydrogenation of OH*, accelerating the overall ORR kinetics. I was also able to conclude that the improved durability for the Pd@Pt_{nL} octahedra arose from both the involvement of enlarged particle size and the presence of Pd as a sacrificial core.

I further extended the protocol for the deposition of conformal Pt shells to passivate Pt−Ni alloy octahedral nanocrystals and then address their poor durability during ORR. I successfully achieved the conformal deposition of Pt ultrathin shells on the surface of Pt−Ni octahedral nanocrystals by dropwise injecting a Pt precursor solution into a suspension of Pt−Ni octahedral nanocrystals at 200 ^{o}C. In this work, I systematically evaluated the long-term stability of the catalyst based upon the Pt−Ni@$Pt_{1.5L}$ core−shell

octahedral nanocrystals by benchmarking against their Pt−Ni counterparts without the Pt shells. Based on the compositional changes during an acid treatment of the catalysts, it was found that the Pt shells could effectively protect the Ni in the Pt−Ni alloy cores from dissolution in a highly corrosive environment. In addition to the improvement in chemical stability, the Pt−Ni@$Pt_{1.5L}$/C catalyst exhibited substantial enhancement in electrocatalytic durability toward ORR when compared with the Pt−Ni/C. Furthermore, the exceptionally high specific activity of the Pt−Ni/C was well retained when only ultrathin Pt shells were deposited on the surface.

I also prepared a new ORR catalyst based upon cubic nanoframes comprised of ultrathin Pt ridges (<2 nm in thickness) with open faces and a hollow interior. The Pt cubic nanoframes were synthesized through the site-selected deposition of Pt on Pd nanocubes and the selective removal of the Pd nanocubic cores. For the site-selected deposition, the kinetics for the deposition of Pt atoms and the diffusion of Pt adatoms were carefully tuned by adjusting the injection rate of the Pt precursor and the reaction temperature, respectively. The Pt nanoframes showed a higher initial mass activity relative to the state-of-the-art Pt/C catalyst. This can be attributed to the open structure of the nanoframe, which results in a high specific ECSA. Moreover, the Pt frames/C catalyst showed substantially improved durability when benchmarked against the Pt/C.

My research has validated a number of strategies for developing advanced ORR catalysts with great enhancement in activity and/or durability. I has also contributed a fundamental understanding of catalytically relevant physicochemical properties of Pt-based nanocrystals. This work represents a major step forward toward the development of advanced ORR catalysts for future commercial application.

5.2 Future Directions

The strategies described in my dissertation involve controlling the physicochemical properties of Pt-based nanocrystals, such as crystal facets, elemental composition, and structure to improve the activity and/or durability of an electrocatalyst toward ORR. A few remaining barriers still need to be addressed in order to attain a successful, large-scale operation of PEMFCs in the automotive industry.

One of the major remaining challenges is to validate the enhanced activity and durability of the ORR catalysts in an actual operating PEMFC system. Even though a number of Pt-based catalysts showed promising results toward ORR, most of them were obtained *via* a RDE method, which is a half-cell test. The RDE method is known to provide the reliable trends of activity and durability, which can be used to predict the performances of the ORR catalyst in the actual PEMFC system. However, recent publications reported that despite the remarkable catalytic performance measured by the RDE method, these catalysts have not yet produced encouraging results in MEA tests [1−4]. Although the ORR activity is measured at 0.9 V_{RHE} and under atmospheric pressure for oxygen in both the RDE and MEA methods, the values from the two methods often do not agree.

For the automotive applications of PEMFCs, it is critical to evaluate the catalytic durability in the MEA system. While the durability of an ORR catalyst can be examined in a RDE test by repeating potential cycles in an acidic medium, it is incredibly difficult to simulate the wide range of stress conditions in a working fuel cell such as start−stop cycles, low humidity, and fuel starvation. In addition to degradation of the catalyst itself, contamination of ionomer and/or membrane by the dissolved metal cations can also degrade the catalytic performance, which cannot be considered in the RDE method. Thus, it is critical to measure the activity and durability of new catalysts through the MEA method in order to obtain a realistic understanding of the catalytic behavior in a PEMFC. This effort will offer significant progress in evaluating the performance of a catalyst in a

PEMFC, paving the way toward large scale commercialization.

Another major challenge in this field is the development of optimal processes for industrial production of the Pt-based nanocrystals while ensuring high yield and good uniformity for the products. However, regarding the process development, only limited research has been conducted so far. For successful implementation of nanocrystals in commercial applications, we need to address the difficulties of scaling up a synthesis that has traditionally been conducted in a batch reactor. Rather than increasing the volume of the batch, a continuous flow droplet reactor can be considered for scaling up the synthesis of the nanocrystals. In recent publications, Xia and co-workers have demonstrated the large scale synthesis of highly uniform nanocrystals using a continuous flow droplet reactor [5, 6]. Although this approach could be applied to the scale-up synthesis of Pt-based nanocrystals for use as advanced ORR catalysts, current batch synthesis protocols need to be modified and optimized for the continuous flow droplet reactor.

Finally, a new and simple protocol needs to be developed for the synthesis of Pt-based nanocrystals with uncommon structures such as core−shell, nanocages, and nanoframes. Due to the complex morphologies of these nanocrystals, two or more synthetic steps are generally involved, resulting in a higher cost for the production [7−10]. Thus, it is necessary to simplify the protocol by reducing the number of steps, or to even develop a single-step approach, in order to make the Pt-based nanocrystals a viable choice of commercial catalysts.

5.3 References

[1] Kongkanand, A.; Mathias, M. F. *J. Phys. Chem. Lett.* **2016,** *7*, 1127−1137.

[2] Carpenter, M. K.; Moylan, T. E.; Kukreja, R. S.; Atwan, M. H.; Tessema, M. M. *J. Am. Chem. Soc.* **2012**, *134*, 8535−8542.

[3] Stamenkovic, V. R. *Nanosegregated Cathode Catalysts with Ultra-Low Platinum Loading*; Annual Merit Review DOE Hydrogen and Fuel Cells and Vehicle

Technologies Programs, Washington, DC, 2015. http://www.hydrogen.energy.gov/pdfs/review15/fc008_stamenkovic_2015_o.pdf.

[4] Debe, M. K. *Nature* **2012**, *486*, 43−51.

[5] Zhang, L.; Xia, Y. *Adv Mater* **2014,** *26*, 2600−2606.

[6] Zhang, L.; Wang, Y.; Tong, L.; Xia, Y. *Nano Lett.* **2014,** *14*, 4189−4194.

[7] Xie, S.; Choi, S.-I.; Lu, N.; Roling, L. T.; Herron, J. A.; Zhang, L.; Park, J.; Wang, J.; Kim, M. J.; Xie, Z.; Mavrikakis, M.; Xia, Y. *Nano Lett.* **2014,** *14*, 3570−3576.

[8] Lim, B.; Jiang, M.; Camargo, P. H. C.; Cho, E. C.; Tao, J.; Lu, X.; Zhu, Y.; Xia, Y. *Science* **2009,** *324*, 1302−1305.

[9] Chen, C.; Kang, Y.; Huo, Z.; Zhu, Z.; Huang, W.; Xin, H. L.; Snyder, J. D.; Li, D.; Herron, J. A.; Mavrikakis, M.; Chi, M.; More, K. L.; Li, Y.; Markovic, N. M.; Somorjai, G. A.; Yang, P.; Stamenkovic, V. R. *Science* **2014,** *343*, 1339−1343.

[10] Zhang, L.; Roling, L. T.; Wang, X.; Vara, M.; Chi, M.; Liu, J.; Choi, S.-I.; Park, J.; Herron, J. A.; Xie, Z.; Mavrikakis, M.; Xia, Y. *Science* **2015,** *349*, 412−416.